Spring 5-4-2019

Human Immunodeficiency Virus Theranostics

Christopher J. Woldstad
University of Nebraska Medical Center

HUMAN IMMUNODEFICIENCY VIRUS

THERANOSTICS

by

Christopher James Woldstad

A DISSERTATION

Presented to the Faculty of

the University of Nebraska Graduate College

in Partial Fulfillment of the Requirements

for the Degree of Doctor of Philosophy

Pharmacology and Experimental Neuroscience Graduate Program

Under the Supervision of Drs. Michael Boska (deceased), Yutong Liu and Howard E. Gendelman

University of Nebraska Medical Center

Omaha, Nebraska

May, 2019

TABLE OF CONTENTS

LIST OF FIGURES

ACKNOWLEDGEMENTS

I would like to begin my acknowledgements by saying that I was completely overwhelmed with the amount of help and support I received during my graduate career at UNMC. Every single person I collaborated with in my graduate studies was not only courteous and professional but exhibited warmth and patience as well. It is difficult to express my gratitude to each and every person that influenced me in a few short pages, but it should be known that I will look reflect back on my time with my coworkers and professors with fondness for the rest of my life

First and foremost I would like to thank my parents, Jeffrey and Carol Woldstad. They have always been there for me, through good times and bad, and surely without their emotional support and guidance I would not have succeeded. My brother, Patrick Woldstad, has also been there as a shoulder to lean on as I struggled throughout the years. I am deeply grateful for my family, as they have shaped me into the person I am today.

Next, I would like to thank my graduate advisors for giving me the opportunity to pursue my graduate work in their laboratories. Dr. Michael Boska, may he rest in peace, was an incredibly kind and intelligent man who first offered me a position within his research laboratory. His impact on my development as a researcher cannot be understated; his willingness to listen and field my thoughts and ideas while giving his own thoughtful input was just one of his many great qualities. Dr. Boska's leadership proved invaluable in the completion of my graduate projects, and he will be forever missed and remembered since his untimely passing in May of 2017.

Dr. Howard Gendelman, my co-advisor, has also been extremely supportive during my graduate journey. Always encouraging and willing to help, Dr. Gendelman has provided valuable insight and expertise at every step, and for that I am very thankful. His examples and lessons of leadership both in my graduate education as well as numerous other students as been deeply impactful on me, and will continue to influence me as I proceed further into my career. Finally, I would like to thank Dr. Yutong Liu, who graciously stepped up to fill the role of my advisor after

Dr. Boska passed away. Assuming responsibility of a graduate student several years into his studies could not have been easy, yet Dr. Liu did so with understanding and grace. His thoughtful advice has been greatly appreciated over these last few years, and his ability to step up as leader of the radiology lab in the wake of such tragedy has been remarkable.

I would like to extend my gratitude to the members of my committee: Dr. Larisa Poluektova, Dr. Balasrinivasa Sajja, and Dr. Myron Toews. Their advice and guidance through my PhD studies was extremely helpful, and I greatly appreciate the time they provided. Their inputs and constructive criticism proved invaluable for the completion of my degree. Additionally, I would like to thank Drs. Gary Suizdak, Mingling Fang, and Rafael Montenegro-Burke of the Scripps Institute for their help and contributions to one of my projects. Drs. Benson Edgawa and JoEllyn McMillan were also incredibly supportive during the completion of my PhD, and were always willing to lend helpful advice, both scientifically and emotionally. To them I am very grateful.

Two postdoctoral fellows (now promoted to instructors) have been particularly influential during my graduate studies. To begin with is my good friend Dr. Bhavesh Kevadiya, a remarkable scientist and chemist. Endlessly patient, consistently good natured and kind, and relentlessly hardworking, Bhavesh truly is representative of the researcher I aspire to be. As shared first author on the major manuscript of my thesis, his work and support has been immensely helpful for the completion of my degree. Without his expertise and contributions, particularly within the synthesis and characterization of our nanoparticles, the completion of my doctorate degree would not have been possible. For that, I am eternally grateful, and wish him the best of luck as he continues on what surely will be a great scientific career. Dr. Aditya Bade not only provided me invaluable insight and support in completion of my projects, but was also a great friend as well. Countless times I would talk Aditya's ear off about my problems, and countless times would he be patient, supportive, and lend fantastic advice. Aditya kept me emotionally grounded, and focused, and because of this I cannot offer him thanks enough.

The members of the radiology core lab not only have lent their expertise and assistance in the completion of my projects, but have also provided me with a sense of family within the laboratory. Dr. Balasrinivasa Sajja, Dr. Mariano Uberti, Melissa Mellon, Ahmad Tanwir, Shea Lundeby and Lirong Xu have all be invaluable to me these last 5 years. It saddens me to leave them behind as I continue on in my career, but I wish them all the best.

Many thanks to our department administrative staff, Theresa Grutel, Lana Reichardt , Robin Taylor, Kim Morrison, Julie Ditter, Johna Belling, Myhanh Che, Na Ly, and Reed Felderman for their enormous administrative help and support throughout my Ph.D. I would also like to thank to member of bioimaging core facility, Marie Witthoft, for her administrative help and support.

Lastly I would like to extend gratitude to my lab mates and close friends who made coming into laboratory each day a bit more fun and enjoyable: Brendan Ottemann, Brady Silman, Jimmy Hilare, Ted Kocher, Denise Cobb, Mary Banoub, Ibrahim Ibrahim, Insiya Mukadam, Tanmay Kulkarny, Hang Su, Jonathon Herskovitz, and many others. I wish each and everyone of you continued success and happiness.

LIST OF ABBREVIATIONS

AFM	Atomic force microscopy
AIDS	Acquired immunodeficiency syndrome
ALB	Albumin
ALT	Alanine aminotransferase
AMY	Amylase
APC	Antigen presenting cell
ART	Antiretroviral therapy
ATR	Attenuated total reflectance
AZT	Azidothymidine
BBB	Blood brain barrier
BMVEC	Brain microvascular endothelial cells
CF	Cobalt Ferrite
CD4	Cluster designation 4
CNS	Central nervous system
CPMG	Carr Purcell Meiboom Gill
CR	Cerebellum
CSF	Cerebrospinal fluid
CTLs	Cytolytic T lymphocytes
CXCR4	C-X-C chemokine receptor type 4
DC	Doral cortex
DCM	Dicholoromethane
DMSO	Dimethyl sulfoxide
DSPE-PEG2000	1,2-distearoyl-phosphatidylethanlamine-

	methyl-polyethyleneglycol conjugate-2000
DOPE	1,2-dioleoyl-sn-glycero-3-phosphoethanolamine
DTG	Dolutegravir
Eu^{3+}	Europium
EuCF-DTG	Europium doped cobalt ferrite dolutegravir loaded nanoparticles
EuCF	Europium doped cobalt ferrite
FA-EuCF-DTG	Folic acid decorated europium doped cobalt ferrite dolutegravir loaded nanoparticles
FA	Folic acid
FC	Frontal cortex
FOV	Field of view
FR-β	Folic acid receptor beta
FTIR	Fourier transformed infrared spectra
Gd	Gadolinium
Gp-120	Glycoprotein 120
GSSG	Glutathione disulfide
GSH	Glutathione
H	Hippocampus
HAART	Highly active antiretroviral therapy
HAD	HIV associated dementia
HAND	HIV associated neurocognitive disorder
HIV-1	Human immunodeficiency virus type 1
HPLC	High performance liquid chromatography

ICP-MS	Inductively coupled plasma mass spectrometry
IDL	Interactive Data Language
IM	Intramuscular
IV	Intravenous
LASER ART	Long acting slow effective release antiretroviral therapy
LC-MS	Liquid chromatography mass spectrometry
LPS	Lipopolysaccharide
MCP-1	Monocyte chemotactic protein 1
MDM	Monocyte-derived macrophages
MGCs	Multinucleated giant cells
MIP-1α	Macrophage inflammatory protein-1 alpha
Mn^{2+}	Manganese
MOI	Multiplicity of infection
MP	Mononuclear phagocytes
MRI	Magnetic resonance imaging
MRM	Multiple reaction monitoring mode
NAA	N-acetylaspartate
NAD	Nicotinamide adenine dinucleotide
NADP	Nicotinamide adenine dinucleotide phosphate
NHS	N-hydroxysuccinimide ester
NP	Nanoparticles
NNRTI	Non-nucleoside reverse transcriptase inhibitor
NRTI	Nucleoside reverse transcriptase inhibitor
PBS	Phosphate-buffered saline
PC	Phosphatidylcholine

PCL	Polycaprolactone
PD	Pharmacodynamics
PEG	Polyethylene glycol
PDI	Polydispersity index
PFA	Paraformaldehyde
PHOS	Phosphate
PK	Pharmacokinetics
PI	Protease inhibitor
QDI	Quantum Design International
ROI	Region of interest
ROS	Reactive oxygen species
RT	Reverse transcriptase
SIV	Simian immunodeficiency virus
SQUID	Superconducting quantum interference device
TBHP	Tert-butyl hydroperoxide
TBIL	Total bilirubin
TCA	Tricarboxylic acid
TEM	Transmission electron microscopy
TP	Total protein
TSE	Turbo spin echo
UPLC-MS/MS	Ultraperformance liquid chromatography tandem mass spectrometry
VC	Ventral cortex
XRD	X-ray diffraction

ABSTRACT

RATIONALE: Long-acting slow effective release antiretroviral therapy (LASER ART) was developed to improve patient regimen adherence, prevent new infections, and facilitate drug delivery to human immunodeficiency virus cell and tissue reservoirs. However, maintenance of sustained plasma drug levels, for weeks or months, after a single high-level dosing, could improve regimen adherence but, at the same time, affect systemic toxicities. Of these, the most troubling are those that affect the central nervous system (CNS) In an effort to facilitate LASER ART development, "multimodal imaging theranostic nanoprobes" were created. These allow combined bioimaging, drug pharmacokinetics and tissue biodistribution tests in animal models. Additionally, dolutegravir (Tivicay, DTG), in both a native drug form and within a nanoformulations, were administered to mice to investigate potential neurotoxicity or lack thereof in animal models for further LASER ART technology development.

METHODS: Europium (Eu^{3+})- doped cobalt ferrite (CF) dolutegravir (DTG)- loaded (EuCF-DTG) nanoparticles were synthesized then fully characterized based on their size, shape and stability. These were then used as platforms for nanoformulated drug biodistribution. Rodents were administered parenteral 45-mg/kg doses. DTG-associated changes in CNS homeostasis were assessed by measuring brain metabolic activities. After antiretroviral treatment, brain subregions were dissected and screened by mass spectrometry-based metabolomics.

RESULTS: Folic acid (FA) decoration of EuCF-DTG (FA-EuCF-DTG) nanoparticles facilitated macrophage targeting and sped drug entry across cell barriers. Macrophage uptake was higher for FA-EuCF-DTG than EuCF-DTG nanoparticles with relaxivities of r2 = 546 mM^{-1} s^{-1} and r2 = 564 mM^{-1} s^{-1} in saline, and r2 = 850 mM^{-1} s^{-1} and r2 = mM^{-1} s^{-1} in cells, respectively. The values were ten or more times higher than what was observed for ultra-small superparamagnetic iron oxide particles (r2 = 31.15 mM^{-1} s^{-1} in saline) using identical iron concentrations. Drug particles were detected in macrophage Rab compartments by dual fluorescence labeling. Replicate particles

elicited sustained antiretroviral responses. After parenteral injection of FA-EuCF-DTG and EuCF-DTG into rats and rhesus macaques, drug, iron and cobalt levels, measured by LC-MS/MS, magnetic resonance imaging, and ICP-MS were coordinate. Within metabolomic experimentations, metabolic drug-related dysregulation of energy and oxidative stress were readily observed within the cerebellum and frontal cortex following native drug administrations. Each was associated with alterations in neural homeostasis and depleted canonical oxidation protection pools that included glutathione and ascorbic acid. Surprisingly, the oxidative stress-related metabolites were completely attenuated when DTG was administered as nanoformulations. These data demonstrate the importance of formulation design in control of DTG or perhaps other antiretroviral drug-associated CNS events.

CHAPTER 1
Introduction

1.1 Global significance of HIV-1

Human Immunodeficiency Virus (HIV-1) is a progressive retrovirus of the human immune system which, if left untreated, can eventually lead to acquired immunodeficiency syndrome (AIDS). Causing a global pandemic shortly after its discovery in the early 1980's, HIV-1 has been in the crosshairs of medical research for several decades, with the molecular structure, function, regulation, tropism, and means of viral persistence having now been documented [1-3]. Regardless of such efforts, more than 70 million people have been infected with HIV-1 since its discovery, with 35 million people succumbing to the virus after initial infection [4]. Additionally, it is estimated that at the end of 2017 approximately 37 million people live infected with HIV-1 around the world. Treatment and management of patients infected with the virus continues to be one of the greatest challenges of the modern medical era.

Development of treatment options for patients infected with HIV-1 is arguably one of the most significant victories in pharmaceutical research, with dozens of effective antiretroviral therapies being brought to market since azidothymidine (AZT) was first approved in 1987 [5, 6]. Antiretroviral therapy (ART) has allowed for a completely new prognosis following HIV-1 infection; recently diagnosed patients no longer fear certain death within years but instead anticipate a prolonged lifespan with a chronic but manageable disease. Furthermore, more recent innovations in ART technology has allowed concurrent administration of multiple antiretroviral compounds to patients, drastically increasing their effectiveness in limiting HIV-1 replication and inhibiting viral resistance. Combination ART (cART) markedly reduces HIV-1 replication such that HIV-1 RNA is undetectable within plasma, allowing for reduced disease morbidity [7, 8]. However, despite such pharmacological advances and sustained viral suppression, ART cannot eliminate viral infection. Complete viral eradication requires the development of new and novel drug technologies, with improvements in drug design and delivery being at the forefront of significance

1.2 HIV-1 virology and pathology

HIV-1 is a retrovirus, using its own reverse transcriptase to transcribe a single stranded viral RNA into a double stranded DNA for integration into the host genome and completion of the viral life cycle. Two identical copies of single stranded RNA reside within the cylindrical capsid of the virus and contain genes needed for the encoding the structural viral proteins [1, 9]. Group-specific antigen, or gag, encodes the proteins of the viral core and matrix, such as viral capsid protein HIV-1 p24 and matrix protein HIV-1p17 [10]. The env gene encodes proteins that form the viral envelope, specifically glycoprotein 120 (HIV-1gp120) and transmembrane glycoprotein 41 (HIV-1gp41). The pol gene encodes a variety of HIV-1 enzymes, such as reverse transcriptase that is required for the transcription of HIV-1 RNA into DNA for integration into the host cell genome [11]. All three genes are critical for the propagation of HIV-1 within an infected host, and as such these genes and the proteins they encode have become biological targets of antiretroviral drug (ARV) therapy.

Protease, ribonuclease, and integrase are also enzymes residing within the HIV-1 core encoded by pol that are necessary for HIV-1 replication [12, 13]. In addition to these enzymes, several accessory and immune-regulatory genes within the viral capsid core play a vital role for viral function. Trans-activator of transcription, or Tat, causes substantially increased levels of reverse transcription to occur after a small number of RNA transcripts are made via a positive feedback loop [10]. Regulator of viral protein expression, or Rev, dictates the movement of RNA from cytoplasm to nucleus. Other necessary proteins include viral protein R (Vpr), viral infectivity factor (Vif), negative regulatory factor (Nef), and HIV-1p7 [14]. While the biological mechanism in which Vpr, Vif, and Nef influence HIV-1 replication are not completely known, it has been established that these proteins positively affect HIV-1 replication.

The primary target of progeny infectious HIV-1 and the most commonly infected cell is the CD4+ T lymphocyte [15, 16]. This was shown by isolation, propagation and molecular analyses

of the viral genome in HIV-1 infected patients [17, 18]. These investigations definitively showed that proviral DNA is integrated within CD4+ T cells and to more limited degree monocyte-macrophages [19]. Indeed, impaired immune response is characteristic of all stages of the disease with parallel deficits in numbers and function [20]. Infection of a CD4+ T cells begins when an HIV-1 virion encounters its cluster designation 4 (CD4) receptor together with its co-receptor molecule, the C-X-C chemokine receptor type 4 (CXCR4). Co-receptor use ensures viral cell entry. Tight binding of HIV-1 gp120 to the CD4 molecule(s) on the surface of the host cell allows the membranes of the virus and the host cell to fuse. The virion's RNA, proteins, and enzymes are then released into the cell following successful cellular fusion and digestion of the protective virion capsid, with the envelope of HIV-1 remaining on the outer membrane of the cell.

Reverse transcription is completed by HIV-1 enzymes utilizing the infected host cell's deoxynucleotides. Viral DNA synthesis occurs concurrently with the degradation of the original viral RNA, as the reverse transcriptase enzyme also has RNase activity. During each iteration of RNA to DNA reverse transcription within a infected host cell, the probability of a random mutation is relatively high due to reverse transcriptase's relatively poor proof reading capabilities [21]. This is what allows HIV-1 to develop viral mutations over time that potentially is beneficial to its propagation within the host, such as developing ART resistance. Reverse transcription is performed twice to produce a double stranded DNA molecule, after which there is binding to the viral integrase enzyme. Integrase can then transport the double stranded viral DNA into the nucleus of the host cell as well as creating a cut within the host cell genome for viral DNA integration [22].

DNA replication, RNA transcription, and protein translation occurring via host cell machinery allows for the production of progeny HIV-1 that occurs after assembly of viral proteins with subsequent transport to the host cell membrane for virion packaging. Assembly is controlled primarily by Gag precursor molecules, Pr55 Gag and Pr160 GagPol [23]. The production of a mature virus particle consists of encapsidation of the viral RNA, viral budding, release of the viral

particles from the infected cells, and finally proteolytic processing of Pr160 and Pr55 during maturation [23].

1.3 Viral transmission

Transmission occurs by separate routes (through contaminated needles, by transfusion of blood and blood products, from mother to fetus and by receptive anal or vaginal intercourse) [24]. The actual process ensues through cells or by the virus itself. As per the latter, HIV-1 is released to float freely within plasma until they come in contact and interact with a host cell suitable for entrance and infection. "Cell-to-cell transmission" is the alternative mechanism for the progression of HIV-1 infection, in which direct contact between an infected cell with an uninfected naïve cell results in HIV-1 transmission. Cell-to-cell transmission occurs during the fusion of HIV-1 infected cells with that of uninfected susceptible cells; the fusion process causes the viral components to be deposited into the uninfected cell, subsequently causing multinucleated giant cells [25, 26].

1.4 Immune Response to HIV-1

AIDS occurs as a consequence of progressive viral infection and CD4+ T cell depletion. It is classified as patients infected with HIV-1 that have CD4+ T cell counts below 200 per µl, compromising cell-mediated immunity, or by opportunistic viral, fungal, parasitic and mycobacterial infections that are strongly associated with advanced HIV-1 infection [14, 27]. Ultimately, patients succumb to HIV-1 not directly from the virus itself, but rather indirectly as opportunistic infections take advantage of a weakened and dysfunctional immune system. However, the progression of the HIV-1 disease state, from initial infection/transmission to complete immune failure, is a process taking many years or even decades, and is characterized into several distinct stages defined by the current immune response [28]. These four stages are: primary infection, a clinically asymptotic period, symptomatic HIV-1 infection, and HIV-1 to AIDS progression. Each infected individual varies in their respective length, severity, and symptoms of

each stage; it is of importance to mention that patients consistently taking ARV medication generally will not progress to the later stages of the disease [28].

Primary infection is the beginning of HIV-1 disease progression as the virus establishes itself within the host body. This stage typically lasts only a few weeks after initial transmission. Within the first 24 hours after infection, HIV-1 virions infect dendritic cells within the mucous membrane; after about 5 days, these infected dendritic cells are recruited to lymph nodes and the peripheral blood, where replication rates dramatically increase. The primary infection stage is characterized by substantially decreasing CD4+ T cells and exponentially increasing levels of viremia, often millions of virus copies per milliliter of plasma [29]. Such a large number of HIV-1 viral particles within the blood allows for systemic infection of peripheral lymphoid organs. Regardless of this viral spike, the body's immune response during primary infection eventually results in reduction of virus levels within the peripheral blood. Virus specific cytolytic T lymphocytes (CTLs) appear early in infection and potentially downregulate HIV-1 replication [30, 31]. CD8+ T cells are also credited in controlling the initial viremia peak that is characteristic of primary infection; activated and mature CD8+ T cells possess different anti-HIV-1 processes. Specifically, CD8+ T-cells can release cytokines such as RANTES, MIP-1 alpha, and MIP-1 beta that can effectively block the entry of HIV-1 into host cells by competing for or downregulating cellular co-receptor CCR5 [30, 31]. Following a severe reduction in plasma viremia and a small rebound in CD4+ T-cell populations, patients progress to the clinically asymptomatic stage.

The period of time between the initial primary infection stage and the development of AIDS is classified as the clinically asymptomatic stage. After the initial viremia peak and subsequent decrease in HIV-1 plasma characteristic of the primary infection stage, HIV-1 continues to replicate within infected cells and is readily detected in almost all lymphoid tissue [32, 33]. Consistent viral replication results in chronic immune stimulation; this strain on the immune system is thought to be responsible for its eventual deterioration as well as the progressive death of

lymphoid tissue [34]. Despite continual propagation of the virus and gradually decreasing CD4+ T-cell populations, infected patients generally don't exhibit any clinical symptoms at this stage, as immunodeficiency has not progressed enough to compromise cell-mediated immune function.

The final phase includes both the stage of symptomatic HIV-1 infection as well as the progression of HIV-1 to AIDS. While the immunological hallmark of the progression from the asymptomatic stage was gradual loss of CD4+ T-cells, the symptomatic stage is defined by a steeper decline in CD4+ T cell populations and overall increase in systemic viral load [35]. This is due to systemic viral replication at multiple sites in addition to the high amount of replication happening within lymphoid tissue. The amount of time required for the development of clinical immunodeficiency from the asymptomatic stage is variable among infected individuals: indeed, the complexity of host and viral factor interactions are integral to the eventually outcome of the disease [28]. Overall, low amounts of viral replication and retention of immune function favors a slow progression of HIV-1 infection, while high viremia and immune dysfunction leads to a more rapid disease progression.

1.5 Antiretroviral therapy (ART)

The natural history of HIV-1 infection that is outlined in the previous section is dependent on infected individuals not being administered any HIV-1 specific treatment during their infection. This is representative of the clinical landscape in the decade following the discovery of HIV-1 in 1983, in which medical professionals were largely ignorant about the virus and its pathology. Treatment options were limited if not non-existent during this period; testing positive for HIV-1 was universally fatal, with survival time directly dependent on the individual's own progression from initial infection to AIDS.

This changed in 1987 with the development and testing of a dideoxynucleoside reverse transcriptase inhibitor (NRTI), azidothymidine (AZT), the world's first antiretroviral drug used to

treat HIV-1 [6]. Benefits of AZT treatment were limited; greater survival times were found in patients at 24 weeks, but this effect was short-lived and by 48 weeks' time, survival benefits were no longer observed [36, 37]. Additionally, AZT treatment showed side effects of transient anemia and malaise due to off target toxicities, particularly in high doses given to HIV-1 patients shortly after approval. Regardless of AZT's limitations, the effects seen on the survivability of HIV-1 patients spurred medical research to investigate the potential of antiretroviral therapy. Three additional NRTIs were then released in quick succession: zalcitabine (ddC), didanosine (ddI), and stavudine (d4T). All three medications had particular toxicities and as of present none are widely administered within the clinic [38, 39]. However, the development and administration of these early antiretroviral drugs, and their associated toxicities, inevitably led physicians to give treatment sequentially or to alternate between different therapies, a strategy that would serendipitously prove effective as more antiretrovirals became developed [40]. Patients continued to fare poorly within the clinic, but with small reductions in the rate of adverse reactions there was optimism antiretroviral research was heading in the right direction.

Combination NRTI therapy, in which two or more antiretrovirals are given as a treatment concurrently, was another clinical concept that showed encouraging results in the early 1990s. The development of lamivudine (3TC), a cytidine analog, allowed for another drug to be used in combination with other NRTIs and proved to be synergistic with the other compounds [41]. But despite such progressions, the quality of life for HIV-1 patients continued to be poor. Triple drug combination strategies were the only cases showing any sign of significantly controlling HIV-1 infection, and early NRTIs, particularly thymidine analogs, continued to have issues with toxicity [39].

The development of different classes of ARVs was perhaps the most substantial advancement of HIV-1 therapeutics. Groups of drugs that have a direct effect on HIV-1 viremia but do so via different biological mechanisms; when given in combination, have proved effective

at limiting viral resistance while decreasing viral plasma levels. Saquinavir became the first protease inhibitor (PI) approved in 1995, but initial formulations struggled with poor bioavailability and deactivation by enzymatic metabolization [39]. Ritonavir, another PI, was developed shortly after saquinavir. Ritonavir was found to be a potent inhibitor of one of the enzymes responsible for deactivating saquinavir, and when given in combination, dual saquinavir and ritonavir administration was found to be quite effective at HIV-1 suppression, though tolerability was low [42]. Eventually is was determined that high-dose saquinavir and low-dose ritonavir in combination was optimal for effective protease inhibition, and still represents the recommended usage for protease inhibition in the clinic at present [39]. Nevirapine became the first non-nucleoside reverse transcriptase inhibitor (NNRTI) approved in 1996, and it was found that if given as a monotherapy that resistance develops relatively quickly. But with nevirapine given as part of three-drug regimen, in which two NRTIs are also administered, HIV-1 was found to be nearly completely suppressed and proved superior to dual therapy NRTI control groups in the Italy, Netherlands, Canada, Australia Study (INCA Study) [43].

Different classes of ARV medications, which in turn could be given to patients in a variety of different combinations, ultimately proved the key in defeating HIV-1 conferred drug resistance. Such drug regimens become referred to as “highly active antiretroviral therapy” (HAART) and truly marked a turning point in the battle against the HIV-1 pandemic. A substantial decrease in HIV-1 associated morbidity and mortality associated with HAART administration changed the world: the leading cause of death among young people within developed countries had become augmented to a chronic but manageable affliction [44]. Perpetual variety in HAART treatment not only prevents HIV-1 for developing resistance to specific ARVs but also prevents HIV-1 replication to the point where plasma viral levels are undetectable [45]. To date, there are five different classes of antiretroviral medications: NRTIs, NNRTIs, PIs, entry/fusion inhibitors, and integrase inhibitors.

- NRTIs work to inhibit the enzyme responsible for the transcription of the viral RNA into DNA for integration. This is accomplished by NRTIs being nucleoside analogs; they compete with natural deoxynucleotides within the cell for incorporation into the growing DNA strand during reverse transcription. Such analogs lack the 3' OH group needed to successful chain elongation. When the next deoxynucleotide is incorporated into the growing DNA chain, the 5' to 3' phosphodiester bond needed for continuation cannot be formed. Failure to form this bond halts the process, effectively preventing viral RNA from being reverse transcribed. Currently approved NRTIs used in treatment of HIV-1 include: Zidovudine, Didanosine, Zalcitabine, Stavudine, Lamivudine, Abacavir, and Tenofovir. It should be noted that Tenofovir is a unique type of NRTIs and is more accurately described as a nucleotide reverse transcriptase inhibitor (NtRTIs). Nucleoside analogs normally undergo phosphorylation to be converted into nucleotides, which become active for incorporation. Tenofovir is administered as an already chemically active nucleotide analog, with no need for activation via phosphorylation
- Non-nucleoside reverse transcriptase inhibitors (NNRTIs) again inhibit the transcription of viral RNA into DNA but do so by more direct means. NNRTIs non-competitively bind to an allosteric site on reverse transcriptase, resulting in a confirmation change and inactivation of the enzyme. If given as a monotherapy, HIV-1 resistance to NNRTIs can be established fairly quickly due to mutations in reverse transcriptase during continual iterations of replication; mutations in which NNRTIs cannot bind to the RT allosteric site are positively selected for (REF). Because of this, NNRTIs are commonly given in conjunction with one or two other NRTIs. Currently approved NNRTIs include: Nevirapine, Delavirdine, Efavirenz, Emtricitabine, Etravirine, and Rilpivirine.

- PIs effectively prevent the maturation and release of newly synthesized viral proteins by inhibiting the enzyme needed for their cleavage and subsequent activation. As described above, once viral RNA has been reverse transcribed into DNA and integrated into the host genome, viral proteins are transcribed by host cell machinery to produce new viral particles. Newly synthesized viral proteins must become cleaved by the viral protease to become fully activated and infectious. PIs bind to the active site of viral proteases, preventing them from having enzymatic activity and inhibiting the completion of HIV-1 life cycle. Currently approved PIs include: Saquinavir, Ritonavir, Nelfinavir, Amprenavir, Lopinavir, Atazanavir, Fosamprenavir, Tipranavir, and Darunavir.
- Entry and fusion inhibitors are a relatively new class of ARV drugs with only 2 compounds currently being approved for HIV-1 treatment: Enfuvirtide, approved in 2003, and Maraviroc, approved in 2007. For entrance of HIV-1 into a host cell, viral envelope surface glycoproteins must interact with membrane surface receptors. HIV-1 envelope glycoproteins are normally a heterotrimer consisting of three molecules of gp120 and three molecules of gp41. Binding of viral gp120 to the CD4 receptor of a host cell causes a conformational change in the glycoprotein, allowing interaction with host cell co-receptors CCR5 or CXCR4. Co-receptor binding ultimately allows fusion between the host cell membrane and portions of gp41 within viral envelope. Enfuvirtide prevents this fusion event by changing the N-terminal heptad repeat of gp41 to an inactive hetero six helix bundle, preventing it's fusion interaction with the host cell membrane. Maraviroc utilizes an interaction with co-receptor CCR5, binding to it and preventing association with gp41, effectively inhibiting entry into cells with the CCR5 co-receptor.
- Integrase inhibitors were developed to block the enzyme responsible for the integration of newly synthesized HIV-1 DNA into the host cell genome. Integrase

catalyzes two reactions within the HIV-1 replication life cycle. The first is 3' end processing in which two nucleotides are removed from one or both of the 3' ends of the viral DNA, while the second is the "stand transfer reaction" in which the processed 3' ends are covalently bound to host chromosomal DNA. Inhibition of integrase prevents these steps from occurring, effectively preventing the infection of the host cell. Currently approved integrase inhibitors are: Raltegravir, Dolutegravir, Elvitegravir, and Bictegravir.

Despite such significant advancements in the development of HIV-1 treatment options, HIV-1 persists and remains yet to be completely eradicated. Thought HAART can reduce plasma viral levels to undetectable levels and allow patients to live decades after their initial infection and diagnosis, HIV-1 continues to persist throughout the world.

1.6 HIV-1 reservoirs

HIV-1-infected individuals receiving clinically effective ART must remain on such therapy continuously and uninterrupted for the entirety of their lives, despite the effectiveness of such drug regimens as described above. This can primarily be attributed to the ability of HIV-1 to escape immune surveillance and persist within latently infected immune cells in cellular and anatomical locations termed "HIV-1 reservoirs" [46]. Such reservoirs were discovered in the mid 1990's during the development of HAART, in which reports exhibited HIV-1 provirus residing within latently infected resting life-long memory CD4+ T lymphocytes [47]. Such cells have HIV-1 DNA integrated within their genome but are not actively producing new virions; rather they are in a latent resting state until they become activated weeks, months, or sometimes years after they initially become infected. Such latency renders the majority of current ARV therapy ineffective; inhibiting steps of viral replication has little consequence on cells that are not actively producing new virions. Indeed, HIV-1 patients who interrupt continuous ART display rapid viral plasma rebound even if plasma levels had been suppressed to undetectable levels for years [48]. Furthermore, such latently

infected immune cells often reside in anatomical locations that ARV therapy poorly penetrates, allowing for potentially high levels of replication within HIV-1 reservoirs [49]. Such latently infected and long lasting groups of immune cells can be categorized based on a commonality between the types cells they reside in, or the anatomical location large amounts of such cells accrue.

Different mechanisms have been proposed for the persistence and maintenance of HIV-1 cellular reservoirs. These include inadequate penetration of ARV drugs into tissues sites of active replication, replenishment of infected cells via residual viral replication, intrinsic stability of latently infected and resting CD4+ T-cells, and periodic homeostatic proliferation of cells in sanctuary sites located within various tissues compartments [50-53]. Overall, HIV-1 persists primarily within immune cells of two broad categories: CD4+ T-lymphocytes of a variety of functions including central memory, effector memory, transitional memory, and naïve CD4+ T-cells, as well as monocyte-derived macrophages. Anatomical locations of HIV-1 sanctuaries are also numerous and diverse, with HIV-1 persistence and replication being found in peripheral blood, peripheral lymphoid tissue, gut-associated lymphoid tissue, the reticuloendothelial system (RES), and the central nervous system (CNS).

1.6.1 Peripheral lymphoid tissue

Lymph nodes are a primary site for viral replication of HIV-1, with large amounts of infected cells and free virions being contained within the follicular dendritic cell network [29, 52]. HAART is effective in reducing HIV-1 RNA levels within lymph nodes, with a clearance half-life only marginally longer than that found in blood [54, 55]. However, both HIV-1 RNA and DNA can be detected within lymph nodes following years of viral suppression due to various combinational ART [56]. A multitude of different studies involving ART-treated SIV-infected rhesus macaques found that HIV-1 RNA and/or DNA levels are highest within the lymph nodes compared to other sanctuary sites such as plasma or the gut, with several of these studies finding

an association between high levels of viremia and low ARV concentrations within such peripheral lymphoid tissues [57-59].

1.6.2 Gastrointestinal tract and GALT

Following transmission of HIV-1, the gastrointestinal tract is one of the earliest targets of HIV-1 infection and is one of the tissues with the highest number of infected cells. This is primarily due to the gut containing a large portion of the lymphoid tissue and lymphocytes within the body [60, 61]. *In vitro* studies of isolated primary gut mucosal CD4+ T-cells not only show an increased susceptibility to HIV-1 infection but also support increased levels of viral replication [62, 63]. Such findings are attributed to these cells having increased T-cell activation and greater levels of CCR5 expression [64]. Clinical investigations of HIV-1 RNA and DNA levels within rectal biopsies showed the viremia remained stable over 1 year of ART, with gut HIV-1 DNA+ cells being twice that in blood [65]. Additional studies report HIV-1 DNA levels per million CD4+ T-cells were 5-6 times higher within the ileum compared with blood in patients that had been taking ART for up to 10 years [66]. Averaging the level of HIV-1 DNA across 4 separate gut sites, it was estimated that the gut harbors 83-95% of all HIV-1 infected cells within the body [67]. Again, such phenomena can be attributed both to the gut intrinsically having large amount of lymphocytes as well as poor penetration of certain ARVs into the gut.

1.6.3 Reticuloendothelial system

The reticuloendothelial system is also referred to as the mononuclear phagocyte system and consists primarily of monocyte and macrophage cells. While the RES encompasses multiple different immune cells within different tissue sites, for the purpose of this dissertation focus will be put on monocytes of bone marrow and peripheral blood, residual macrophages of the spleen, and Kupffer cells of the liver, as these are the areas of biological interest that are targeted in chapter 2 and chapter 3. Circulating monocytes terminally differentiate into mononuclear phagocytes (MP)

and, once associated with a particular tissue, no longer replicate [68]. The utility of MPs is primarily that of phagocytosis, in which cells engulf cellular debris and/pathogens and become antigen presenting cells (APC). While the percentage of MP cells that become infected with HIV-1 is quite low in comparison with that of CD4+ cells, the biological consequences of such infection are drastic [69]. Additional utility of MPs consist of the ability to infiltrate a large variety of different tissue sites: such cells containing HIV-1 would have a "trojan-horse effect" as they would carry HIV-1 into anatomical sites that free virions or even infected CD4+ T-cells would not be able to access, particularly the brain as discussed below. Therefore, infected MPs are significant contributors in the establishment of HIV-1 reservoirs. However, the migratory behavior of MPs, coupled with their large intracellular compartments, make them ideal targets in the establishment of drug depots, as discussed in later chapters. Multiple studies have confirmed that presence of infected Kupffer cells within the liver as well as the presence of infected red pulp macrophages within the spleen, with one study finding evidence of compartmentalization between the plasma and the spleen [70, 71].

1.7 Central nervous system as a major reservoir[1]

Of all the complications of HIV-1, the most foreboding and chronic issue is the disease's effects on the nervous system. Soon after the discovery and description of AIDS, neurological impairments were described and associated with advanced disease and profound immune suppression [72, 73]. These aggravations can often become severe with a triad of cognitive, motor, and behavioral disturbances [74-79]. Whether directly caused by the virus or indirectly misfolded and aggregated proteins, all of the processes discussed underlie the tempo and progression of disease [80-86]. A significant body of data has emerged in the past twenty five years on how HIV-1 affects the brain and causes progressive clinical impairment [72-74, 87-89]. Particular focus will

[1] This material was originally published in *Comprehensive Textbook of AIDS Psychiatry: A Paradigm for Integrated Care* edited by Mary Ann Cohen and Jack M. Gorman and has been reproduced by permission of Oxford University Press

be given here on how HIV-1 can pass the blood brain barrier (BBB) into the brain and the cellular targets of HIV-1 after entering the brain parenchyma.

1.7.1 Entry into the brain

HIV-1 is thought to gain entry to the protected environment of the CNS via a variety of different routes, and it is likely that HIV-1 invasion into the brain is achieved by utilizing more than one path [90-92]. Several mechanisms have been proposed by which HIV-1 gains entry into the brain [93]. In the most prominent and well supported theory, HIV-1 enters the brain inside infected macrophages, migrating into the brain parenchyma through BBB disruption and establishment of a chemokine gradient. This model is commonly referred to as the "Trojan horse hypothesis," as HIV-1 buds into intracytoplasmic vesicles in macrophages with limited expression of viral proteins on the cell surface, allowing for escape from immune surveillance [94, 95]. An alternative theory is that cell-free HIV-1 virus directly infects the endothelial cells and astrocytes of the BBB, however, this model is partially flawed as there is low or nonproductive infection of cells of the BBB [96]. In another model, the transcytosis model, HIV-1 invades the CNS through internalization of the virion by endothelial cells or by astrocyte foot processes by macropinocytosis or endosomes, with subsequent transfer of the virus to CNS cells [97]. In the brain, monocyte-derived perivascular macrophages are the main cell type infected by HIV-1, with limited expression in microglia and restrictive/non-productive replication within astrocytes [20, 98, 99]. The virus replicates within the infected macrophages and can infect other CNS cells, particularly other macrophages that perpetuate the infection within the CNS. Astrocytes and capillary endothelial cells have been found to contain HIV-1 protein and DNA in infected individuals [20]. Depending on the number of infected brain macrophages, the extent of CNS inflammation, and the number of recruited monocyte-derived macrophages, the course and extent of neurological impairment can be tentatively predicted.

It has been suggested that the early CNS HIV-1 infection has the possibility of inducing

immune activation of the brain parenchyma, resulting in a subsequent increase in the number of microglial cells, up-regulation of MHC class II expression, and local production of cytokines. In the normal CNS, neurons, oligodendrocytes, astrocytes, and microlgia are intimately associated with each other and communicate through specialized synapses and cell junctions; this direct cell contact is required for proper glia maturation and function [100-102]. For glia to undergo transformation to an activated amoeboid phenotype, they need to be freed from inhibitory neural and astrocytic responses [25]. Activated microglia and, to a lesser extent, astrocytes express MHC class I and II antigens and adhesion molecules and secrete cytokines and reactive oxygen intermediates, and all have been shown to be important factors contributing to HAD [25, 103, 104]. Microglia and astrocytes produce chemokines and control monocyte migration across the BBB [105-109]. The event(s) triggering monocyte invasion into the nervous system likely involves the secretion of macrophage attractant chemokines and the up-regulation of adhesion molecules on activated endothelial and immune cells. Proinflammatory factors induce cytokines and chemokines (such as IL-8, IFN-γ, IP-10, growth-related oncogene α [GRO-α], MIP-1a, MIP-1b, RANTES, and MCP-1) found in infected brain tissue and may also participate directly in the disease process. Both cytokines and HIV-1 Tat induce expression of E-selectin on BMVEC. The likelihood of this event is increased by the release of nitric oxide (NO). TNF-α and Il-1β also induce expression of VCAM-1 on the BMVEC [110]. This induction of adhesion molecules allows binding of HIV-1-infected cells to the brain endothelium. Virus and activated macrophage entry into the brain is likely precipitated by BBB damage heralded by activation of brain MP. Neuronal damage and alterations in the integrity of tight junction and/or regulation of its immune function occur as consequences of viral and cellular secretory products and are crucial to HIV-1 brain transport [109].

The BBB consists of a monolayer of specialized, non-fenestrated, microvascular endothelial cells. Associated with the BBB is a capillary basement membrane on the abluminal side of the monolayer, with tight junctions connecting the BMVEC and no transcellular pores [111].

These together serve to restrict movement of cells and macromolecules, including viral particles, throughout much of HIV-1 infection. Nonetheless, a number of biological situations enable the aberrant trafficking of cells across the BBB as a result of HIV-1 infection, allowing for the virus to enter the brain. The movement of viral particles from the periphery into the brain is facilitated through immune and structural BBB compromise. This process occurs late in the course of disease and serves to speed the overall pathogenic process of the disease. HIV-1 infection alters the BBB itself; numerous functional and structural abnormalities are of consequence, including damage to the basement membrane, damage to tight junction proteins, morphological and functional alterations of the BMVEC, and subsequent protein leakage [112-117]. As a result, HIV-1-infected monocytes and/or CD4+ T lymphocytes as well as cell-free virus are able to cross the BBB [114, 118].

Inflammation also serves to enhance trafficking of cells across the BBB. ICAM-1, VCAM-1, and E-selectin are up-regulated on the surface of BMVEC and astrocytes after exposure to proinflammatory factors secreted from microglia and astrocytes and/or activated leukocytes from the periphery; these serve to augment the process of adhesion molecule expression on not only BMVEC but astrocytes as well [106, 119]. Late in the disease process, inflammatory cytokines are produced at high levels and allow the BBB to be more easily breached. These proinflammatory cytokines induce a transient increase in endothelial permeability by increasing secretion of endothelial vasoactive factors, such as NO [120]. TNF-α and IL-1β increase the production of other inflammatory mediators, including arachidonic acid–derived PAF [106, 107, 121]. These serve to promote monocyte migration across the BBB and ultimately into the brain parenchyma. The adhesion molecules ICAM-1 and VCAM-1 on the luminal surface of the BMVEC bind LFA-1 and Vl-4 on the monocyte, resulting in migration of the monocyte between the endothelial cells during the early stages of viral infection.

Changes in cellular physiology that are induced as a consequence of inflammation also

influence transmigration of inflammatory cells into the CNS. Chemokines are secreted at sites of inflammation in all tissues and work to guide leukocytes in a concentration-dependent manner[122-124]. Importantly, specific chemokines will attract specific populations of leukocytes. MIP-1α and MCP-1 levels are increased during HIV-1 encephalitis and are potent chemoattractants for macrophages as well as CD4+ T lymphocytes [121, 125]. Increasing damage to the BBB impairs its ability to protect the CNS from the periphery resulting in cells and toxins being able to reach the CNS unchecked. Levels of inflammatory factors greatly increase and lead to a cascade of events culminating in further BBB dysfunction. These processes, taken together, affect MP-induced neuronal destruction during HAD.

The Trojan horse hypothesis is based on the concept that infected monocytes and lymphocytes act as cellular vehicles that can transport HIV-1 across the BBB, crossing from the periphery to the CNS. The specific mechanism of this process has not been completely elucidated, however, observations as well as a substantial body of scientific data support this claim. Monocytes and CD4+ lymphocytes the primary target of HIV-1 infection outside of the CNS, and analysis of HIV-1 infected brains have found large accumulations of HIV-1 infected macrophages within neuronal tissue [126-128]. Expression of adhesion molecules as well as chemo attractants within the CNS is higher in individuals experiencing HIV-1 dementia, allowing increased interactions between infected leukocytes and brain endothelium plus increased recruitment of these monocytes for transmigration [129].

These observations converge into the idea of a “snowball” like effect, in which initial HIV-1 invasion occurs in very small amounts, with increasing levels of invasion facilitated by signaling initiated by the resulting microenvironment of the initial migrating infected cells. Indeed, several groups have reported findings supporting this claim. HIV-1 infection of human peripheral blood monocytes resulted in higher expression levels of LFA-1, and factors released by these infected cells induce expression of adhesion molecules E-selectin and VCAM by endothelial cells [96, 112,

130]. Upon immunohistochemical analysis of HIV-1 infected brain tissue, E-selectin levels were substantially increased in HIV-1-demented individuals as compared to non-demented patient's brain samples [115, 117].

Chemokines play a vital role in the transmigration process, and studies have reported aberrant expression levels of both chemokines and their respective cell surface receptors in HIV-1 infected leukocytes [101, 123]. Monocyte chemotactic protein 1, or MCP-1 (also referred to ass CCL2) has long been established as a principal attractant for monocytes and activated t-cells, and studies have indicated that it is integral for monocyte transmigration into the brain parenchyma [131]. Analysis of CSF from HIV-1 infected patients exhibiting dementia found elevated levels of MCP-1 [132, 133]. These findings, taken together, indicate that adhesion molecules and chemokines likely play an important role in facilitating leukocyte transmigration and subsequent invasion of HIV-1 into the CNS.

Although the major targets of HIV-1 in the brain are macrophages and microglia, there have been some reports of other cells of the brain being infected by HIV-1, including the endothelial cells of the BBB [134, 135]. This highlights another theory of HIV-1 entry into the CNS; direct infection of perivascular endothelial cells and astrocytes within the blood brain barrier. The support for this hypothesis is weak, and suggests that this route of viral entry occurs only in small amounts, most likely in conjunction with the other entry mechanisms discussed. Groups have reported that in HIV-1 infected patients, brain microvascular endothelial cells (BMVECs) have exhibited dysfunction and rampant apoptosis [136, 137]. Astrocyte viral infection is very low and often results in minimal reproduction of the virus, however, several studies have demonstrated that astrocytes that do become infected increase toxicity and inflammation surrounding CNS cells, thus propagating HAND pathology [129]. It is also possible that infection of astrocytes occurs only the late stages of the disease, long after the initial invasion of the virus, as one study concluded that up to 19% of astrocytes were infected with in patients exhibiting dementia; this same study also found

correlation between areas of HIV-1 infected astrocytes and increased rate of macrophage/monocyte transmigration [134]. Based on these findings, it is unlikely that direct infection of endothelial cells and astrocytes is the main mode of HIV-1 entry into the CNS. However, it is plausible that these cells, once infected, can participate in subsequent infection of other cells in the CNS and lend a hand in the creation of a viral reservoir.

Another possibility of HIV-1 invasion into the CNS is that transcytosis, in which endothelial cells or astrocytes absorb the HIV-1 virion via macropinocytosis or endosomes and mediate transfer to CNS cells. While the basic idea of this hypothesis is supported with compelling data from multiple groups, the precise mechanism has yet to be determined and is entangled in controversy within the scientific community [138, 139]. One group has reported the process being pH independent and thus non-endosomal, while others have indicated for a pH dependent mechanism [114, 140]. *In vitro* studies using electron microscopy have shown viral particles localized within structures comparable with endosomes [114]. Increased surface microvilli of brain endothelial cells and increases in numbers of cytoplasmic vesicles are indicative of macropinocytosis, with both findings demonstrated experimentally *in vitro* [141]. While it is evident that endothelial cells and astrocytes have the capability to acquire HIV-1 by transcytosis, how these cells transfer and propogate infection of the virus to other cells within the CNS has yet to be investingated.

1.7.2 HIV-1 targets within the CNS

1.7.2.1 Mononuclear phagocytes

The pathogenesis of HIV-1-associated CNS disease centers around mononuclear phagocytes (MPs), which include blood borne macrophages, dendritic cells, tissue macrophages, and microglia.. Macrophages are the principal cell infected in the brain and become activated and recruited into tissue during inflammation and emigrate into the CNS during disease [128, 142]. This influx is usually transient, however, and will revert to a quiescent state after the inflammatory

process has subsided. For HIV-1-encephalopathy and HIV-1 associated dementia (HAD), the process never subsides, as brain inflammation is continuous and induced by ongoing viral replication. Mononuclear macrophages are preferentially infected by HIV-1 due to their CD4 receptor and CXCR4 co-receptor; both of which help mediate the fusion of the HIV-1 envelope with the host cell membrane. Subsequent activation and differentiation into macrophages further increases the efficiency in which these cells replicate and spread the virus [126, 143]. Such cells, once in the CNS, initiate a "pull" mechanism of activation and recruitment via chemotactic and inflammatory signals such that more monocytes are attracted to the brain, increasing the amount of HIV-1 as well as activating and infecting other cells within the CNS.

The perivascular macrophage is an actively studied MP cell type with involvement in HAD pathogenesis. Normally these cells exist between the glia limitans and basement membrane of the choroid plexus and CNS capillaries and are derived from circulating monocytes. Because of their anatomical proximity to cerebral vessels in the brain, perivascular macrophages are likely susceptible to HIV-1 that crosses the BBB [144]. .They are in close association with the bone microvascular endothelial cells (BMVEC), and this collaboration allows them to serve as sentinels for the CNS. In fact, perivascular macrophages act as intermediates between the peripheral circulation and the microglia. Since microglia are in contact with these macrophages, signals may be rapidly communicated deep into the CNS from interactions at the perivascular space. Transmission of virus and/or inflammatory responses in the brain may occur between these perivascular macrophages and glial cells [20, 128, 145].

Parenchymal microglia occur in significant numbers in the CNS and may constitute up to 10% of CNS cells. These cells enter the CNS during gestation and have a very low turnover rate [100, 128], in contrast to perivascular macrophages, which are continuously replenished from the bone marrow. Parenchymal microglia act as the resident macrophages within the brain and are responsible for the primary immune response within the brain. Normally, parenchymal microglia

and macrophages in the CNS are easily distinguished from each other by morphology, but activation of microglia results in them displaying macrophage-like properties [146]. There are two morphological subtypes of microglia. The first, ramified microglia, are resting cells with reduced secretory and phagocytic activity making up the web of microglia that span the CNS [146, 147]. In contrast to perivascular macrophages, they have weak antigen-presenting capability. The second morphological subtype, amoeboid in form, is a morphological intermediate and transitional cell between the ramified microglia and the brain macrophages [146]. This subtype is not found in the normal adult CNS but rather in inflammatory and demyelinating conditions.

Infection of brain MPs eventually leads to the formation of multinucleated giant cells (MGC). These cells result from the fusion of HIV-1-infected brain MP with uninfected monocyte-derived macrophages (MDM) or microglia [99, 128, 148]. This fusion is mediated by HIV-1-envelope glycoproteins present at the surface of infected cells with CD4 and chemokine receptors at the surface of uninfected cells [15, 149-151]. The MGCs are large, irregularly round, elongated or polyhedral, with dense eosinophilic cytoplasm in the center and vacuolated at the periphery [148]. MGC formation is found throughout the brain in HIV-1 disease, but is characteristically seen primarily in the deep brain structures and most commonly in subcortical white matter. Although pathognomonic of HAD, giant cells are only found in 50% of patients [25, 26, 152].

1.7.2.2 Astrocytes

Astrocytes are critical for the survival of neurons and their function may be impaired in the context of HIV-1 infection. Astrocytes are responsible for maintaining homeostasis in the CNS and are important in the detoxification of excess excitatory amino acids such as extracellular glutamate levels [153, 154]. However, infected astrocytes can produce cellular factors that may adversely affect neuronal survival [121, 155, 156]. Astrocytes play a dual role in the pathogenesis of HIV-1-related encephalopathy; in HIV-1 infection, astrocyte glutamate reuptake is impaired, possibly due to interactions with infected macrophages. However, glutamate release in astrocytes is also induced

by activated macrophages [157]. Activation of the CXCR4 receptor by stromal cell-derived factor 1 (SDF-1) results in the release of extracellular TNF-α and downstream release of glutamate [157]. During HIV-1 infection there is an amplification or regulation of neurotoxic signals among astrocytes and microglia. The HIV-1 protein Tat induces expression in astrocytes of MCP-1, a chemoattractant for macrophages, and IL-8 and inducible protein-10 (IP-10), which attract multiple leukocyte types [124, 132].

Astrocytes both proliferate and undergo apoptosis in HIV-1 CNS infection [154]. The level of astrocyte apoptosis correlates strongly with both the severity and rate of progression of HIV-1 dementia. Direct infection of astrocytes by HIV-1 is minimal due to an absence of the CD4 receptor [158]. Although studies have reported that infection of astrocytes can be both productive and unproductive, recent studies have concluded that productive HIV-1 infection of astrocytes is infinitesimally small, with .0025% of brain astrocytes undergoing productive infection [134, 158]. HIV-1 virus enters these astrocytes via endocytosis in which endosome internal machinery degrades the majority of the viral particles; thusly HIV-1 astrocytic endocytosis is seen as a "kiss of death", as only a very small amount of viral particles survive and establish a productive infection [158]. Unproductive infection of astrocytes occur more frequently, with groups reporting 3-19% of astrocytes within infected brain tissue carrying HIV-1 DNA [134, 159].

1.7.2.3 T-cells

. CD4+ T cells serve as important reservoirs of HIV-1, as a small proportion of these cells harbor HIV-1 in a stable, inactive form. Normal immune processes can activate these cells, resulting in the production of new HIV-1 virions. After transmigration through the BBB, T cells are able to instigate cell-to-cell spread of HIV-1 through CD4-mediated fusion of an infected cell with an uninfected cell. In addition, phagocytosis of CD4+ T cells by MP can result in the spread of virus [160, 161]. Activated T cells penetrate the BBB

after insult to the CNS and can initiate both protective and toxic inflammatory responses [162]. Protective responses are elicited through elimination of the ongoing infectious agent by innate, humoral, and cytotoxic immune activities. Nonetheless, widespread inflammation in the setting of HIV-1 often leads to damage of the BBB and further transendothelial migration of leukocytes entering the nervous system [109]. Inflammation of the brain and spinal cord actively attracts T cells to the CNS. Macrophage inflammatory protein-1 alpha (MIP-1α) and MIP-1β are relevant to the cellular recruitment and immune activation during HIV-1 infection, as both use CCR5 as their receptor [122, 163-166]. MIP-1α selectively attracts CD8+ and MIP-1β recruits CD4+ lymphocytes. Both MIP-1α and MIP-1β are produced by HIV-1-infected monocytes and are closely linked to viral replication [125].

During HIV-1 infection, more T cells are activated to a blast phase [167-169]. Once within the CNS, the lymphoblasts search for antigen as they migrate through the parenchyma. Such cells can easily encounter and engage perivascular macrophages through direct cell-to-cell contact or through soluble factors released. CD4+ T lymphocytes are responsible for most of the HIV-1 replication in the periphery, and HIV-1 may enter the CNS in infected lymphocytes during the late stage of the disease. As the T cells migrate through the parenchyma, they secrete the cytokines that lead to activation of MP and an amplification of inflammatory cell responses throughout the CNS region involved [170]. If these activated T cells are infected, they will shed virus as they migrate. At the same time, they induce CD4 expression on cells susceptible to HIV-1 infection, rendering them even more susceptible. T cells expressing the CD40 ligand (soluble and bound forms) can activate both infected and noninfected monocytes that express TNF-α and CD40 receptors [167, 171, 172]. Macrophages become activated by way of scavenger receptors as they clear the debris of dead virus-infected cells [12, 161]. Since viral replication occurs mostly within CD4+ T cells,

direct cytopathic effects of HIV-1 may be attributed to cell death [173]. The decline in CD4+ T lymphocytes allows macrophages, without control, to express a metabolically active, tissue-destructive phenotype.

1.8 ART associated neurotoxicity

While it is likely that HIV-1 invasion into the brain and a subsequent inflammatory cascade is responsible for the development of adverse neuropsychiatric events in infected patients, other potential mechanistic causes are certainly possible. Such reasoning is a result of the prevalence of HAND remaining consistent in groups of infected individuals despite the introduction of HAART, with 15-55% of HIV-1+ individuals estimated to have HAND, a proportion comparable to the pre-cART era [89, 174]. It should be noted that more recent HAND cases in the era of HAART represent more milder forms of the condition, however, additional studies have indicated that HAND becomes more prevalent and severe as patients grow older [89, 174]. Additional risk factors for the development of HAND include cardiovascular disease, age, co-infection of hepatitis C, substance abuse, and concomitant psychiatric illnesses [175]. Therefore, it is likely that the onset of neuropsychiatric complications is multifactorial, with many causes working in tandem to propagate HAND in HIV-1 infected patients. A potential contributor to HAND pathology not yet discussed is that of the antiretroviral medications themselves. Indeed, while the introduction of cART has resulted in a marked reduction in morbidity and mortality in HIV-1 infected patients, the off target effects can be quite substantial [176, 177].

Unfortunately, little information on the effects of antiretrovirals within the CNS is available, with studies of off target neurotoxicity in ART cohorts being reported only within the past decade [178]. This can partly be attributed to more recent ART development being focused on drugs that can pass the BBB to readily control the HIV-1 CNS viral reservoir; increasing ARV concentrations in the brain would result in decreased CNS viremia, subsequently leading to a decrease in adverse neuropsychiatric events based on mechanisms described above. Based on

previous observations of severe AIDS associated dementia seen in the pre ART era, it would seem that decreased ARV brain concentrations causing less neuropsychiatric problems would be the opposite expected effect. However, one such study found exactly that. In a group of immunologically and virologically suppressed patients, researchers found that patients reported improved cognitive abilities for up to 96 weeks following election to cease treatment [179]. Such findings were opposite of the groups expected hypothesis and raised the possibility that low ARV concentrations within the brain, while effectively reducing brain viremia, can have some detrimental effects.

The NNRTI Efavirenz has long been considered an excellent antiretroviral particularly when used in combination, such as Combivir (lamivudine/zidovudine), Kivexa (abacavir/lamivudine), and Truvada (tenofovir/emtricitabine) [180]. While these therapies are extremely effective at systemically reducing viral load, the most consistently reported side effect of efavirenz is neurotoxicity, with one study reporting 40-60% of patients on efavirenz having CNS toxicity, and 25-40% exhibiting psychiatric effects [181]. In multiple studies the number of CNS effects attributable efavirenz is almost double that of other antiretrovirals it was compared to [182-184]. These off-target toxicities within the CNS contribute to a higher numbers of discontinuation of therapy compared to newer, less toxic drugs, further compounding problems with HIV ART compliance.

Additional studies investigating ARV neurotoxicity have found that a variety of antiretrovirals have exhibited toxic effects on neurons; however, such studies were performed on *in vitro* neuronal cultures and as such conclusions are limited. Highest neurotoxicity within neurons was seen in abacavir, efavarenz, etravirine, nevaripine, and atazanavir, with some toxic concentrations overlapping drug levels clinically found within the CNS of patients [178]. In general, clinically relevant concentrations showed modest levels of toxicity. Nonetheless, such findings indicate the need for careful studies of the effects of ARV compounds at concentrations

required to suppress viral replication and to guide the use of compounds that will minimize CNS complications.

Dolutegravir, a potent integrase strand inhibitor, is one of the more recent ARV drugs to come to market with its medical use being approved in 2013. DTG readily crosses the BBB and has been found to accumulate within CNS tissues. Additionally, some of the more commonly reported side effects of DTG administration is that of headache and insomnia. Though these off target effects are minor and generally well tolerated, they still raise concern of DTGs contribution to adverse neuropsychiatric events in HIV-1 patients. Furthermore, a recent study following DTG administration to women at the time of conception exhibited a potential increased risk for neural tube defects in their newborns [185].

1.9 Theranostics

Over recent decades, nanotechnology has garnered a considerable amount of interest within the scientific community, with medical research being no exception. Indeed, the ability to reliably and consistently produce materials with dimensions and tolerances of less than 100 nanometers (nm) has proven extremely useful across a diverse multitude of research fields. The impact nanotechnology has had on medicine, both in research laboratories and within the clinical landscape, cannot be understated. Constant innovation in the synthesis and characterization of nanoscale materials has resulted in products with high amounts of utility.

However, until recently, nanotechnology developed for medical purposes has largely been one-dimensional. Development and production of nanomaterials were done for the utilization of a single function; to diagnose and/or provide information on a disease state, or to provide therapy for the treatment of a disease state [186]. These nanoscale diagnostic agents and nanomedicines have proven to be independently useful, with particular success being found in sequential utilization of their single functions. To first make a diagnosis and acquire details on the progression of a disease, and then to administer specific, personalized treatments to abrogate and possibly eliminate said

disease based on previously acquired diagnostic information, has proven useful in patient management. But these independent functions, diagnosis and therapy, have required independent nanomaterials. Such a two-part strategy has proven ineffectual for disease states with diverse presentations within the clinic and complicated underlying pathology. Furthermore, the most significant diseases impacting humanity today have complex disease progressions.

The term “theranostics” was coined from the concept of combining both therapeutic and diagnostic nanomaterials into a single platform [187]. Such combination would allow both nanomaterials to be delivered together, allowing for concurrent treatment and monitoring of a disease state. Theranostics is a cornerstone strategy for personalized medicines, allowing for identification of subgroups of patients with specific clinical profiles that are most likely to respond to specific therapies, while also identifying within those same subgroups patients that would have adverse reactions to these same therapies [186].

We developed theranostic nanoparticles for real-time tracking of therapy biodistribution in the treatment of HIV-1. Termed “multi-modal imaging theranostic nanoprobes”, such nanotechnology allowed combined bioimaging, drug pharmacokinetics, and tissue biodistribution tests in animal models [188]. Individual components include a diagnostic paramagnetic contrast agent in cobalt ferrite, a diagnostic fluorescent component in incorporated Europium (Eu^{3+}), and HIV-1 therapy in nanoformulated dolutegravir (DTG). Brief descriptions of each of these components are described below.

1.9.1 Paramagnetic and superparamagnetic contrast agents

Magnetic resonance imaging (MRI) has proven to be a powerful and non-invasive diagnostic modality since it’s development in the 1970’s [189]. MRI utilizes strong magnetic fields, magnetic field gradients, and radio waves for interaction with the protons within a living organism, allowing for generation of internal images. Specifically, MRI generates contrast based on intrinsic differences between different tissue regions such as T_1 (spin-lattice) and T_2 (spin-spin) relaxation

times, and proton density. In some disease states, it is possible to differentiate diseased tissue from healthy tissue based on disease's effect on these intrinsic differences. However, often times the effect of disease pathology on these factors is too limited for any meaningful diagnostic information to be discerned from the resulting images. Because of this, multiple "contrast agents" have been developed that can drastically change the intrinsic relaxation times of specific tissues.

"Paramagnetic" materials can be defined as those that are weakly attracted by an external magnetic field and form internal, induced magnetic fields in the direction of a specific applied magnetic field [190, 191]. Paramagnetic contrast agents include manganese (Mn^{2+}) and gadolinium (Gd) that substantially shorten T_1 relaxation of water protons, creating a brightened contrast in T_1 weighted MR images. Superparamagnetic contrast agents such iron oxide particles or cobalt ferrite nanoparticles shorten T_2 relaxation times of water protons, creating a "darkening" effect on T_2 weighted MR images [192]. Additionally, superparamagnetic contrast agents show much more magnetic susceptibility compared that paramagnetic contrast agents, leading to an increase in magnetic sensitivity.

1.9.2 Fluorescence

Fluorescence can be defined as a substance emitting light of a specific wavelength after said substance has absorbed light or other electromagnetic radiation. Utilization of such a property has proven useful in biological sciences, as application of fluorescent materials to a vehicle allows for non-destructive tracking or analysis through different biological pathways. This can be performed at specific emission frequencies in which there is no background from excitation light, as very few biological components are naturally fluorescent. Such "fluorescent labeling" can be done via a very large variety of different fluorophores such as dyes and fluorescent proteins, each with a unique excitation and emission wavelength, molecular weight, and quantum yield [193]. Additionally, specific elements exhibit intrinsic fluorescence. Rare-earth doped phosphors such as Terbium, Cerium, Lanthanum, and Europium form the basis for fluorescent lighting [194].

Incorporation of rare earth element Eu^{3+} into our nanoparticle vehicle proved particularly useful, exhibiting fluorescence and emission wavelengths at 410 nm and 660 nm, respectively. Europium doping within the spinel ferrite structure of our theranostic nanoparticles allowed for subcellular tracking using both *in vitro* and *ex vivo* confocal microscopy, as described in both chapter 2 and chapter 3

1.9.3 Nanoformulated ARVs

The final component of our theranostic nanoparticles was that of nanoformulated ARV drug, specifically the integrase inhibitor dolutegravir. Considerable innovation has occurred in the production of long-acting ART regimens in efforts to reduce secondary toxicities, improved drug adherence, and prevent new infections [195]. Ultimately, such goals center on drastically increasing the half-life of ARV drugs by improving upon their hydrophobicity. Formation of cell and tissue penetrate nanocrystals that are protected by biodegradable polymers allow the establishment of drug depots within monocyte-macrophages, prolonging drug half-life. [195, 196] However, a major drawback of developing long-acting ARV formulations is that biodistribution and pharmacokinetic studies, often taking weeks to months, are tedious and burdensome. Incorporation of long acting ARV drug into theranostic nanoparticles, in conjunction with other components, allows a much more rapid screening of tissue biodistribution and pharmacokinetics, subsequently resulting in much more timely pharmacodynamic improvements.

CHAPTER 2

Synthesis, characterization, and *in vitro* testing of multi-modal theranostic nanoformulations

2.1 Introduction

A major unmet need in the treatment of HIV-1 infection rests in long-term adherence to antiretroviral therapy (ART). If brought into clinical practice, long-acting ART regimens would substantively improve drug adherence, reduce secondary toxicities and prevent new infections. These could ultimately facilitate the realization of an AIDS-free world [195, 197-201]. In efforts to complete this task, we improved the hydrophobicity of existing antiretroviral drugs (ARVs), leading to the formation of cell- and tissue-penetrant nanocrystals protected inside biodegradable polymers. These were made to establish drug depots within monocyte-macrophages [202-207]. A critical component for formulation development rests, in measure, on nanoparticle decoration with macrophage-targeting moieties in order to best facilitate drug reservoir targeting. Such advances, if realized, will speed the development of eradication measures or, at the least, make therapeutics more accessible to larger patient populations. However, a significant obstacle remains in the ability to rapidly screen drug formulation tissue biodistribution and pharmacokinetics (PKs) in order to realize substantive pharmacodynamic (PD) improvements. This is of particular importance as, while the half-lives of each of the few existing long-acting drugs measure in weeks or even months, drug tissue distribution is limited [200, 208-212]. To overcome these technical and biologic challenges, multimodal decorated nanoparticles were produced where hydrophobic ARVs and bioimaging agents were encased in a single nanoformulation. All were placed into one "multimodal imaging theranostic nanoparticle" using core-shell construction methods [213]. The surface of the particle was coated with lipids decorated with targeting moieties, while the drug and image contrast agents were incorporated into a polymeric core. The formed particles were rapidly taken up by macrophages. Specifically, europium (Eu^{3+}) doped cobalt ferrite (CF, EuCF) crystals and

hydrophobic drug dolutegravir (DTG) were packaged in a polycaprolactone (PCL) core. A lipid layer coated the particle's "shell". L-α-phosphatidylcholine (PC), 1,2-distearoyl-phosphatidylethanolamine-methyl-polyethyleneglycol conjugate-2000 (DSPE-PEG2000) and 1,2-dioleoyl-sn-glycero-3-phosphoethanolamine (DOPE) lipids enhanced particle biocompatibility and lipophilicity, facilitating macrophage targeting [214]. Macrophage receptors sped entry of the ligand-coated drug particles. The folic acid (FA) receptor on macrophages enhanced particle cell entry [215-220]. Nanoparticles were produced with consistent size and stability, reflected in long-acting slow effective drug release (LASER) ART profiles [202, 206]. This enabled depot formation for viral reservoir targeting [206]. Overall, the newly generated theranostic nanoparticles provided a platform for effective nanoformulated ARV development.

2.2 Materials and methods

2.2.1 Reagents

Iron(III) acetylacetonate (Fe(acac)3), cobalt(II) acetylacetonate (Co(acac)2), europium(III) nitrate hydrate (Eu(NO3)3·5H2O), folic acid (FA), oleic acid, oleylamine, lipopolysaccharide (LPS), poly(vinyl alcohol) (MW 30,000-70,000, 87-90% hydrolyzed), L-α-phosphatidylcholine (PC) (from egg yolk), 3-(4,5-dimethylthiazol-2-yl)-2,5-diphenyltetrazolium bromide (MTT), dicyclohexyl-carbodiimide, N-hydroxysuccinimide, low gelling temperature agarose, coumarin-6, iron and cobalt standards for ICP-MS (TraceCERT®) and nitric acid (TraceSELECT®) were obtained from Sigma-Aldrich, St. Louis, MO, USA. Polycaprolactone (PCL) (MW 43,000-50,000) was obtained from Polysciences, Inc. Warrington, PA, USA. 1,2-Distearoyl-phosphatidylethanolaminemethyl-polyethyleneglycol conjugate-2000 (DSPEPEG2000) and 1,2-dioleoyl-sn-glycero-3-phosphoethanolamine (DOPE) were obtained from Corden Pharma International, Plankstadt, Germany. DTG was obtained from BOC Sciences, Shirley, NY, USA. 1,2-Distearoyl-sn-glycero-3-phosphoethanolamine-N- [amino(polyethyleneglycol)-2000] (DSPE-PEG2000- NH2) was obtained from Laysan Bio Inc. Arab, AL, USA.

2.2.2 Synthesis of DSPE-PEG$_{2000}$-FA Conjugates

FA-modified DSPE-PEG2000 was synthesized by a multi-step process. FA was activated by conversion to a N-hydroxysuccinimide ester (NHS-FA) [221]. FA (237 mg; 0.536 mmol, 1 equiv.) was dissolved in 10 mL of anhydrous dimethyl sulfoxide (DMSO, 10 mL) and triethylamine (80 µL, 0.569 mmol, 1.1 equiv.) and allowed to stir at room temperature for 18 h under argon and protection from light [222]. Dicyclohexylcarbodiimide (111 mg; 0.533 mmol, 1 equiv.) and N-hydroxysuccinimide (123 mg; 1.0 mmol, 2 equiv.) were added to the FA solution then stirred for an additional 16 h. The resulting NHS-FA solution was separated from insoluble dicylohexylurea by filtration then reacted with DSPE-PEG2000-NH2 (500 mg; 0.179 mmol, 0.3 equiv.). The mixture was stirred for 3 days at room temperature under argon and light protection. The DSPE-PEG2000-FA conjugate was precipitated from ether (~150 mL) and collected by centrifugation at 215 × g for 15 min. The pellet was dried under vacuum, dissolved in methanol (~25 mL) and purified on a sephadex LH-20 column using a coumarin-6 dye as an indicator. The purified product (~200 mL volume) was precipitated from ether and collected by centrifugation at 1950 × g for 10 min. The resulting pellet was lyophilized (Labconco Freezone 2.5, Kansas City, MO, USA) for two days and yielded a light yellow powder. Covalent linkage of FA to DSPE-PEG2000-NH2 was confirmed by 1H-NMR (Bruker Avance III HD, 500 MHz in deuterated DMSO). The final DSPE-PEG2000-FA conjugate was stored at 4 °C

2.2.3 Production of EuCF-DTG "core-shell" nanoparticles

EuCF nanoparticles of 7.2 nm size were fabricated using solvothermal techniques [223] and characterized for hydrodynamic size, size distribution, shape, structural configurations, morphology, chemical composition and superparamagnetic properties. EuCF-DTG "core-shell" nanoparticles were synthesized using a modified solvent evaporation process [213, 224]. Specifically, PCL (400 mg), DTG (30 mg) and EuCF (20 mg) were dissolved in DCM, methanol and chloroform (oil phase), respectively. Fresh lipid mixtures were prepared by dissolution of PC

(50 mg), mPEG2000-DSPE (25 mg) and DOPE (25 mg) in 5 mL of chloroform by bath sonication. A EuCF-DTG primary emulsion was prepared by mixing EuCF, PCL and DTG solutions with stirring for 6-8 h at 140 × g at room temperature. The secondary emulsion and shell layers for core nanoparticles were prepared by making a thin film of lipids (PC, PEG2000-DSPE and DOPE) in a round bottom flask through rotary evaporation (Büchi Rotavapor R-II, New Castle, DE, USA) of chloroform followed by overnight vacuum-drying. The primary emulsion of EuCF-DTG was then transferred into 30 mL of freshly prepared 1% (w/v) PVA and mixed by probe sonication (Cole-Parmer, Vernon Hills, IL, USA) at 20% amplitude for 10 min in an ice bath. The PVA served as a surfactant in this emulsification step. The core nanoparticles were then transferred into the flask containing the lipid film. The flask was steadily rotated with the core nanoparticles in a bath sonicator followed by probe sonication at 20% amplitude for 10 min in an ice bath. Evaporation of DCM was carried out under pressure at 35°C followed by overnight stirring. The nanoparticles were purified by centrifugation of the suspension at 55 × g for 10 min, followed by centrifugation of the supernatant at 35,1315 × g for 30 min at 10°C (Sorvall, Lynx-4000 super speed centrifuge, Thermo Fisher Scientific, Waltham, MA, USA). The pellet was washed twice with PBS, resuspended in PBS and stored at 4°C. For preparation of FA-EuCF-DTG nanoparticles, 25 mg of DSPE-PEG2000-FA was used and the remainder of the synthesis followed the preparation of the EuCF-DTG nanoparticles. For drug quantification from nanoparticles, ~30 mg of lyophilized nanoparticles was dissolved in 10 mL of DCM: methanol (1:1 v/v) mixture. The mixture was then bath sonicated for 30 min followed by centrifugation at 35,1315× g for 30 min. The supernatant was collected and DCM was evaporated at room temperature. The drug in methanol was quantified by HPLC.

2.2.4 Nanoparticle characterization

Powder X-ray diffraction (XRD) analysis was carried out in the 2θ range of 2–70° using a PANalytical Empyrean diffractometer (PANalytical, Inc., Westborough, MA, USA) with Cu-Kα

radiation (1.5418 Å) at 40 kV and 45 mA. A mask of 20 mm and divergence slit of 1/32° were used on the incident beam path. A thin layer of the powdered nanoparticle was placed on a zero-background silicon plate and continuously spun at a rate of 22.5°/s. The solid state PIXcel3D detector (PANalytical, Inc.) was scanned at a rate of 0.053°/s. The PIXcel3D was equipped with a beam monochromator to improve the signal-to-noise ratio. Magnetic characterization was performed using a superconducting quantum interference device (SQUID) magnetometer (Quantum Design, MPMS-XL, Quantum Design International (QDI), San Diego, CA, USA) at 300 K. Stability of the EuCF-DTG nanoparticle suspension was assessed over three weeks by measuring hydrodynamic diameter and nanoparticle size distribution in saline on a Malvern Zetasizer Nano-Series instrument (Malvern Instruments Ltd., Malvern, UK) at 4 °C. FTIR were recorded on a Perkin-Elmer-spectrum attenuated total reflectance (ATR)-FTIR equipped with a UATR-accessary (Perkin-Elmer, Inc., Waltham, MA, USA). Atomic-force microscopy (AFM) was conducted using a Bruker Dimension Icon® Atomic Force Microscope (Bruker, Billerica, MA, USA) equipped with peak-force tapping and scan-assist with Al reflection coating (spring constant is 0.4 N/m and tip radius is ~2 nm, width 25 μm, thickness 0.65 μm, and length 115 μm). Multilayers of nanoparticles were prepared by drop-casting diluted aliquots of aqueous nanosuspensions on clean glass slides followed by slow evaporation of the solvent at room temperature. The images were flattened using Nano-Scope Analysis software (Bruker, Billerica, MA, USA). Nanoparticle morphology and structure were analyzed by transmission electron microscopy (TEM). Nanoparticle suspensions were dried on a copper grid at room temperature and bright field images were taken with exposure times of 2 s using the Tecnai G2 Spirit TWIN electron microscope (FEI, Houston, TX, USA) operating at 80 kV. Images were acquired with an AMT digital imaging system. Fluorescence spectroscopy was performed by SpectraMax® M3 Multi-Mode Microplate Reader (Molecular Devices, LLC, Sunnyvale, CA, USA).

2.2.5 In vitro drug release study

In vitro release study of DTG was performed using a USP dissolution testing system (Sotax-AT7smart USP, SOTAX Corp. Westborough, MA, USA) with dialysis bag technique [225] (Dialysis bag, MWCO 25 kD, Spectrum Laboratories, Inc., CA,USA). The DTG release experiments were carried out in Dulbecco's phosphate-buffered saline (DPBS; Thermo Fisher Scientific, Waltham, MA, USA) with 2% (v/v) Tween-80. Five mg of DTG in EuCF nanoparticles were placed in dialysis bags containing 3 mL of the release medium. The bags were placed in stainless steel baskets and immersed in a container containing 1000 mL of release medium at a temperature of 37±0.5 °C. One mL of each sample was withdrawn at regular time intervals and the same volume was replaced with fresh release medium. Samples were further diluted and analyzed for DTG content by HPLC. These studies were performed in triplicate for each sample, and the average values were used in the data analyses. Furthermore, the release profiles of DTG from nanoparticles were each fitted with Higuchi, Korsmeyer–Peppas, Elovich equation, parabolic diffusion, Bhaskar-equation, and Modified-Freundlich mathematical models [226].

2.2.6 Isolation of culture of monocyte-derived macrophages (MDM)

Human peripheral blood monocytes were obtained by leukapheresis from hepatitis B and HIV-1/2 seronegative donors, and purified by counter-current centrifugal elutriation [223]. Cells were cultured in Dulbecco's modified Eagle's medium (DMEM; Invitrogen, Grand Island, NY, USA) with 10% heat-inactivated pooled human serum (Innovative Biologics, Herndon, MA, USA), 1000 U/mL macrophage colony stimulating factor, 1% glutamine, 50 μg/mL gentamicin, and 10 μg/mL ciprofloxacin for 7 days to promote monocyte macrophage differentiation [227]. Cellular uptake of the EuCF-DTG and FA-EuCF-DTG nanoparticles was determined in MDM cultured in 12-well plates at a density of 1.5×10^6 cells/well. Cells were treated with nanoparticles in medium at a concentration of 5 μg iron/mL for 12 h. Nanoparticle uptake was assessed by measurement of cell drug and iron concentrations without medium changes. Adherent MDM were scraped into PBS at 2, 4, 8 and 12 h post treatment. Cells were pelleted by centrifugation at 1950 × g for 10 min at 4

°C and briefly sonicated in 100 μL of a mixture of methanol:acetonitrile (1:1 v/v) then centrifuged again at 10,844 × g for 10 min at 4 °C. Supernatant was used for DTG quantification by reversed phase HPLC. Parallel sets of cells were collected into nitric acid (69%) for ICP-MS analysis of iron and cobalt content.

2.2.7 Immunocytochemistry and transmission electron microscopy (TEM)

Macrophage nanoparticle uptake and subcellular distribution were studied by confocal microscopy and TEM [207, 223, 228]. To determine subcellular localization of EuCF-DTG nanoparticles, MDM were treated with nanoparticles at a concentration of 5 μg iron/mL for 8 h. For immunofluorescence staining, cells were washed three times with 1 mL of PBS (10 min each step) and fixed with ice cold 4% paraformaldehyde (PFA) at room temperature for 30 min. The cells were then washed with PBS (1 mL, 3X) for 10 min at each step and treated with a permeabilizing reagent (0.5% v/v Triton-X-100) for 15 min at room temperature. Cells were again washed with PBS (1 mL, 3X) for 10 min at each step. Cells were treated with a blocking solution (5% w/v BSA in PBS and 0.1% v/v Triton-X-100) for 1 h at room temperature and quenched with 50 mM NH4Cl for 15 min. The cells were washed once with 0.1% Triton-X-100 in PBS and incubated with primary antibody (Rab7 (SC-10767) for late endosomes, Rab11 (SC-6565) and Rab14 (SC-98610; Santa Cruz Biotechnology, Dallas, TX, USA) for recycling endosomes and LAMP-1 (NB120-19294; Novus Biologicals, Littleton, CO, USA) for lysosomes) diluted in blocking solution (5% BSA and 0.1% Triton-X in PBS; antibody: blocking solution 1:25) overnight with shaking at 4 °C. Cells were then incubated with secondary antibody (AlexaFluor-594; Thermo-Fischer Scientific, Waltham, MA, USA) and diluted in blocking solution (1:50) for 2 h at room temperature. Slides were covered with ProLong Gold AntiFade reagent with DAPI (4′,6-diamidino-2- phenylindole; Thermo-Fischer Scientific, Waltham, MA, USA) and imaged using a 63X oil objective on an LSM 710 confocal microscope (Carl Zeiss Microimaging, Inc., Dublin, CA, USA). Zeiss LSM 710 Image browser AIM software version 4.2 was used to determine the

number of pixels and the mean intensity of each channel. For TEM analysis, MDM (1.5 × 106 cells/mL) were incubated in 12-well plates for 8 h with nanoparticles (5 μg/mL of iron concentration). After treatment, cells were centrifuged at 1950 × g for 10 min at 4 °C. Cell pellets were suspended in a solution of 2% glutaraldehyde and 2% PFA in 0.1 M Sorenson's phosphate buffer (pH 6.2) for a minimum of 24 h at 4 °C. The cell fixation and block preparation methods are available in the Supplementary Material. MDM internal morphology was analyzed by cutting thin sections of control and nanoparticle-loaded MDM using a Leica UC6 ultramicrotome (Leica Microsystems, Inc., Buffalo Grove, IL, USA) then placed on 200 mesh copper grids. MDM and nanoparticle samples were examined using the Tecnai G2 Spirit TWIN electron microscope (FEI, Houston, TX, USA) operating at 80 kV. Images were acquired with an AMT digital imaging system.

2.2.8 Antiretroviral activity

Antiretroviral efficacies of the EuCF-DTG and FA-EuCF-DTG nanoparticles in HIV-1 -infected MDM were evaluated as described [196, 229]. In brief, MDM were treated with 6.25 μM, 12.5 μM, or 25 μM (DTG content) of native DTG, EuCF-DTG or FA-EuCF-DTG nanoparticles for 8 h. Cells were then cultured in fresh medium without nanoparticles. At days 1 and 5 post-treatment, MDM were then treated with HIV-1_{ADA} for 16 h at a multiplicity of infection (MOI) of 0.1 infectious virions per cell. Cells were maintained for 10 days post infection with a full media exchange occurring 2 days prior to analysis. The culture supernatants were assessed for progeny virion formation by measuring reverse transcriptase (RT) activity [230]. At this time, cells were washed with PBS and fixed in 4% PFA for 15 min. Fixed cells were blocked using 10% BSA containing 1% Triton-X 100

2.3 Results

2.3.1 Structural and physicochemical nanomaterial characterization

Theranostic multimodal EuCF-DTG lipid-PCL "core shell" nanoparticles were synthesized to have fluorescence, exhibit paramagnetism for MR imaging, and to package ARV therapy as lipid-PCL "core-shell" nano-constructs have previously been shown to be effective vehicles. Characterization of FA-decorated EuCF-DTG nanoparticles is outlined in Figure 2.1A Composition of the cores of the nanoparticles was PCL:DTG:EuCF (1:0.075:0.05 w/w/w) surrounded by a lipid shell of PC:DSPE-PEG:DOPE (1:0.5:0.5 w/w/w). For FA-EuCF-DTG nanoparticles, a lipid ratio of PC:DSPE-PEG_{2000}-FA:DOPE (1:0.5:0.5 w/w/w) was used. Synthesized theranostic nanoparticles exhibited fluorescence and emission wavelengths at 410 nm and 660 nm, respectively. Transmission electron microscopy (TEM) determined the internal morphology of the nanoparticles, with TEM images in Figure 2.1B showing nanoparticles possessing a spherical shape with a core structure composed of the PCL surrounded by multiple lipid surface layers. TEM images of nanoparticles without EuCF are shown in Figure 2.1B (i-ii). Complete embedding of the EuCF within the PCL core matrix is illustrated in Figure 2.1B (iii-iv). Characterization of the surface topography of nanoparticle was performed using atomic force microscopy (AFM) and suggested the lipid layers covered the spherical nanoparticles with smooth and uniform surfaces, as shown in Figure 2.1C. X-ray diffraction (XRD) patterns of EuCF and EuCF-DTG are shown in Figure 2.1D. Comparison of diffractograms of EuCF-DTG with that of native EuCF confirmed polycrystalline nature of the theranostic nanoparticles. Furthermore, XRD diffractogram patterns of the EuCF-DTG nanoparticles displayed peaks corresponding to organic and inorganic EuCF phases, showing incorporation of all necessary components into a finalized nanoparticle. Diffraction peaks exhibiting a decrement in EuCF intensity do so because of the masking effect of both PCL and lipids [231]. Broader diffraction peaks present in the EuCF-DTG XRD were attributed to the to the presence of nanosized EuCF crystals [231]. EuCF-PCL nanoparticles showed a saturation magnetization value of 7.5 emu/g and a sigmoid curve via superconducting quantum interference device (SQUID) analysis shown in Figure 2.1E, demonstrating that the nanoparticles were superparamagnetic at 300 K [223]. Dynamic light

scattering (DLS) was utilized to determine the hydrodynamic size of monodispersed nanoparticles, as shown in Figure 2.1F. Average nanoparticle size was 253 nm in diameter with a polydispersity index (PDI) of 0.14 and ~6.2% w/w DTG drug loading. Drug release from theranostic EuCF-DTG nanoparticles was found to cumulative with ~30% of drug released within 5 days and 36% by day 10 as shown in figure 2.1G. Additionally, it was found that when the cumulative percentages of DTG release from experimental formulations was plotted vs time that ~40% of DTG was released in 12 days from EuCF-DTG. Several kinetic models were used to better understand mechanism of DTG release from the EuCF-DTG nanoparticles: experimental *in vitro* release data set was fitted by the Higuchi, Korsmeyer-Peppas, parabolic diffusion, Elovich equation, Bhaskar equation, and a Modified-Freundlich kinetic model [225, 226]. Of the kinetic models tested, the parabolic diffusion and Bhaskar equations showed a theoretical DTG release pattern that was close to the experimental profile. Therefore, the kinetics of DTG release are governed by diffusion-controlled release phenomena.

Theranostic nanoparticles with a folic acid (FA) receptor targeting ligand were prepared by incorporating FA-PEG-DSPE onto the surface of EuCF-DTG nanoparticles. Specifically, chemical shifts at 3.3-3.6 ppm in the 1H-NMR spectrum correspond to repeating ethylene oxide (CH2CH2O) hydrogens of the PEG component of the lipid, while the aromatic protons from FA are at 7.7 and 8.3 ppm. Chemical shifts corresponding to DSPE are seen at 0.9 ppm (-CH3), 1.1 ppm (-CH2) and 2.1 ppm (-CH2CO) [40]. The EuCF nanoparticles contain characteristic absorption bands of octahedral metal-oxygen (M–O) bonds of the ferrite lattice [21]. DTG showed characteristic absorption bands at 1272 (-C-N), 1588 and 1650 (-C=O), 2983 (-C-H) and 3082 cm-1 (-C-H aromatic rings). The IR spectrum of PC demonstrates a characteristic C=O stretching band at 1740 cm−1 and PO−2 asymmetric double bond stretching bands at 1250 cm−1. The spectra of both PEG–DSPE and PC demonstrate a carbonyl ketone band at 1740 cm−1 and a CH alkyl-stretching band at 2891 cm−1. EuCF-DTG nanoparticles showed characteristic absorption bands

belonging to EuCF, DTG, PCL and lipids, along with bands at 2951 cm−1 (asymmetric), 2873 cm^{-1} (symmetric) due to (−CH2), and 1725 cm^{-1} for the carbonyl (−C=O) stretching of PCL [213]. The FTIR results indicate that DTG and EuCF interact strongly with PCL and lipids.

2.3.2 Macrophage uptake and subcellular distribution

Cellular uptake of theranostic nanoparticles was determined in MDMs. Cells were treated with FA-EuCF-DTG or EuCF-DTG nanoparticles (based on 5 µg/ mL iron) for up to12 hours, with cells washed in phosphate-buffered saline (PBS) and collected into nitric acid (69.0%) at either 2,4, 8, or 12 hours post-treatment. Cobalt and DTG concentrations were determined by ICP-MS and UPLC-MS/MS, respectively. As shown in Figure 2.2A, the uptake of FA-EuCF-DTG nanoparticles was significantly greater than that of EuCF-DTG nanoparticles at both 8 hours and 12 hours, as determined by iron content analysis. Cell iron concentrations exhibited a 4.5-fold greater amount of iron in cells treated with FA-EuCF-DTG nanoparticles are compared to EuCF-DTG nanoparticles at 12 hours post treatment. Cellular DTG levels show results corresponding to iron levels, with Figure 2.2B exhibiting FA-EuCF-DTG nanoparticles providing higher amounts of drug compared to EuCF-DTG nanoparticles. Visualization of cellular uptakes of nanoparticles and their subsequent subcellular distribution was performed using confocal microscopy and the inherent fluroscent properties of Eu^{3+} within nanoparticles (Figure 2.2C). Specifically, subcellular distribution of EuCF-DTG nanoparticles was determined by immunostaining with various different endosomal protein antibodies: Rab7 representing late endosomal sorting, Rab11 and Rab14 representing recycling endosomal compartments, and LAMP-1 representing the lysosomal-associated membrane protein-1. Primary antibodies were detected using a red Alex Fluor 594 secondary antibody. Figure 2.2D shows the yellow color associated with the colocalization of EuCF-DTG nanoparticles (green) and endosomal proteins (red) [196]. These resulting images suggest that EuCF-DTG nanoparticles were distributed mainly in recycling endosomal compartments throughout the cytoplasm (Rab11) and in the perinuclear region (Rab14).

Distribution within lysosomal regions (LAMP-1) and early endosomal compartments (Rab7) was less than that seen in recycling endosomes. Additionally, TEM was used to investigate the subcellular distribution of nanoparticles (Figure 2.2F-H) Typical macrophage morphology is illustrated by TEM of a control cell in Figure 2.2E, and visually there appears to be a greater amount of FA-EuCF-DTG nanoparticles that were internalized as compared to EuCF-DTG. Macrophage morphology was not altered by the presence of theranostic nanoparticles.

2.3.4 Antiretroviral activities of EuCF-DTG and FA-EuCF-DTG nanoparticles.

MDM infected with HIV-1_{ADA}, a prototype macrophage-tropic strain, were used to assess the antiretroviral activities of EuCF-DTG and FA-EuCF-DTG nanoparticles [196]. MDM were treated with nanoparticles are various DTG concentration while native drug served as a control. MDM were infected at a multiplicity of infection (MOI) of 0.1 infectious viral particles per cell after 1 day post-treatment. Progeny HIV-1 virion production was determined by reverse transcriptase (RT) activity in cell culture fluids 10 days after infection, with intracellular p24 antigen expression also being measured within cells. Figure 2.3A Illustrates that RT activity was suppressed by 6.25, 12.5, and 25 µM DTG (both native and nanoparticles), with parallel results being displayed in HIV-1 p24 staining (Figure 2.3B). Fewer HIV-1 p24 positive cells were detected with EuCF-DTG and FA-EuCF-DTG nanoparticles than in cell treated with native DTG at day 1 after treatment.

2.4 Discussion

The use of LASER ART as a viable alternative to conventional ARV therapy has been realized in our laboratories previous publications [195, 199, 202, 232, 233]. LASER ART can affect regimen changes, improve patient ARV adherence, reduce systemic toxicities, ease pill burdens and limit new viral infections [201, 233-235]. Nonetheless, hurdles remain in the conversion from commonly used pills into long-acting drug formulations. Our laboratories have taken a singular approach in converting hydrophilic or partially hydrophobic drugs into lipophilic prodrugs and in

using decorated polymers to target reservoirs of viral infection. This strategy seeks to optimize drug delivery, biodistribution and PK profiling [195-197, 199, 229]. However, the best strategy to screen newly synthesized and decorated nanoparticles remains unrealized. As therapeutic success of formulations is linked to nanoparticle size, shape, decoration, encapsulation and drug half-life, screening is cumbersome. Moreover, how best to assess drug penetrance into "putative" viral reservoirs remains a major obstacle in translational research efforts. We now posit that one means to assess the therapeutic potential of LASER ART is through theranostic probes [223]. Thus, stable ultra-sensitive EuCF nanoparticles encapsulating ARV and surrounded by lipids [213] were made. Such theranostic screens used to assess cell-based drug delivery holds potential for approaches to develop eradication strategies to cure HIV-1/AIDS.

EuCF-DTG nanoparticles were prepared via an emulsification solvent evaporation method using dichloromethane (DCM) as the organic phase. The mechanism of formation of multicomponent nanosystems is described as a combination of inorganic nanoparticles (EuCF) and organic, hydrophobic, biodegradable PCL forming the core of the particles with amphipathic lipids (DOPE, mPEG2000-DSPE and PC) constituting the shell of the multicomponent nanosystems. Importantly, PCL has a good solubility in DCM, which by diffusing towards the oil phases enhances the hydrophobic drug (DTG) retention in the core of EuCF-PCL, significantly improving encapsulation efficiency. Additionally, when the EuCF-PCL and drug solution (in DCM) is dispersed into the aqueous polyvinyl alcohol (PVA) surfactant, the agitation of the interface spontaneously produces a bigger interfacial area, which leads to nano-sized quasi-emulsion droplets of EuCF and DTG encapsulated in PCL. Simultaneously, combinations of amphipathic lipids serve as secondary surfactants on the surface of nanoparticles. Meanwhile, methanol specially diffuses from droplets due to its lower affinity for EuCF, DTG and PCL, and higher affinity for PVA. Continuous diffusion of methanol out of the droplets and the coacervation of PVA led to formation of nanoparticles with the lipids mixture acting as secondary surfactants.

Conclusively, the evaporation of residual solvent and subsequent solidification of EuCF-DTG core-shell nanoparticles, together with stirring in PVA solution, caused greater reduction in surface tension, leading to formation of the resultant particles in the nanometer range and with spherical morphologies.

DTG was released slowly over a time period of 12 days. The prolonged release profile could be attributed to physicochemical properties of the EuCF-DTG core-shell. Drug release occurred by diffusion through the lipid barriers followed by erosion of the core polymer by hydrolytic degradation. These hypotheses were cross validated by kinetic parabolic diffusion and Bhaskara equation models indicative of the low permeability of water in the particle's interior PCL core-shell. Due to the hydrophobic nature of DTG, it is probable that the drug was incorporated at the core of the particles during the solvent evaporation process. It is expected that nanoparticles prepared by solvent evaporation slowly release the drug due to the hydrophobic nature of the core materials.

Macrophage uptake and subcellular nanoparticle distribution enables drug delivery to HIV-1 infection sites [13, 236, 237]. Uptake of the lipid nanoparticles is greater than that of silica platforms [223]. The fluorescence modality of the EuCF-DTG and FA-EuCF-DTG nanoparticles proved useful in identifying nanoparticle subcellular distribution. We assayed macrophage nanoparticle uptake by measurements of both iron and DTG. We then examined nanoparticle subcellular localization using antibodies specific to subcellular compartment proteins and showed that the nanoparticles were distributed preferentially within recycling endosomes. Previously, we and others have demonstrated preferential localization of nanoformulated rod-shaped nanoparticles containing ARV drugs in similar compartments [196, 229]. HIV-1 persists in recycling endosomes [196, 202, 229] supporting the importance of subcellular ART depots.

Overall, EuCF-DTG “multimodal imaging theranostic nanoprobes” were made to facilitate the development of targeted LASER ART. The lipid-encapsulated EuCF nanoparticles can fulfill this role by providing a flexible platform for the design of diagnostic and therapeutic applications.

2.5 Figures

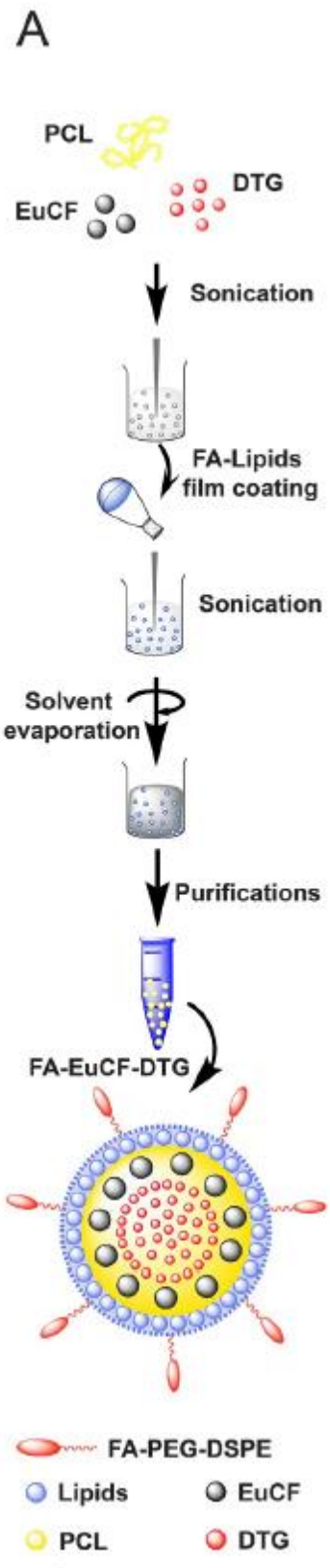
A
PCL
DTG
EuCF
Sonication
FA-Lipids
film coating
Sonication
Solvent
evaporation
Purifications
FA-EuCF-DTG
FA-PEG-DSPE
Lipids
EuCF
PCL
DTG

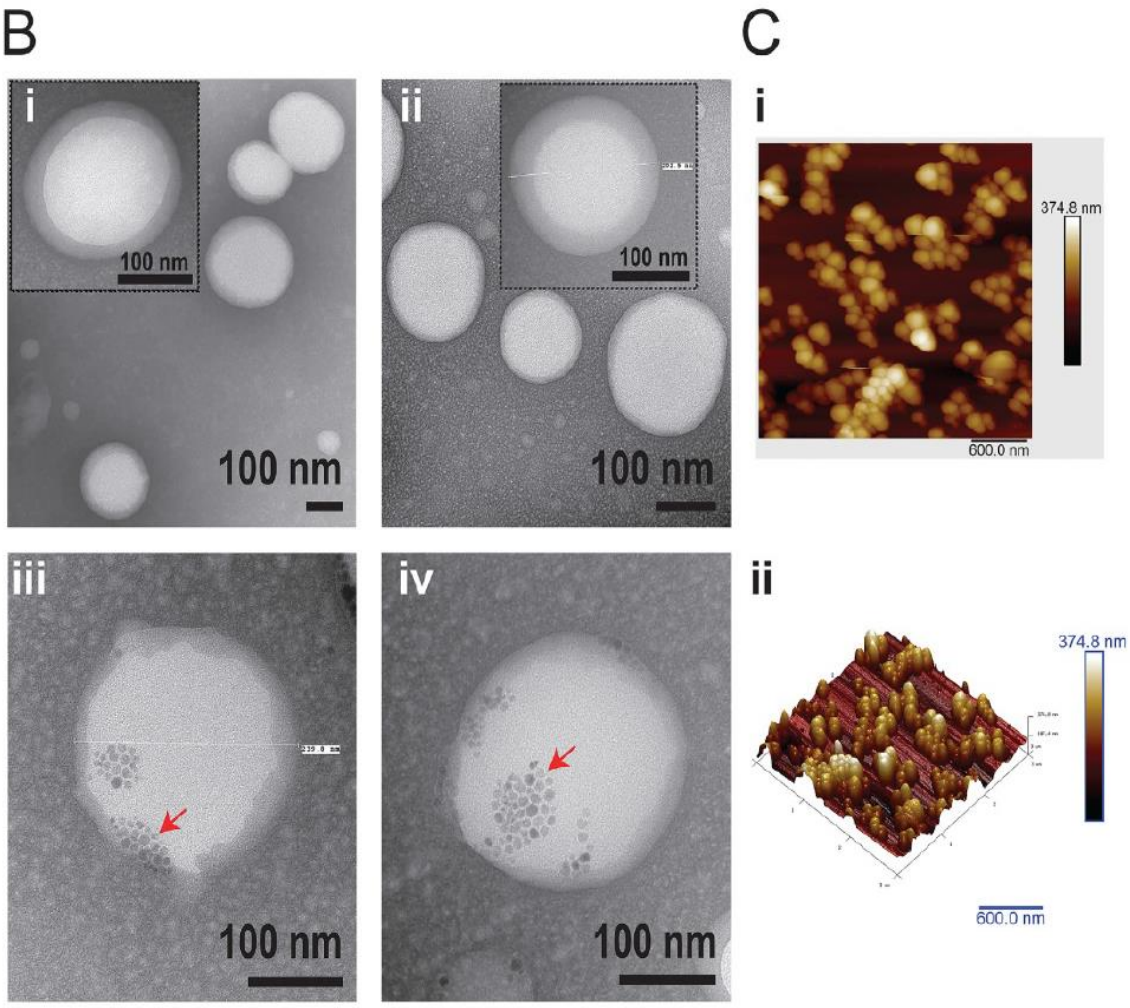
B
C
i
100 nm
100 nm
ii
100 nm
100 nm
iii
100 nm
100 nm
iv
100 nm
100 nm
i
374.8 nm
600.0 nm
ii
374.8 nm
600.0 nm

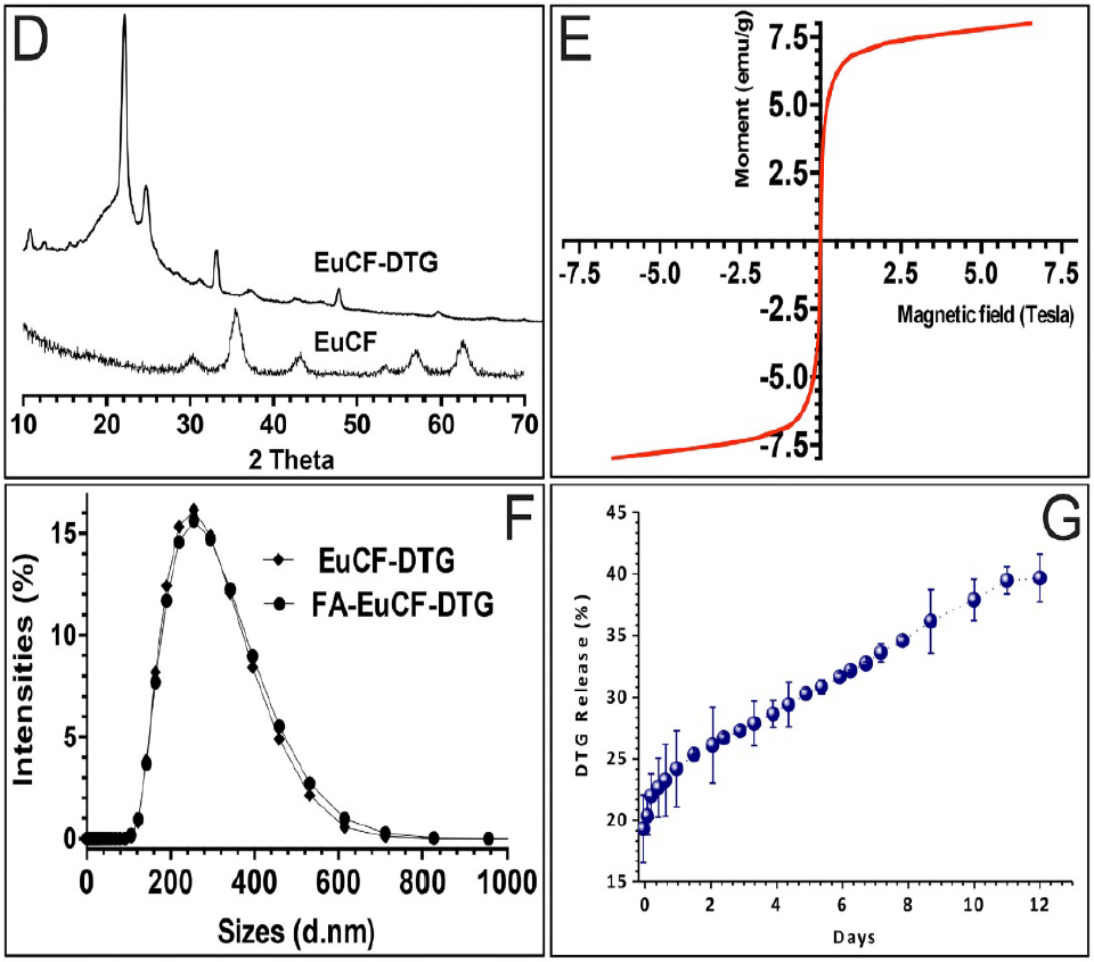
D
EuCF-DTG
EuCF
10
20
30
40
50
60
70
2 Theta
E
Moment (emu/g)
7.5
5.0
2.5
-2.5
-5.0
-7.5
-7.5
-5.0
-2.5
2.5
5.0
7.5
Magnetic field (Tesla)
F
Intensities (%)
15
10
5
0
EuCF-DTG
FA-EuCF-DTG
0
200
400
600
800
1000
Sizes (d.nm)
G
DTG Release (%)
45
40
35
30
25
20
15
0
2
4
6
8
10
12
Days

Figure 2.1 Synthesis and characterization of lipid-coated core-shell nanoparticles. (A) A schematic illustration of the design of multimodal FA-EuCF-DTG core-shell nanoparticles is presented. (B) TEM images of nanoparticles, (Bi) PCL-DTG (without EuCF) nanoparticles, (Bii) FA-functionalized PCL-DTG (without EuCF) nanoparticles, (Biii) EuCF-DTG nanoparticles, and (Biv) FA-EuCF-DTG nanoparticles. The lipid layers (average thickness of ~15 nm) appeared as a solid corona around the "hard" PCL matrix. EuCF nanocrystals (red arrows) appear as crystalline hexagonal-shaped monodispersed structures in the PCL matrix. (C) Characterization of the size distribution of EuCF-DTG nanoparticles by AFM. (Ci) AFM topographic distribution of EuCF-DTG nanoparticles and, (Cii) a corresponding 3D view. (D) X-ray powder diffraction (XRD) patterns of EuCF and EuCF-DTG nanoparticles. (E) Evaluation of the magnetic properties of the nanoparticles by magnetic-hysteresis (M-H) curves measurements using SQUID. Data are recorded at 300 K. (F) Hydrodynamic size distribution of nanoparticles determined by dynamic light scattering (average nanoparticle size of ~253 nm) and (G) *in vitro* release profiles of DTG in PBS (pH 7.3) at 37±0.5 °C

A

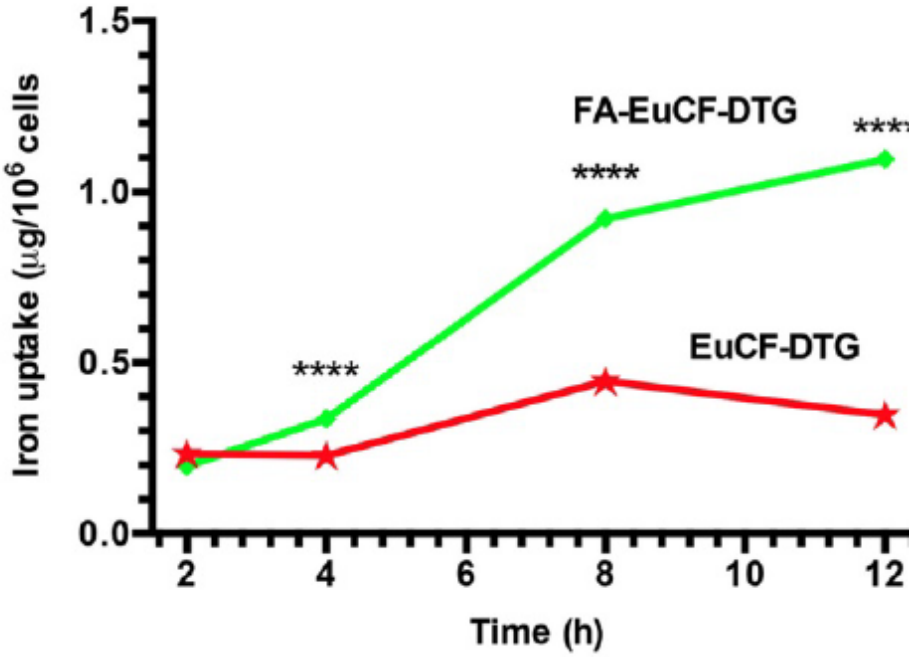
1.5
1.0
0.5
0.0
Iron uptake (μg/10^6 cells)
FA-EuCF-DTG
EuCF-DTG
****
****
****
2
4
6
8
10
12
Time (h)

B

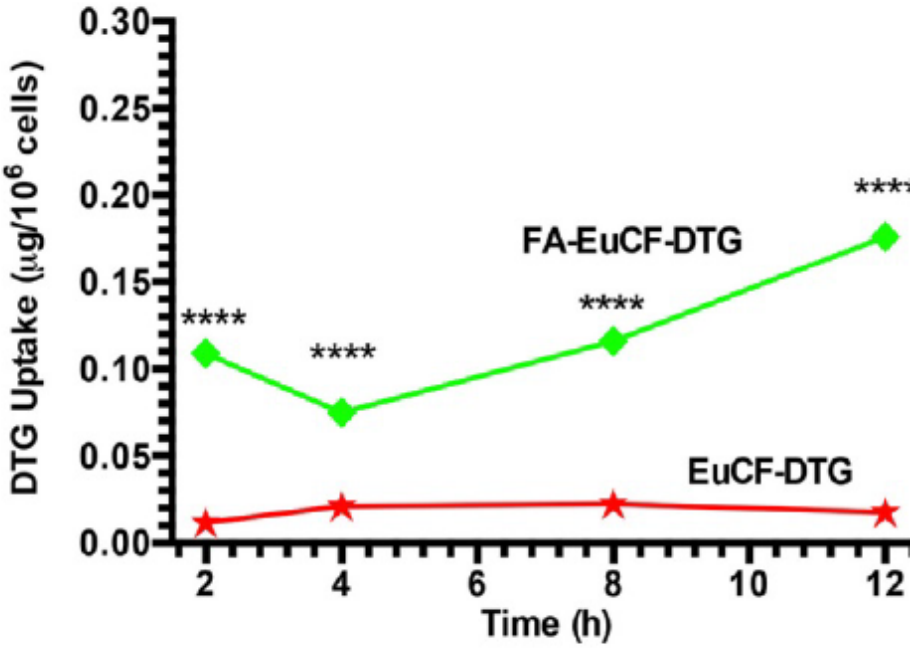
0.30
0.25
0.20
0.15
0.10
0.05
0.00
DTG Uptake (μg/10^6 cells)
FA-EuCF-DTG
EuCF-DTG
****
****
****
****
2
4
6
8
10
12
Time (h)

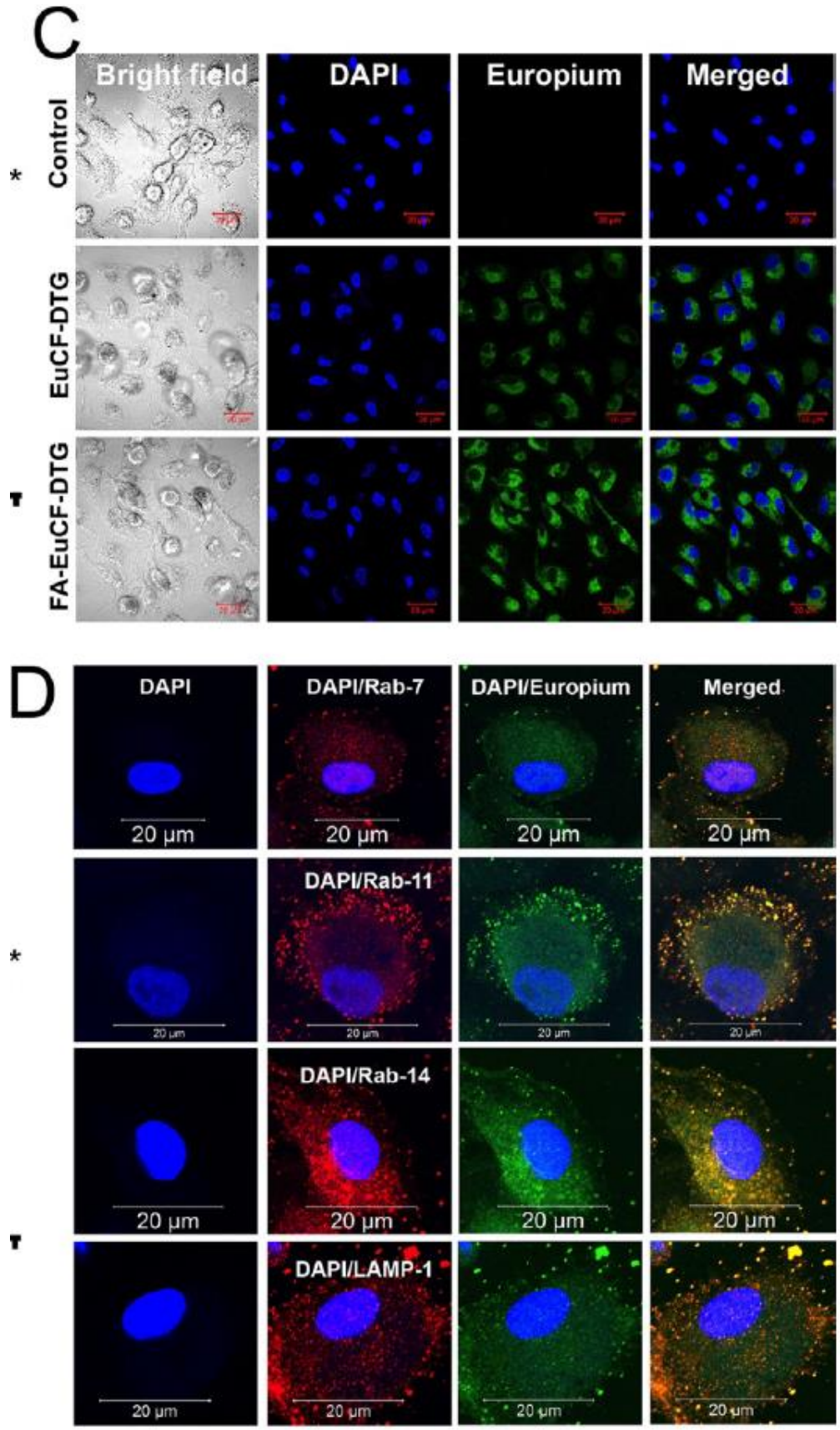
C
Bright field
DAPI
Europium
Merged
Control
EuCF-DTG
FA-EuCF-DTG
D
DAPI
DAPI/Rab-7
DAPI/Europium
Merged
DAPI/Rab-11
DAPI/Rab-14
DAPI/LAMP-1
20 µm

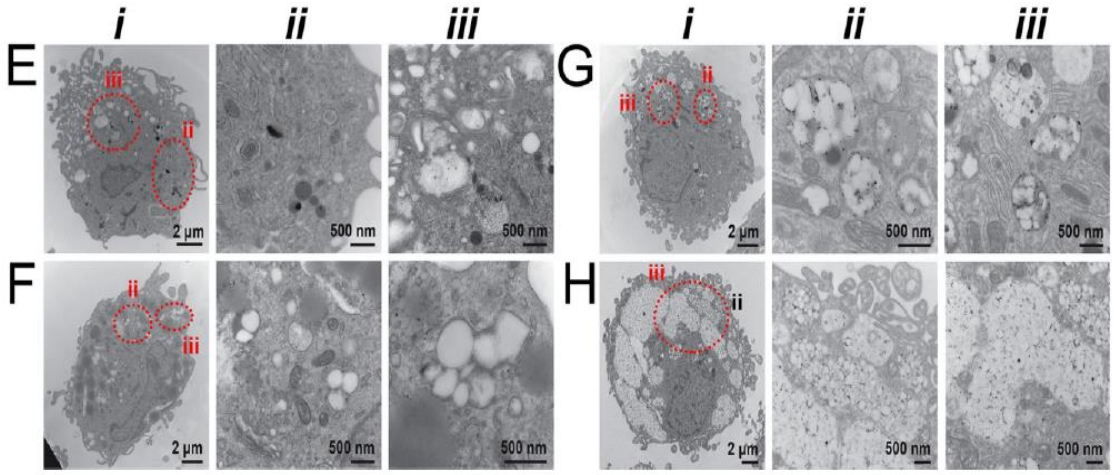

Figure 2.2 Macrophage nanoparticle uptake and subcellular distribution. Uptake and subcellular distribution of nanoparticles was determined in human MDM (monocyte-derived macrophage). EuCF-DTG and FA-EuCF-DTG nanoparticles were detected in cells at 2 h. EuCF-DTG and FA-EuCF-DTG nanoparticles were added to MDM culture at a concentration of 5 µg/mL iron. (A) Iron concentrations in MDM following nanoparticle uptake over 12 h and (B) corresponding DTG levels; data represent mean ± SEM (n = 3). Statistical differences were determined using one-way ANOVA among groups followed by Student's t-test for differences between groups at each time-point, ****$p < 0.0001$. (C) Intracellular nanoparticles were detected by confocal microscopy at an excitation wavelength of 488 nm and emission wavelength of 510/520 nm. (D) For subcellular distribution analysis, MDM were treated with EuCF-DTG nanoparticles (5 µg/mL based on iron; green) for 8 h and then immunostained with Rab7, Rab11, Rab14 and LAMP-1 antibodies and Alexa Fluor 594-labeled secondary antibody (red) to visualize nanoparticle and organelle co-registration. The yellow (merged) shows overlap of nanoparticles and Rab compartments. DAPI (blue) stain indicates cell nuclei. Images were captured with 63X objective on a Zeiss LSM 710 confocal microscope. Scale bars = 20 µm. (E-H) TEM ultrastructural evaluation of macrophage nanoparticle uptake and subcellular distribution. Nanoparticles were added to MDM cultures for 8 h. Cells were fixed and processed for TEM. (E) Typical internal morphology of control macrophages is shown. Detailed evaluation of membrane-bound intracellular structures at areas of interest is presented in magnified panel ii and iii. (F–H) Intracellular uptake of (F) PCL-DTG (without EuCF), (G) EuCF-DTG and (H) FA-EuCF-DTG nanoparticles. Areas of interest bordered with dotted red lines are presented in corresponding high-resolution images (ii–iii) and illustrate nanoparticles within membrane-bound intracellular structures. All nanoparticle types were internalized and entrapped in endosomal vesicles in the macrophages. Images of macrophages treated with FA-functionalized nanoparticles reveal a higher number of nanoparticles internalized in vesicles compared to non-decorated particles. EuCF-DTG and FA-EuCF-DTG nanoparticles are seen as black punctate structures encapsulated in white polymeric nanoparticles within membrane-bound endosomes

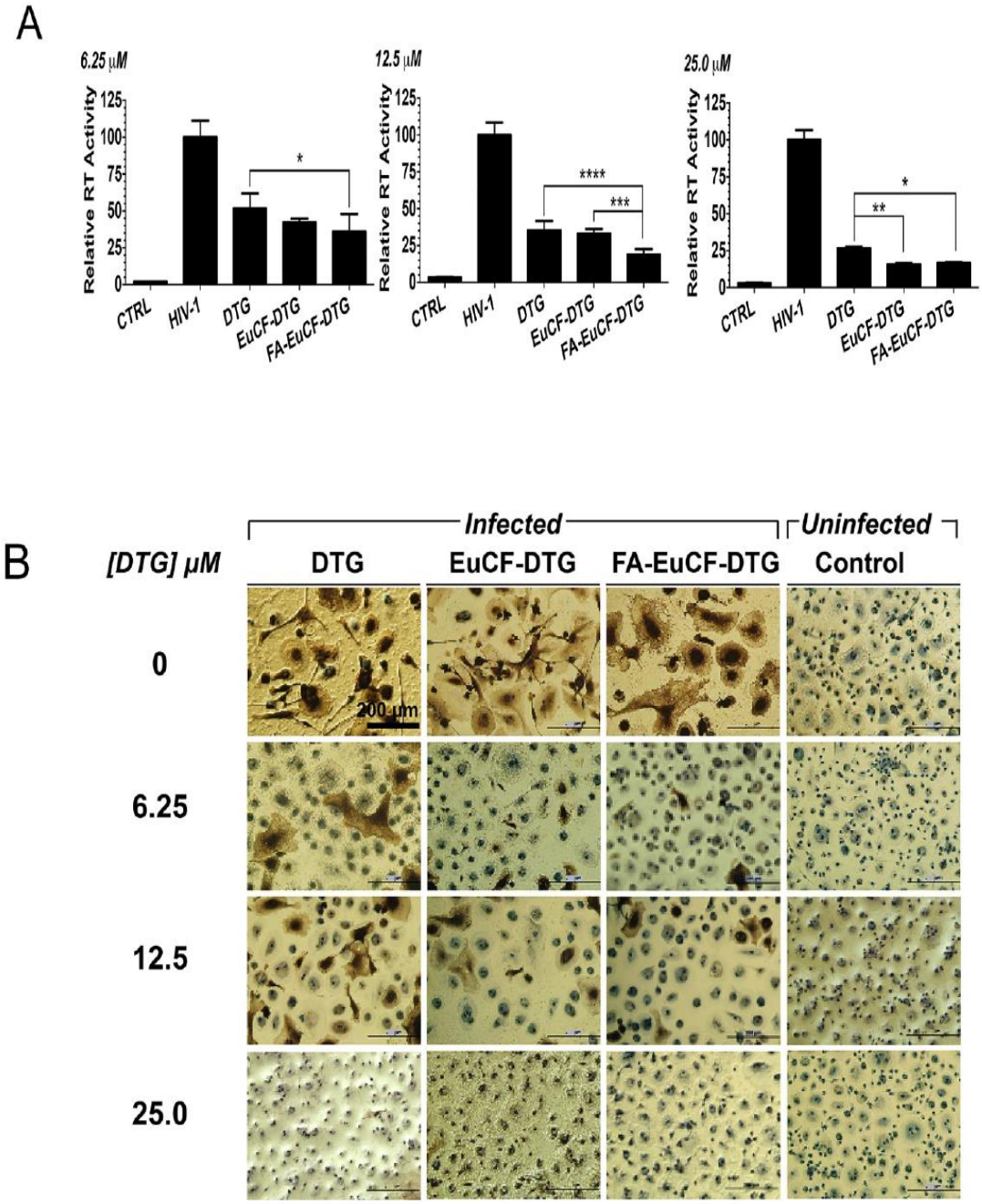

Figure 2.3 Antiretroviral activity measurements. Antiretroviral activity was determined in MDM treated for 8 h with free DTG, EuCF-PCL, EuCF-DTG or FA-EuCF-DTG nanoparticles (6.25, 12.5 and 25 μM DTG) and then infected with HIV-1_{ADA} at a multiplicity of infection (MOI) of 0.1 at day 1 after drug loading. At 10 days after infection, progeny HIV virion production was determined by RT activity in the cell culture fluids. (A) HIV replication was determined 10 days after infection by HIV RT activity of day 1. Statistical differences were determined using one-way ANOVA among groups; we used Tukey's test to correct for multiple comparisons. *$p < 0.05$; **$p < 0.01$; ***$p < 0.001$. (B) HIV p24 staining (scale bar = 200 μm).

CHAPTER 3

In vivo and *ex vivo* biodistribution studies of multi-modal theranostic nanoformulations in rats and rhesus macaques

3.1 Introduction

To realize the potential of long acting viral reservoir penetrating drugs, pharmacokinetic and pharmacodynamic profile assessment must be performed to minimize on and off-target effects. Current PK and PD experimental assessments often take weeks to months to perform, and with multiple innovative strategies coming to the forefront of development, such timeframes have proved too tedious and time consuming. To overcome these technical and biologic challenges, multimodal decorated nanoparticles were produced where hydrophobic ARVs and bioimaging agents were encased in a single nanoformulation. All were placed into one "multimodal imaging theranostic nanoparticle" using core-shell construction methods [213]. This allowed real-time assessment of ARV biodistribution and activity [223]. *S*ynthesized nanoparticles were deployed for sensitive MRI tests. Such testing facilitated PK analyses and monitoring of drug-loaded nanoparticle distribution into tissue reservoirs of viral infection. The core-shell structure was engineered to carry ARVs that include DTG (EuCF-DTG), while demonstrating excellent relaxivity profiles of r2 = 564 mM^{-1} s^{-1} and r2 = 546 mM^{-1} s^{-1} (targeted nanoparticles) in saline and r2 = 876 mM^{-1} s^{-1} and r2 = 850 mM^{-1} s^{-1} (targeted nanoparticles) in cells. The Eu3+ component enabled fluorescence imaging for histological validation of cell localizations of drug-loaded nanoparticles [223]. DTG release from EuCF-DTG nanoparticles provided real-time validation of drug biodistribution, as EuCF-DTG nanoparticles are rapidly endocytosed and retain potent antiretroviral activity. Confocal microscopy with Eu3+ fluorescence showed nanoparticles in cytoplasmic Rab compartments that affect vesicle trafficking and ARV depot formation [195, 202, 238, 239]. Following synthesis and particle characterization, bioimaging tests reflected drug biodistribution after parenteral injection in rats and rhesus macaques. No secondary metabolic or histopathological alterations were observed.

3.2 Materials and methods

3.2.1 MRI relaxometry measurements

EuCF-DTG and FA-EuCF-DTG nanoparticle suspensions with an iron concentration ranging from 0.2 to 2 μg/mL were prepared in DPBS. A 1.5% w/v agar gel was prepared by adding 150 mg of low melting agar in 10 mL of PBS at 70°C for 30 min. Phantom gels containing nanoparticles were prepared by mixing 100 μL of a 1.5% (w/v) agar solution that was preheated to 60°C to prevent gelation with 100 μL of the nanoparticle suspension. Experiments were performed in triplicate at each concentration. In order to make sure that no air bubbles were present, the nanoparticle suspensions and agar gels were vortexed thoroughly while warm in 250 μL eppendorf tubes and then rapidly cooled in an ice bath. MRI tests were performed using eppendorf tubes containing the fixed nanoparticles in agar gels. MRI data were acquired on a 7T/16 cm Bruker PharmaScan MRI system (Bruker; Ettlingen, Germany). T2-relaxtion maps were generated using a CPMG (Carr Purcell Meiboom Gill sequence) phase-cycled multi-echo sequence. Single slice (0.5 mm slice thickness) data were acquired with 3000 ms repetition time, 50 echoes (echo times TEn = n x 10 ms; n = 1), 256 x 128 acquisition matrix, 50 x 50 mm field of view (FOV), 2 averages, for a total scan time of 13 min. For T2 relaxation time measurements in MDM, as described in our previous study [223], monocytes were seeded onto 100 mm culture plates at a concentration of 10^6 cells/mL and differentiated into macrophages in the presence of MCSF for seven days. Following this, MDM were treated with nanoparticles (5 μg iron/mL) for 8 h and then the treatment medium was removed and cells washed three times with DPBS. Cells were scraped into DPBS, collected by centrifugation (1950 × g for 10 min at 4 °C) and suspended at various cell concentrations containing 1.5% w/v agar in 250 μL eppendorf tubes. For T2 map measurements, CPMG phase-cycled 3-dimensional multi-echo sequence data was acquired with 250 ms repetition time, 48 echoes (echo times TE_n = n X 2.618; n = 1,…,48), 128 × 128 × 64 acquisition matrix, 70 × 64.76 × 42.38 mm FOV, one average, for a total scan time of 34 min.

3.2.2 EuCF-DTG and FA-EuCF-DTG nanoparticle biodistribution in rats

In vivo biodistribution of nanoparticles was determined in male Sprague Dawley rats (160–170 g) obtained from Charles River Laboratories (Wilmington, MA, USA). Animals were housed in the University of Nebraska Medical Center (UNMC) laboratory animal facility according to Association for Assessment and Accreditation of Laboratory Animal Care guidance. All protocols related to animal experiments were approved by the UNMC Institutional Animal Care and Use Committee, and met the requirements of the UNMC ethical guidelines set forth by the National Institutes of Health. Rats were divided into multiple groups dependent on their route of injection and planned sacrifice time point of 2, 5, or 10 days post-injection. 24 hours prior to nanoparticle treatment, rats were given 5 mg/kg lipopolysaccharide (LPS) by intraperitoneal injection to engage the innate immune system and affect macrophage activation in analogous manners as would be seen following HIV-1 infection. Rats were MRI scanned prior to injection of the EuCF-DTG nanoparticles (2 mg iron/kg iron content) and at 2, 5 and 10 days post-injection to determine nanoparticle biodistribution and integrity. Assessment of the effects of FA targeting was performed by administration of FA-EuCF-DTG nanoparticles in rats by either IM or IV injection. MRI scanning was performed pre-injection and 5 days after injection for comparison tests of EuCF-DTG administered animals. MRI was performed using the same 7T/16 cm Bruker PharmaScan that was used for phantom data acquisition. Both T2 ∗-weighted high-resolution imaging and T2 mapping were used to determine the biodistribution of EuCF-DTG nanoparticles. T2 ∗-weighted MRI was performed using a 3D spoiled gradient recalled echo sequence with 10 ms repetition time, 2.7 ms echo time, 15° pulse angle, 256 × 196 × 128 acquisition matrix, 75 × 57.5 × 37.5 mm FOV, six averages, for a total scan time of 25 min. For T2 mapping, CPMG phase-cycled 3-dimensional multi-echo sequence data were acquired with 24 echoes (echo times TEn = n × 2.718 ms; n = 1, 2, …,24), 400 ms repetition time, 128 × 128 × 64 acquisition matrix, 70 × 64.76 × 42.38 mm FOV, one average, for a total acquisition time of 34 min. T2 relaxation times were computed at each pixel and generated maps using custom computer programs written in Interactive Data Language (IDL; Exelis Visual Information Solutions; McLean, VA, USA). These maps were constructed at pre-

injection and 24 h post-injection of nanoparticles using the even-echo images from the CPMG phase cycled imaging data. Estimation of T2 relaxation times from even echoes only minimizes the measurement errors due to the imperfection of high-power pulses [240]. The region of interest (ROI) analysis was performed using Image-J software (http://imagej.nih.gov/lj). The concentrations of nanoparticles were determined from the change in relaxivity rate ($\Delta R2 = 1/T2_{postinjection} - 1/T2_{preinjection}$) and the nanoparticle relaxivity (r2) per mmol was determined as the slope of iron concentration versus R2 measured ex vivo

3.2.3 Plasma and tissue drug, iron, and cobalt animal tissue quantifications

Drug concentrations in animal plasma and tissues were determined by UPLC-tandem mass spectrometry (UPLC-MS/MS) using a Waters Acquity H-class UPLC- Xevo TQ-S micro system (Waters Corp, Milford, MA, USA). For plasma drug quantitation, 25 µL of sample was added into 1 mL acetonitrile, followed by addition of 10 µL of internal standard (IS) solution to achieve a final IS concentration of 50 ng/mL DTG-d3 (Clearsynth Canada Inc, Mississauga, ON, Canada) after reconstitution. Samples were then vortexed and centrifuged at 17,000 g for 10 min at 4°C. Supernatants were dried using a Thermo Scientific Savant Speed Vacuum (Waltham, MA) and reconstituted in 100 µL 50% (v/v) acetonitrile in MS-grade water. Standard curves were prepared in blank rat plasma in the range of 0.2–00 ng/mL. For tissue analyses, 100 mg of tissue was homogenized in 4 volumes of 90% (v/v) acetonitrile in MS-grade water using a Qiagen Tissue Lyzer II (Valencia, CA, USA). To 100 µL of tissue homogenate 80 µL of acetonitrile, 10 µL of 50% acetonitrile (v/v) was added in MS-grade water, and 10 µL IS. Standard curve samples were prepared using equivalent tissue matrix dilutions, 80 µL of acetonitrile, 10 µL of 50% acetonitrile (v/v) in MS-grade water spiked with standard drug concentrations, and 10 µL of IS. Chromatographic separation of 10 µL of plasma or tissue samples was achieved with an Acquity UPLC-BEH Shield RP18 column (1.7 µm, 2.1 mm x 100 mm) using a 10-min gradient of mobile phase A (7.5 mM ammonium formate in Optima-grade water adjusted to pH 3 using formic acid)

and mobile phase B (100% Optima-grade acetonitrile) at a flow rate of 0.25 mL/min. The initial mobile phase composition of 40% B was held for the first 3 min, increased to 86% B over 0.5 min further, held constant for 5 min, then reset to 40% B over 0.25 min and held constant for 1.25 min. DTG was detected at a cone voltage of 10 volts and collision energy of 25 volts. Multiple reaction monitoring (MRM) transitions used for DTG and DTG-d3 were 420.075 > 277.124 and 422.841 > 129.999 m/z, respectively. Spectra were analyzed and quantified by Mass Lynx software version 4.1. DTG quantitations were based upon drug peak area to internal standard peak area ratios. Iron and cobalt levels were quantified by inductively coupled plasma mass spectrometry (ICP-MS) on an Agilent Technologies ICP-MS 7500cs (Santa Clara, CA) and an ESI SC-4 high-throughput autosampler (Elemental Scientific Inc., Omaha, NE) [241]

3.2.4 SIV-infected rhesus macaques

Three female rhesus monkeys were obtained from the Yerkes National Primate Research Center. The monkeys were infected with SIVmav239 by an intravenous injection route 350 days prior to drug administration. The monkeys had also been infected with Zika virus subcutaneously 175 days prior to this study. All animals had cleared Zika virus but were productively chronically infected with SIV. EuCF-DTG nanoparticles were prepared under GLP conditions as above and given to animals by intramuscular injection at a dose of 2 mg/kg based on iron on day 0. Animal health was monitored daily and injection sites were examined closely under anesthesia on days 3 and 7; no reaction was noted. Blood was collected in K-EDTA tubes and plasma prepared on day -5, day 0, day 3 and day 7; CSF was collected without additives in tubes on day 0 and day 7. On day -2 pre- and day 5 post- EuCF-DTG nanoparticle administration, MRI was performed on the three animals.

3.2.5 MRI tests for EuCF-DTG nanoparticle biodistribution in rhesus macaques

Biodistribution of EuCF-DTG nanoparticles in rhesus macaques was determined using a Philips Achieva (Briarcliff Manor, NY, USA) 3.0T MRI scanner. T2-weighted high-resolution imaging and T2 mappings were obtained. High resolution T2-weighted images were acquired using a turbo spin echo (TSE) sequence with 1428.6 ms repetition time, 90 ms echo time, 90° flip angle, 116 echo train length, 22 slices (3.5 mm slice thickness; 4.5 mm spacing between slices), 360 × 360 acquisition matrix, 360 × 360 mm FOV, 6 averages, for a total scan time of 31.42 min. A multi-echo TSE sequence was used for T2 relaxation time mapping. Images were acquired with 2000 ms repetition time, 16 echoes (echo times TEn = n x 6 ms; n = 1, …,16), 288 x 288 acquisition matrix, 360 × 360 mm FOV. This sequence was repeated to cover multiple coronal slices (12 slices for pre-injection and 16 slices for post-injection, 3.5 mm slice thickness, 4.5 mm spacing between slices). T2 relaxation time maps were created using custom-developed computer programs using IDL programming language. ROI analysis was performed using ImageJ software.

3.2.6 Tissue analyzes from treated rhesus macaques

After imaging on day 5, bone marrow and lymph node biopsies were performed on two of the animals. The third animal was sacrificed on day 7, and fluids and tissues were collected for study. At necropsy, splenomegaly and lymphadenopathy were present (consistent with chronic SIV infection), and EuCF-DTG nanoparticles were present in the gall bladder, confirmed by ICP-MS (cobalt = 0.476±0.037 μg/g). Complete blood counts and metabolic panels were performed by the UNMC Department of Pathology and Microbiology / Nebraska Medicine Clinical Laboratory Services. All animal experimentation was performed under approval by the UNMC IACUC in AAALAC-certified facilities following NIH guidelines

3.2.7 Immunohistochemistry of rat tissues

To determine cellular distribution of EuCF-DTG nanoparticles in tissues, following the MRI scan (five days after administration of EuCF-DTG nanoparticles) animals were euthanized for

collection of tissues. Tissues were fixed in 4% PFA overnight and embedded in paraffin. Tissue sections (5 µm) were cut and mounted on glass slides. For rats, tissues sections were probed with rabbit anti-rat polyclonal antibody to ionized calcium binding adaptor molecule-1 (Iba-1) (1:500; Wako Chemicals, Richmond, VA, USA) to detect macrophages. Primary antibody was detected with anti-rabbit secondary antibody conjugated to Alexa Fluor 594 (Thermo-Fischer Scientific, Waltham, MA, USA).

3.2.8 Immunohistochemistry of rhesus macaque tissues

Tissues (spleen and lymph nodes) were perfused with phosphate buffer saline (PBS) followed by post-fixation with 4% paraformaldehyde (PFA) for 3 days at room temperature then processed in a automated processor in Shandon Citadel-1000 processor (Thermo scientific) for 18 h with reagents in step-wise manner containing 70, 95 and 100% flex followed by Xylene and paraffin. Finally tissues were embedded using paraffin blocks for further sectioning. Sections 5µ-thick were cut from the paraffin blocks, mounted on glass slides and labelled with combination of rabbit monoclonal antibody to CD68 (Sigma-Aldrich, St. Louis, MO, USA) for macrophages and mouse monoclonal antibodies to SIV-p27. Primary antibodies were labeled with secondary anti-mouse and anti-rabbit antibodies conjugated to the fluorescent probes Alexa Fluor® 633 and Alexa Fluor®594 and nuclei were labeled with 4′,6-diamidino-2-phenylindole (DAPI). Slides were cover slipped with ProLong Gold anti-fade reagent (Invitrogen, Carlsbad, CA), allowed to dry for 24 h at room temperature and then stored at −20 °C for future use. Images were captured at wavelengths encompassing the emission spectra of probes, with a 40X magnification objective. Images were captured using a Zeiss LSM710 confocal microscope and analyzed with Zen 2011 software (Carl Zeiss Micro imaging)

3.2.9 Toxicological assessments

In vivo toxicity of the EuCF-DTG nanoparticles was determined by serum chemistry and histological examination. For histological examination, 5 μm sections of paraffin-embedded tissues were affixed to glass slides and stained with hematoxylin and eosin. Images were captured with a 20X objective using a Nuance EX multispectral imaging system affixed to a Nikon Eclipse E800 microscope (Nikon Instruments, Melville, NY, USA). Histopathological assessment was conducted in accordance with the guidelines of the Society of Toxicologic Pathology. For serum chemistry analysis, rat blood samples were collected before and five days after EuCF-DTG nanoparticles administration. Albumin (ALB), alanine aminotransferase (ALT), total bilirubin (TBIL), phosphate (PHOS), total protein (TP) and amylase (AMY) were quantitated using a VetScan comprehensive diagnostic profile disc and a VetScan VS-2 instrument (Abaxis Veterinary Diagnostics, Union City, CA, USA).

3.3 Results

3.3.1 MRI assessment of EuCF-DTG and FA-EuCF-DTG nanoparticles biodistribution

Theranostic nanoparticle relaxation rates (R_2) were measured in both PBS and MDM and were found to increase linearly with increasing iron concentrations, demonstrating paramagnetism (Figure 3.1C). The linear regression coefficients of determination (r2) for relaxation rate (R2) vs. iron content for EuCF-DTG and FA-EuCF-DTG nanoparticles were 0.979 and 0.973 in PBS, respectively (Figure 3.1C left), and 0.985 for both EuCF-DTG and FA-EuCF-DTG nanoparticles in cells (Figure 3.1C right). The relaxivities of the EuCF-DTG and FA-EuCF-DTG nanoparticles were r2 = 564 mM^{-1} s^{-1} and r2 = 546 mM^{-1} s^{-1} in PBS, and r2 = 876 mM^{-1} s^{-1} and r2 = 850 mM^{-1} s^{-1} in cells, respectively. In comparison with superparamagnetic iron oxide (SPIO) nanoparticles, FA-EuCF-DTG nanoparticles showed a log-order of magnitude increase in both sensitivity and specificity at replicate iron concentrations [223]. T_2^*-weighted images of FA-EuCF-DTG nanoparticles in increasing iron concentrations within PBS phantoms exhibited decreasing signal

intensities, again showing the paramagnetic properties of the synthesized nanoparticles (Figure 3.1D). Together, these data confirmed magnetic sensitivity.

In vivo assessment of EuCF-DTG and FA-EuCF-DTG nanoparticle biodistribution was performed in Sprague Dawley rats following either intravenous (IV) or intramuscular (IM) injection (Figure 3.3A). The experimental timeline for the EuCF-DTG nanoparticle injection and MRI scanning is shown in Figure 3.2A. MR images representative of pre-injection and 2,5, and 10 days post-injection time points are shown in Figure 3.2B A reduction in T_2^*-weighted signal intensity in the MRI images can be seen within animals liver (red highlight) and spleen (green highlight) at all post-injection time points, reflecting the presence of iron due to nanoparticle distribution to these tissues.

In vivo assessment of EuCf-DTG nanoparticle biodistribution was also performed in rhesus macaques infected with simian immunodeficiency virus (SIV). Administration of theranostic nanoparticles to these animals was proof-of-concept to determine subsequent biodistribution in a large animal during viral infection, such an animal model is much more comparable to humans infected with HIV-1. Plasma viral loads ranged from 10^6-10^7 copies/mL in the tested animals. Figure 3.3C shows a schematic of the uptake of EuCF-DTG nanoparticles by macrophages and the establishment of a reticuloendothelial system drug depot. MR images of rhesus macaques before nanoparticle injection and 5 days post-injection revealed a significant decrease in T_2-weighted signal within the liver and the spleen after 5 days (Figure 3.3D). This change in T_2 signal intensity proved to be higher within the liver as compared to the spleen, indicating a possible increase in uptake of EuCF-DTG nanoparticles within hepatic tissue. Such shortening of T_2 in the rhesus macaque MR images are comparable to MR images taken of EuCF-DTG at identical timepoints, suggesting that EuCF-DTG biodistribution is similar between the species.

3.3.2 DTG, iron and cobalt validation tests in both rats in rhesus macaques

The concentrations of the various components of EuCF-DTG nanoparticles within administered animals was determined by multiple independent techniques: iron concentration was estimated *in vivo* by MRI, DTG drug concentration was determined *ex vivo* by ultraperformance liquid chromatography tandem mass spectrometry (UPLC-MS/MS), and cobalt concentration was determined *ex vivo* by inductively coupled plasma mass spectrometry (ICP-MS) (Figure 3.6A-C). Quantification of iron concentrations within the liver and spleen of both rats and rhesus macaques was performed by MRI T_2 mapping, and subsequently compared with respect to time and route of administration (Figure 3.5A). Iron concentrations were two-fold higher in animals given IV injections compared to animals given IM injections (Figure 3.5A) IV injected animals displayed decreasing iron levels in the liver and spleen over time, while corresponding iron levels in IM-injected animals were lower but sustained over the 10-day experimental time course. Comparison of tissue iron and cobalt levels exhibited a similar trend of DTG drug levels (Figure 3.5A-B). Figure 3.5C shows liver and spleen DTG concentrations at days 2 and 5. Figure 3.6 D-E illustrates cobalt and DTG plasma concentrations. Drug levels in liver and spleen were approximately 2-fold higher at day 2 post-treatment compared to day 5 post-treatment. The DTG levels in liver at day 2 and day 5 were 112±42 ng/g (IV) and 91.2±32 (IM) ng/g versus 47.3±44 ng/g (IV) and 27.12±15 ng/g (IM), respectively; whereas, DTG levels in the spleen at day 2 and day 5 were 39.3±21 ng/g (IV) and 82.4±41 ng/g (IM) versus 54.8±23.3 ng/g (IV) and 15.12±5.4 ng/g (IM), respectively. In general, both IV or IM administration of nanoparticles showed coordinate tissue and plasma drug and cobalt levels. Liver macrophage uptake of nanoparticles was 2.5-fold higher than splenic uptake of nanoparticles (Figure 3.5A-C). A correlation analysis of iron levels obtained by MRI, cobalt levels by ICP-MS, and DTG drug levels by UPLC-MS/MS was performed in both the liver and spleen in IV and IM injected animals to validate the usefulness of MRI to track nanoparticles in real-time. Figure 3.5F shows Pearson correlation plots between *in vivo* MRI iron levels and both tissue DTG and cobalt concentrations. Day 5 iron levels measured by MRI are plotted versus cobalt levels for individual animals given IM or IV injections are shown in Figure 3.5D. Such plots show

a strong correlation between iron, cobalt, and DTG concentrations within the liver and spleen, with Pearson's correlation coefficients of r = 0.8949 within the liver, r = 0.9396 within the spleen, r = 0.6505 within both liver and spleen for iron versus cobalt, and r = 0.789 within both liver and spleen for iron versus drug. DTG and iron levels within the liver and spleen were directly related to cobalt concentrations as measured by ICP-MS (Figure 3.5D). Such data suggests that MRI can be used to estimate the amount of drug that accumulates within reticuloendothelial tissues by using the known *in vivo* MRI signal-to-drug ratio for EuCF-DTG nanoparticles (Figure 3.7)

Investigation of the biodistribution of EuCF-DTG nanoparticles by MRI in rhesus macaques was performed to confirm whether the data sets observed in the *in vivo* rat biodistribution studies could possibly be observed in a species that is much more closely related to humans. Plasma and tissue DTG and cobalt concentrations were also measured *ex vivo.* The liver and kidneys of the rhesus macaques displayed the highest concentrations of cobalt and DTG, with detectable levels also being observed in the spleen and lymph nodes (Figure 3.8) Very small amounts of drug or cobalt was detected within the lungs. Such data suggests that macrophages within reticuloendothelial tissues of macrophages take up EuCF-DTG nanoparticles.

3.3.3 Intracellular macrophage nanoparticle trafficking in rat tissues

Immunohistology and TEM was performed *ex vivo* on rat tissues to confirm the localization of nanoparticles within the liver and splenic macrophages. Figure 3.9A shows tissue sections of liver and spleen from animals sacrificed 5 days post-EuCF-DTG injection (IM and IV). Tissues were probed with Iba-1 antibody to identify activated macrophages. The yellow/orange color highlighted by arrows within the merged images is indicative of the co-localization of EuCF-DTG nanoparticles (green) within the activated macrophages (red). Figure 3.9B shows corresponding TEM images of liver and spleen sections 5-days post injection of EuCF-DTG nanoparticles. Blacks dots can be clearly seen within TEM images in both IV- and IM-injected animals and represent the cellular localization of nanoparticles within macrophages and immune cells in both the liver and

the spleen. Such immunohistological and TEM data are in strong agreement with *in vitro* results listed in the previous chapter and suggests that nanoparticle retention within these tissues persists for at least 5 days. Parallel immunohistochemistry studies were performed in rhesus macaque tissues 5-days post IM injection of EuCF-DTG nanoparticles; histological evaluation was conducted in accordance with the guidelines of the Society of Toxicologic Pathology, and no anomalies were found other than those that are common in SIV infected animals. Biochemical or hematological effects of EuCF-DTG nanoparticle administration to rhesus macaques were not observed.

3.4 Discussion

Synthesized theranostic nanoparticles contain individual functional components that improve their diagnostic and therapeutic potential. *First*, the CF component enhances MRI signal sensitivity and specificity measures [223]. The images show excellent T2 relaxivity. As such, they can be readily used for ARV biodistribution studies. High relaxivity results in enhanced sensitivity for ferrite quantification. *Second*, the nanoparticle's unique spinel structure permits the incorporation, in a formed lattice, of rare earth elements. This includes, but is not limited to, neodymium, Eu^{3+} and gadolinium [223, 242]. *Third*, Eu^{3+} provides magnetic and fluorescence capabilities. *Fourth*, the translational potential is realized through the nanoparticle's biocompatibility [223]. This is facilitated through the outer "soft" lipid layer of the EuCF-DTG nanoparticles [214, 243]. *Fifth*, Eu^{3+} doped CF can be surface-modified by FA for functionalization [223]. *Sixth*, the formed FA-EuCF-DTG nanoparticles are highly stable and as such can be made for systemic use. *Seventh*, the FA-EuCF-DTG nanoparticles are hydrophilic with a narrow size distribution. Each contains a "hard" inner matrix of an organic-inorganic hybrid of EuCF and PCL, which enables the nanoparticles to be loaded with hydrophobic ARVs and have limited to no toxicities [214]. *Eighth*, the nanoparticles unique physicochemical properties facilitate entry into cells. Indeed, the core is made up of EuCF, PCL and DTG, while the outer lipid layers are formed

with PC, DSPE-PEG2000 and DOPE. The lipid surrounding the EuCF-DTG core serves to facilitate rapid uptake by macrophages and as such effectively distribute drug into tissue viral reservoirs. *Ninth*, the lipid layer shell over the nanoparticle's core provides inherent stability and appropriately sized nanoparticles can be readily made in order to optimize cell and tissue delivery. Indeed, the EuCF-DTG and FA-EuCF-DTG nanoparticles are homogeneous with relatively narrow nanoparticle size distribution and retention of drug loading capacities and antiretroviral activity. *Tenth*, the nanoparticle's size and shape are comparable to that of LASER ART being developed for clinical use [202, 229]. The nanoparticles are remarkably consistent in morphology. Electron microscopic images indicate that all synthesized nanoparticles display lipid layers outside the EuCF-DTG or FA-EuCF-DTG core matrix. The latter appears smooth with uniform topography that is particularly important in reducing systemic adverse events. *Eleventh*, the uptake of nanoparticles by macrophages is optimized, as endocytosis is facilitated by spherical or semi-rod-shaped nanoparticles [206, 244-246].

Prior reports demonstrated that the FA receptor beta (FR-β), highly expressed on macrophages, could facilitate nanoparticle cell entry [216, 217, 220]. We have previously demonstrated significantly higher macrophage uptake of FA-decorated nanoformulations compared to replicate nanoformulations without decoration [206, 247]. In particular, ARV nanoparticles that were decorated with FA showed higher atazanavir levels in lymphoid organs such as the spleen and lymph nodes compared to non-decorated particles. Notably, drug levels paralleled FR-β staining in both macrophage-rich parafollicular areas of spleen and lymph nodes. FA targeting of abacavir nanoparticles improved drug and pharmacokinetics and antiretroviral activity [196]. Moreover, demonstration of human serum albumin nanocapsules that were surface modified with FA led to macrophage internalization [218]. Formulation uptake was three-fold higher in FR-β-positive macrophages than in macrophages not expressing FR-β. Similarly, FR-β-specific targeting of methotrexate nanoparticles suppressed inflammation associated with type II

collagen-induced arthritis models [219]. Furthermore, macrophage targeting of FA-conjugated iron oxide nanoparticles were described [215] and reflect our own results. In the current report, we showed higher uptake of FA-EuCF DTG nanoparticles in reticuloendothelial tissues (Figure 3.4, Figure 3.6). Moreover, we confirmed that FA decorated nanoparticles showed higher macrophage uptake (Figure 3.4) [206, 247]. Therefore, the macrophage-targeting strategy presented in our study for FA-mediated uptake of nanoparticles will enable targeting of nanoformulated drug particles.

Nanoparticle migratory behavior was investigated in rodents and non-human primates. MR images showed decreased signal intensity within the liver and spleen. Corresponding MRI T2 values revealed that iron levels matched the drug PK and biodistribution profiles. Validations were made by analysis of cobalt and drug content. No significant differences in deviation from linearity for either drug or cobalt levels were found over time. Co-localization of nanoparticles within macrophages was seen using confocal and electron microscopy in both cell culture and histopathological tissue analyses, highlighting the importance of Eu3+ as a fluorescent tag. Assay of cobalt and iron along with drug content provided MRI confirmation results. Our finding of preferential macrophage uptake of nanoparticles paralleled the observed PK and biodistribution results [243-246]. With the successful development of the multi-modal nanoprobes in rhesus macaques, we posit that macrophage-targeted theranostics can be useful as a testing platform to assess drug biodistribution in humans. Macrophages loaded with theranostic nanoparticles can move throughout the body and target tissue sites of residual latent virus [207, 248, 249]. Notably, the nanoparticles maintain their integrity and ARV efficacy. Most importantly, nanoparticle distribution can be monitored and tracked in real-time [207, 223]. Overall, our newly-developed platform provides a means to accurately and effectively optimize the delivery of antiretroviral drug-loaded nanoparticles into macrophages.

In conclusion, the efficacy and structural integrity of the nanoprobe platform was confirmed in rats and SIV-infected rhesus macaques by MRI. FA-functionalized EuCF-DTG nanoparticles showed enhanced nanoparticle uptake and antiretroviral activity. EuCF-DTG was localized to recycling macrophage endosomal compartments without evidence for cytotoxicity.

3.5 Figures

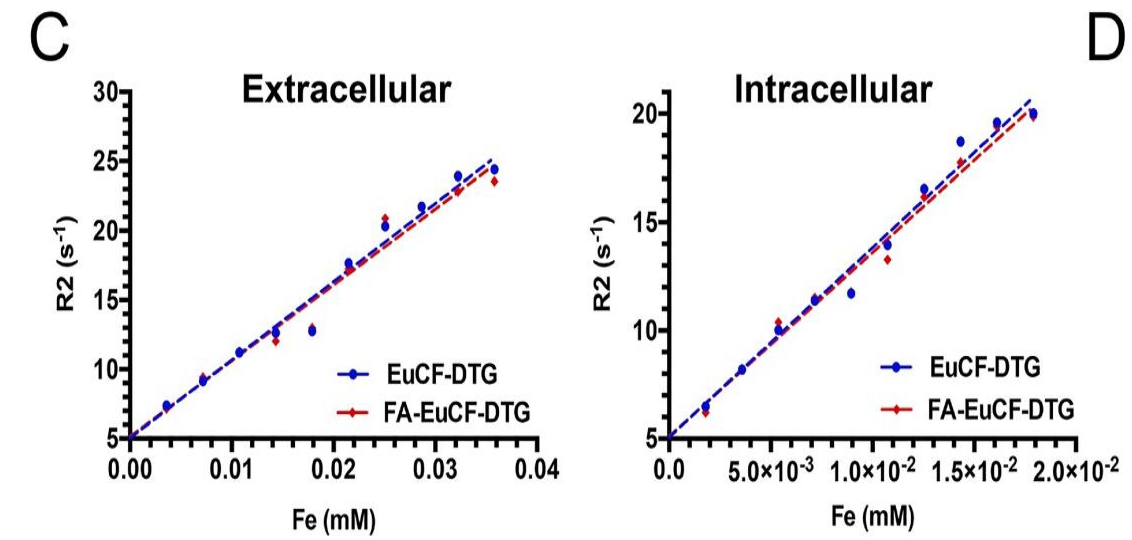
C
Extracellular
R2 (s-1)
Fe (mM)
EuCF-DTG
FA-EuCF-DTG
D
Intracellular
R2 (s-1)
Fe (mM)
EuCF-DTG
FA-EuCF-DTG

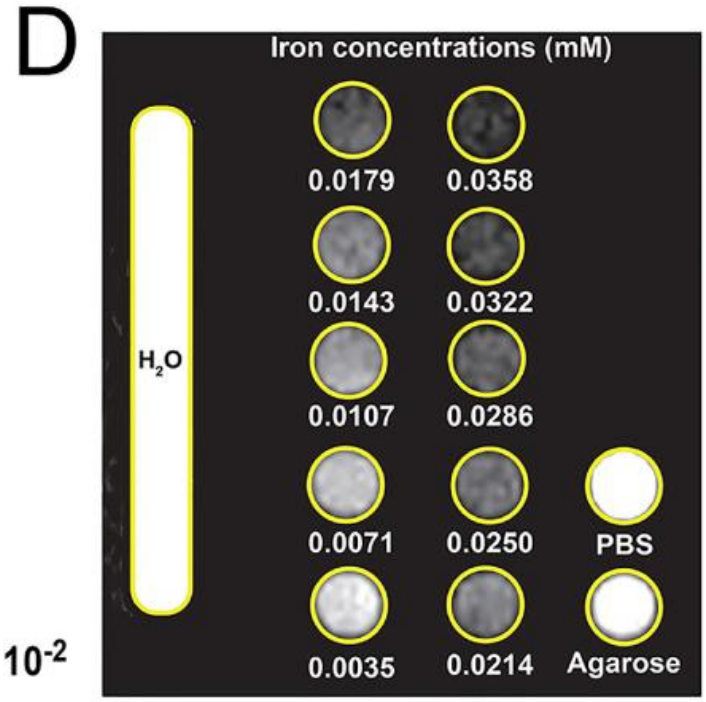
D
Iron concentrations (mM)
H2O
0.0179
0.0358
0.0143
0.0322
0.0107
0.0286
0.0071
0.0250
PBS
0.0035
0.0214
Agarose
10-2

Figure 3.1 MRI relaxometry measurements (c-d) MRI signal enhancement effects of EuCF-DTG and FA-EuCF-DTG nanoparticles were determined by calculating nanoparticle relaxivity r2 (mM−1s−1) in both PBS (extracellular) and MDM (intracellular) using a 7T MRI scanner. (C) Nanoparticle relaxation rates (R2) in both PBS and MDM increased linearly with increasing iron concentrations. (D) T2-weighted images of EuCF-DTG nanoparticles in PBS demonstrate signal reduction with increasing concentrations of iron.

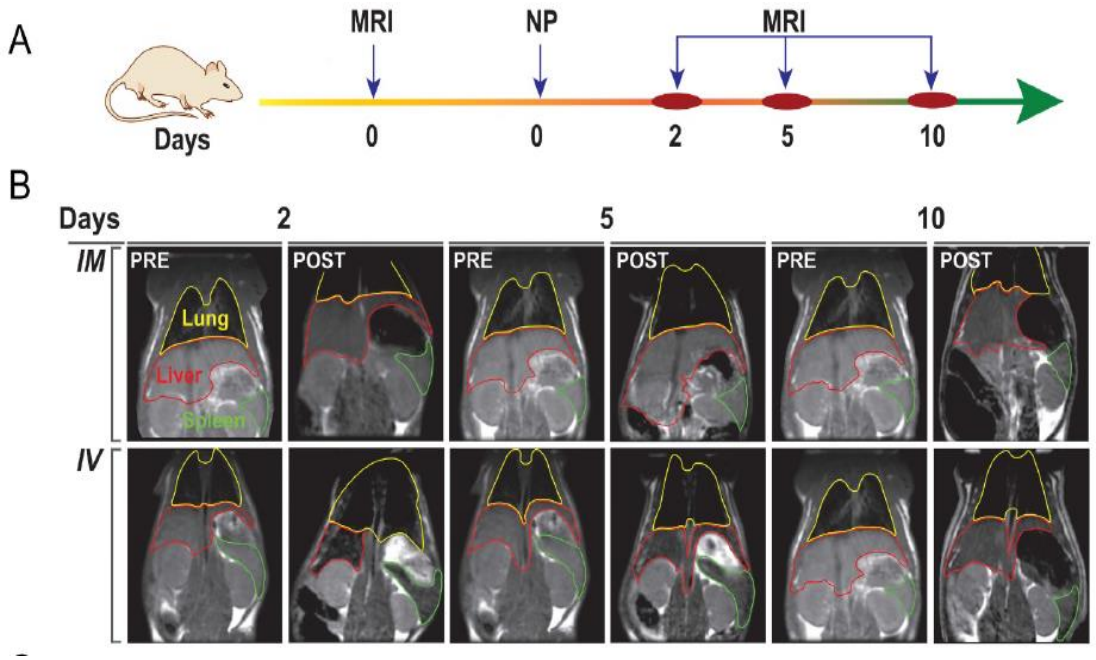

Figure 3.2 Nanoparticle biodistribution tests. (A) Time line of the experimental procedure in the rats is shown (NP: nanoparticles). (B) Representative T2 maps of rats at 2, 5 and 10 days after IV or IM administration of 2 mg iron/kg as EuCF-DTG nanoparticles (yellow: lung; red: liver; green: spleen).

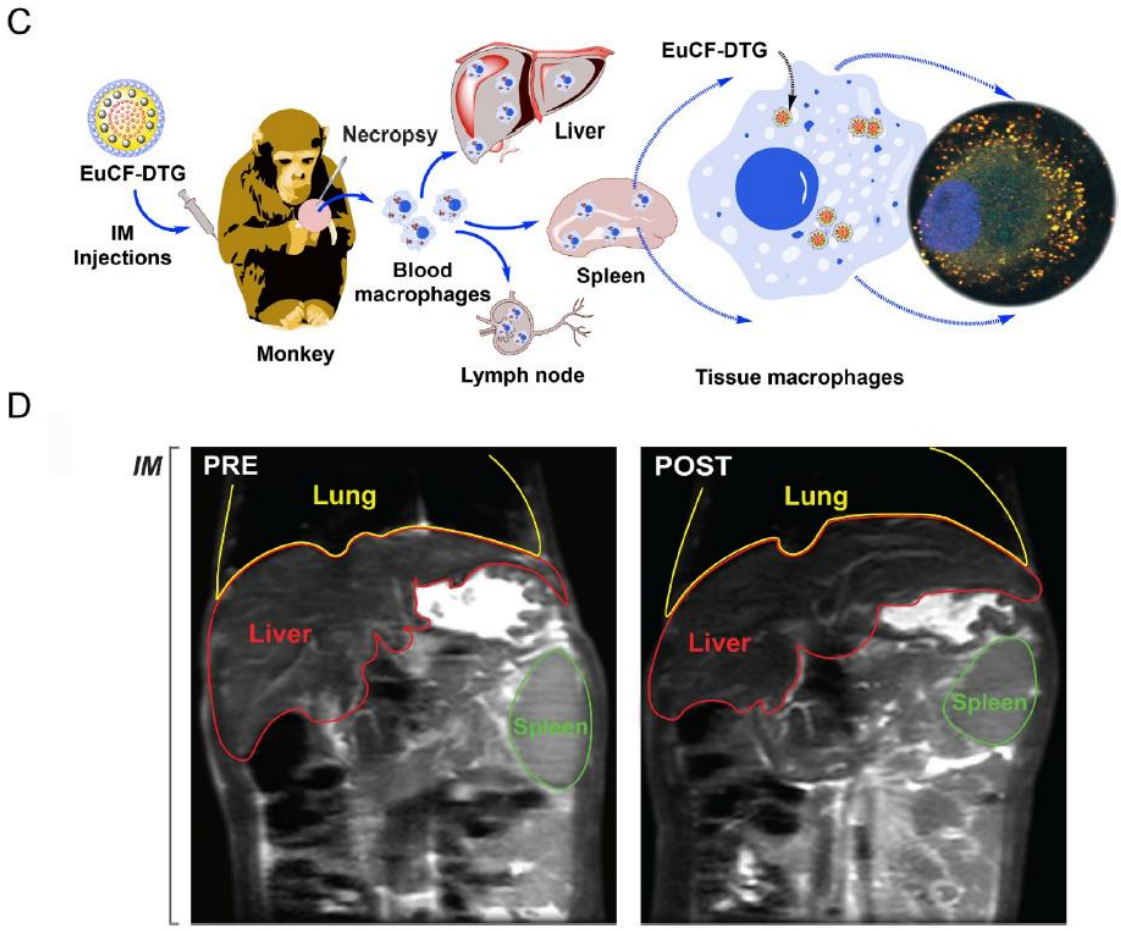

Figure 3.3. (C) Schematic diagram of macrophage-based biodistribution of EuCF-DTG nanoparticles in the reticuloendothelial system of rhesus macaques (IM: intramuscular). (D) Representative T2-weighted images of a macaque at 5 days after IM administration of 2 mg iron/kg as EuCF-DTG nanoparticles (yellow: lung; red: liver; green: spleen).

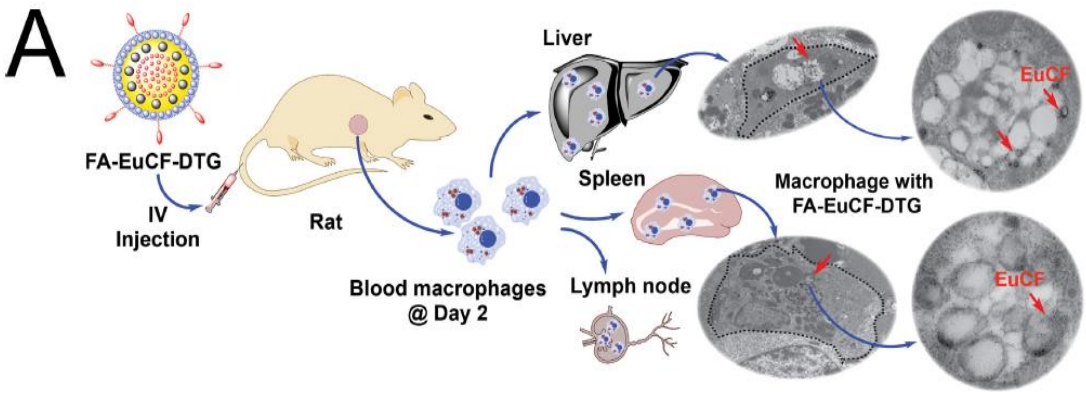
A
FA-EuCF-DTG
IV
Injection
Rat
Blood macrophages
@ Day 2
Liver
Spleen
Lymph node
Macrophage with
FA-EuCF-DTG
EuCF
EuCF

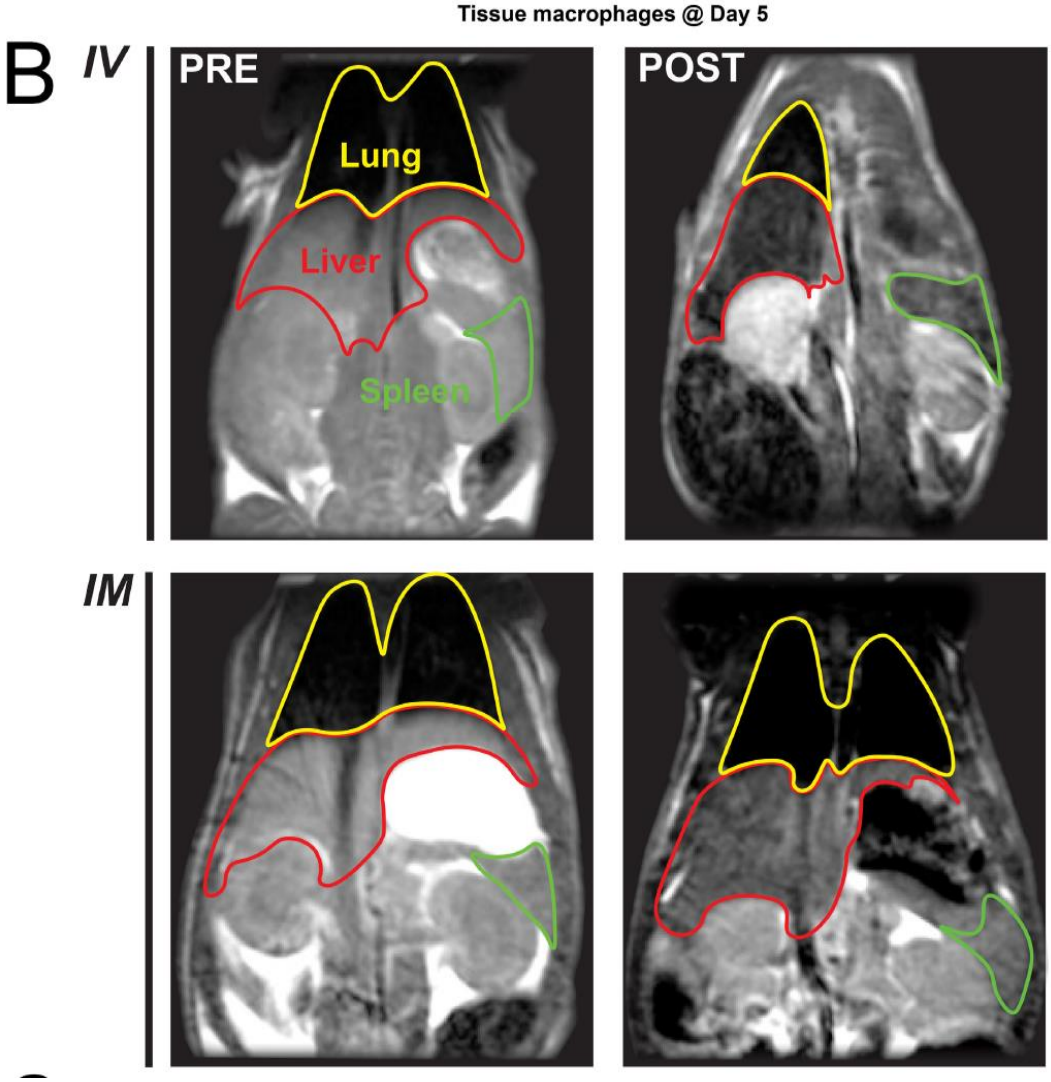
Tissue macrophages @ Day 5
B
IV
PRE
POST
Lung
Liver
Spleen
IM

C

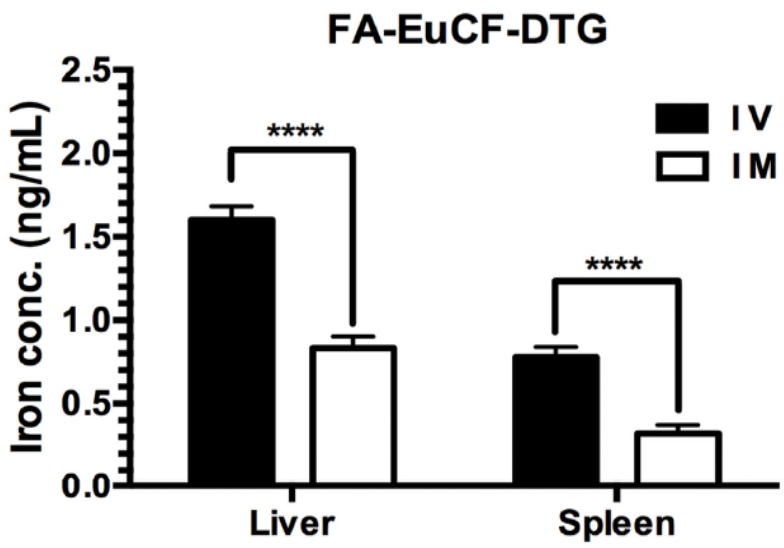

Figure 3.4: **FA-EuCF-DTG nanoparticle biodistribution**: (A) Schematic diagram of macrophage-based biodistribution of particles in rats reticuloendothelial system (IV: intra intravenous). Nanoparticles were administrated in Male Sprague Dawley rats followed by IV or IM injection and underwent MRI scanning immediately before injection as well as 2 and 5 days post-injection. (B) MR images of rats at day 5 after IM/IV administration of 2 mg iron/kg FA-EuCF-DTG particles (yellow: lung; red: liver; green: spleen). (C) MRI T2 mapping again quantified the iron concentrations in the liver and spleen. Statistical differences were determined using one-way ANOVA among groups; followed by Student's t-test. (****$p < 0.0001$).

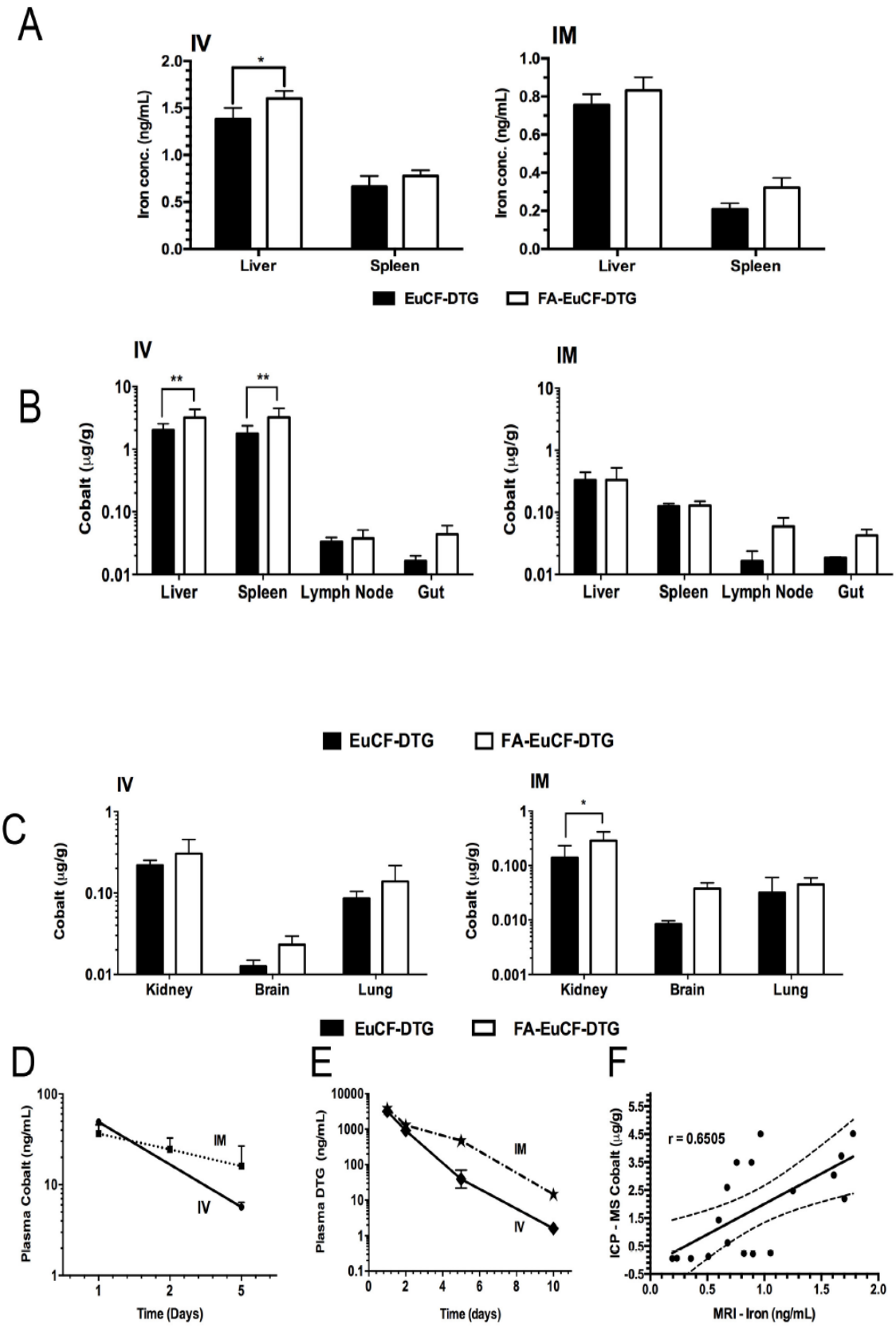
A
IV
IM
Iron conc. (ng/mL)
Liver
Spleen
EuCF-DTG
FA-EuCF-DTG
B
Cobalt (µg/g)
Liver
Spleen
Lymph Node
Gut
C
Kidney
Brain
Lung
D
Plasma Cobalt (ng/mL)
Time (Days)
E
Plasma DTG (ng/mL)
Time (days)
F
ICP - MS Cobalt (µg/g)
MRI - Iron (ng/mL)
r = 0.6505

Figure 3.5: Biodistribution of FA-EuCF-DTG nanoparticles in rats. (A) Iron level comparisons for EuCF-DTG and FA-EuCF-DTG nanoparticle in liver and spleen measured by MRI. (B) Cobalt concentrations within lymphoid tissues and (C) brain, kidney and lung cobalt levels measured by ICPMS. (D) Plasma cobalt and (E) DTG concentrations were measured after IV or IM administration for EuCF-DTG nanoparticles. (F) Pearson's correlation in liver and spleen tissues of cobalt levels (determined by ICPMS) in tissues as compared to iron levels determined by MRI five days after injection of EuCF-DTG nanoparticles (2 mg iron/kg). Statistical differences were determined using two-way ANOVA among groups. (*$p < 0.01$; **$p < 0.001$).

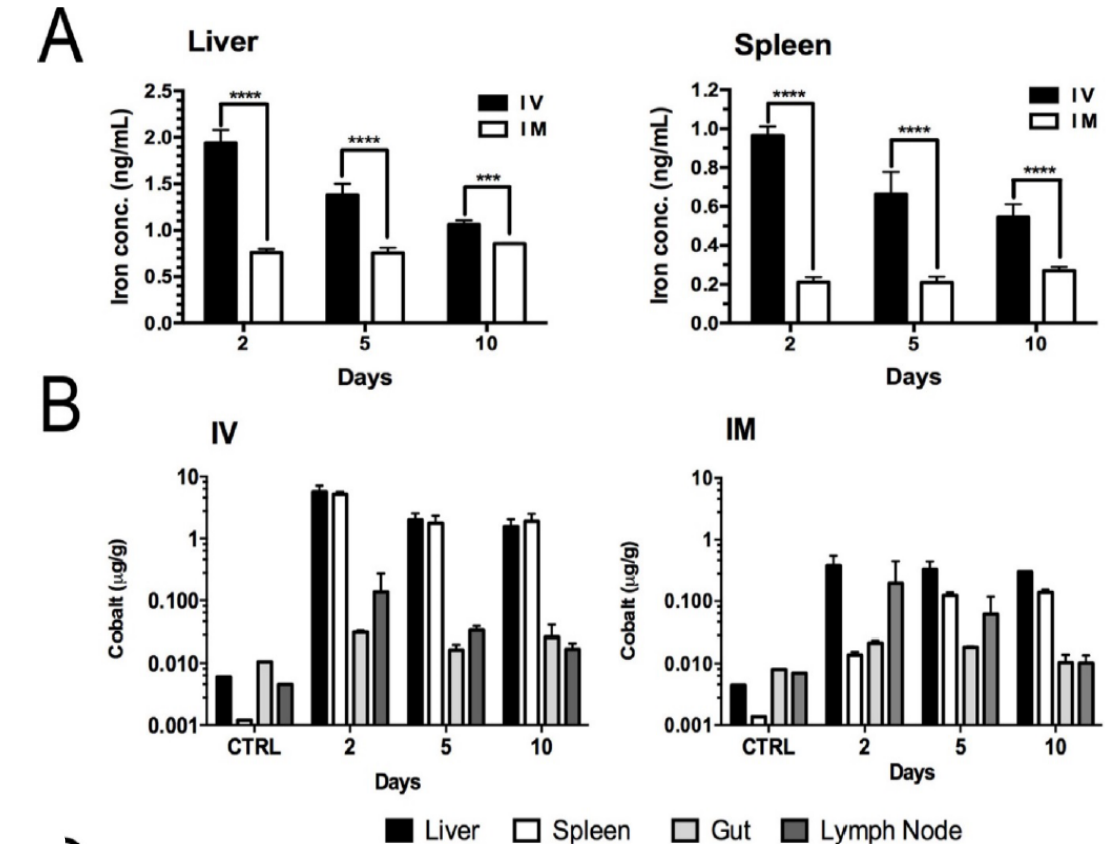
A
Liver
Spleen
Iron conc. (ng/mL)
IV
IM
****
***
Days
B
IV
IM
Cobalt (µg/g)
CTRL
Days
Liver
Spleen
Gut
Lymph Node

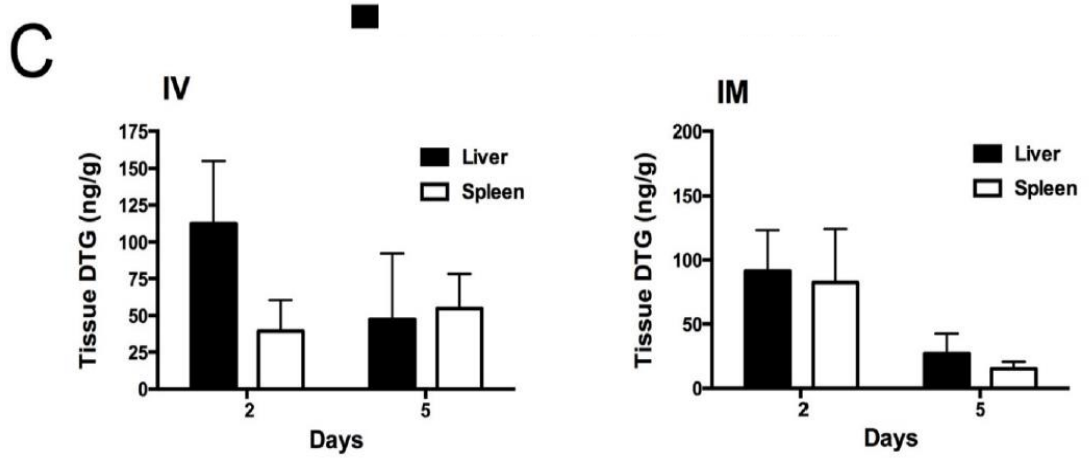
C
IV
IM
Tissue DTG (ng/g)
Liver
Spleen
Days

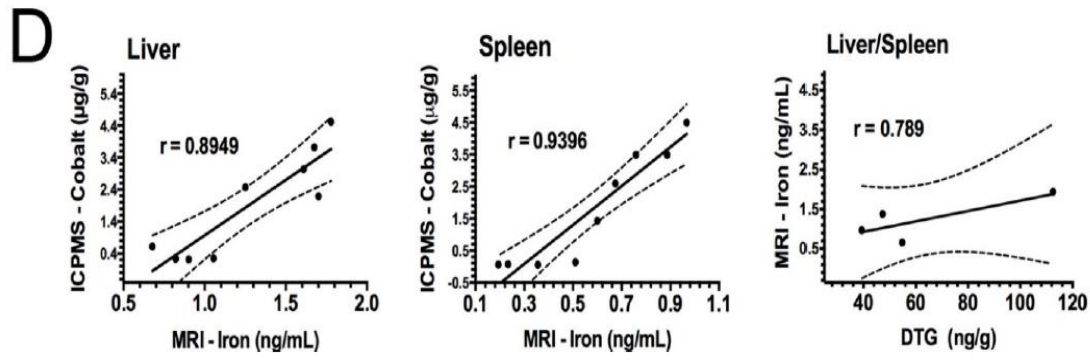
D
Liver
Spleen
Liver/Spleen
ICPMS - Cobalt (µg/g)
MRI - Iron (ng/mL)
r = 0.8949
r = 0.9396
r = 0.789
DTG (ng/g)

Figure 3.6 Drug and cobalt concentrations after parenteral EuCF-DTG administration. Sprague Dawley rats were administered EuCF-DTG nanoparticles (2 mg/kg iron content) by IM or IV injection on day 0 and sacrificed on days 2, 5 or 10. Plasma was collected for drug analysis on days 1, 2, 5, and 10 after treatment. DTG and cobalt levels were determined by UPLC-MS/MS and ICP-MS, respectively, at days 2, 5 and 10. (A) Quantitation of iron in liver and spleen by MRI tests. (B) Cobalt concentrations. (C) Tissue DTG concentrations. (D) Pearson's correlation of iron (determined MRI), cobalt (determined ICP-MS) and DTG (determined UPLC-MS/MS) concentrations in liver and spleen tissues five days after IV/IM administration of nanoparticles. Statistical differences were determined using two-way ANOVA among groups; ***$p < 0.001$; ****$p < 0.0001$.

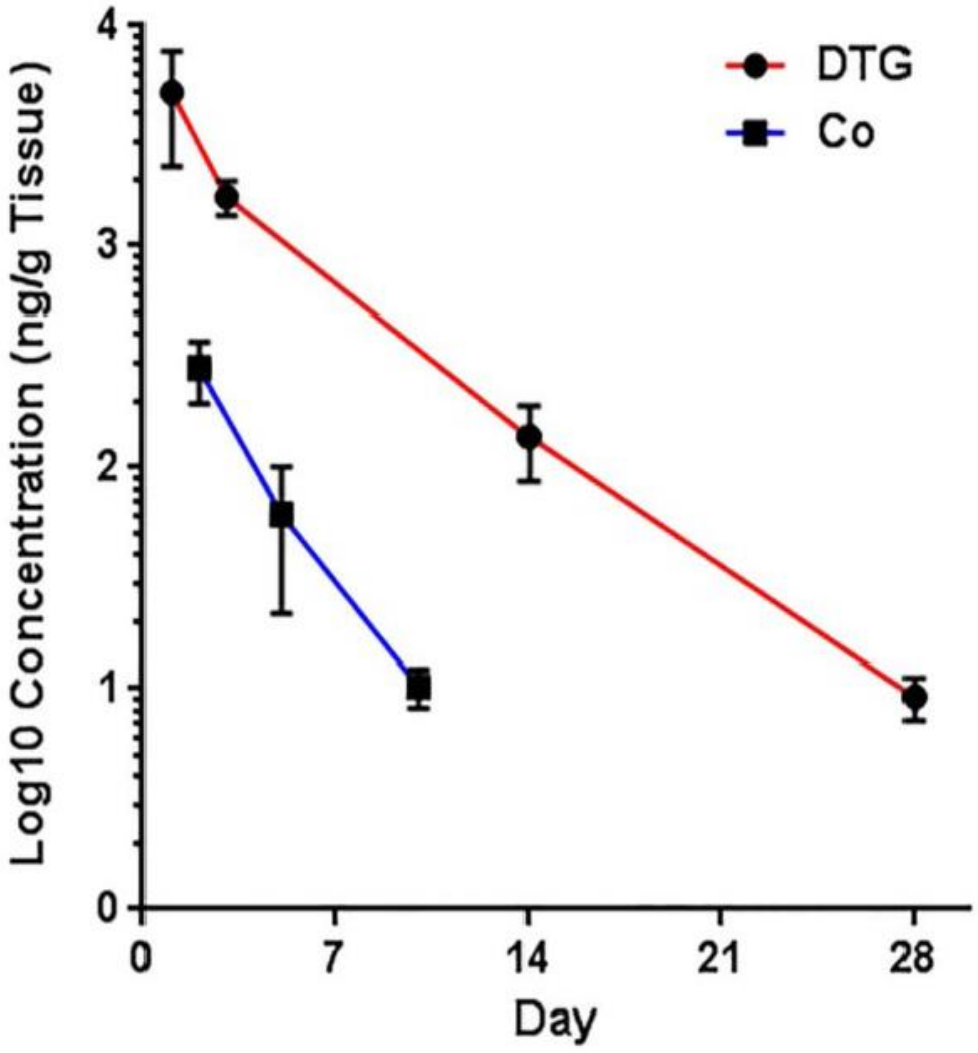

Figure 3.7 Prediction correlations of cobalt and DTG levels in tissues (DTG data sets were obtained from an independent publication [12])**.** Cobalt and DTG levels in the tissues were analyzed by ICP-MS and UPLC-MS/MS. No significant differences in deviation from linearity for either function ($p = 0.6667$ and $p = 1.0000$) were observed. In addition, no significant differences were observed in the rate of change, by slope measures, in either DTG or cobalt concentrations ($p = 0.476$). Noted differences in line elevation ($p = 0.0011$) were linked to the relative concentrations of each component (cobalt and DTG) administered.

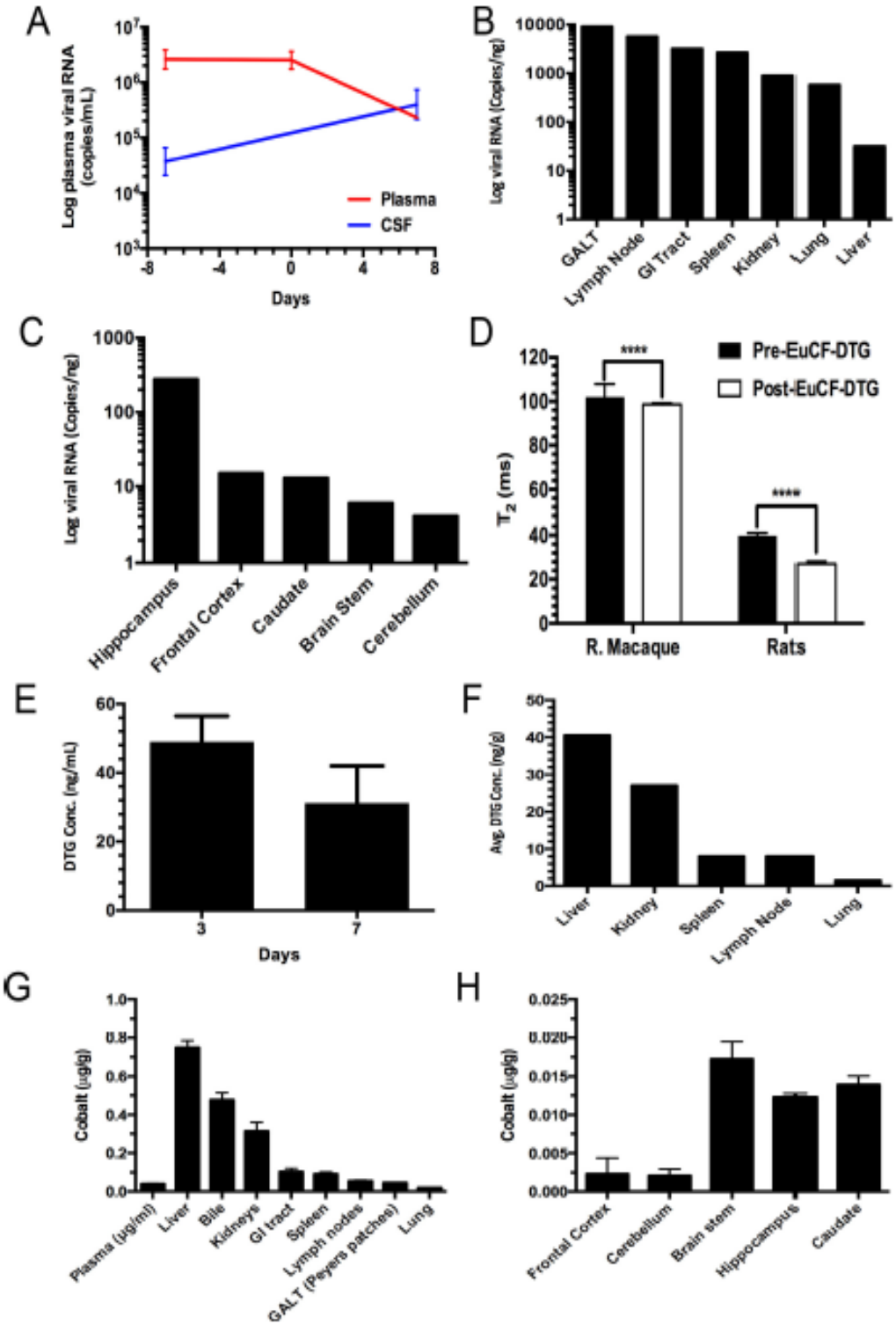
A
Log plasma viral RNA (copies/mL)
Plasma
CSF
Days
B
Log viral RNA (Copies/ng)
GALT
Lymph Node
GI Tract
Spleen
Kidney
Lung
Liver
C
Log viral RNA (Copies/ng)
Hippocampus
Frontal Cortex
Caudate
Brain Stem
Cerebellum
D
Pre-EuCF-DTG
Post-EuCF-DTG
T2 (ms)
****
****
R. Macaque
Rats
E
DTG Conc. (ng/mL)
Days
F
Avg. DTG Conc. (ng/g)
Liver
Kidney
Spleen
Lymph Node
Lung
G
Cobalt (µg/g)
Plasma (µg/ml)
Liver
Bile
Kidneys
GI tract
Spleen
Lymph nodes
GALT (Peyers patches)
Lung
H
Cobalt (µg/g)
Frontal Cortex
Cerebellum
Brain stem
Hippocampus
Caudate

Figure 3.8: **Biodistribution of EuCF-DTG nanoparticles in rhesus macaque tissues and effect on simian immunodeficiency virus (SIV) RNA loads**. (A-C) plasma (results are shown as means ± SEM; n=3) and tissue viral RNA loads of SIV-infected rhesus macaque. (D) Rat and rhesus macaque T2 relaxation in liver, (E-F) effect of EuCF-DTG treatment on plasma and comparison of DTG concentrations in post-mortem tissues measured by ICP-MS 5 days post IM injection of EuCF-DTG nanoparticles and (G-H) cobalt concentrations in the reticuloendothelial organs and brain regions at 2 mg iron/kg dosage.

A

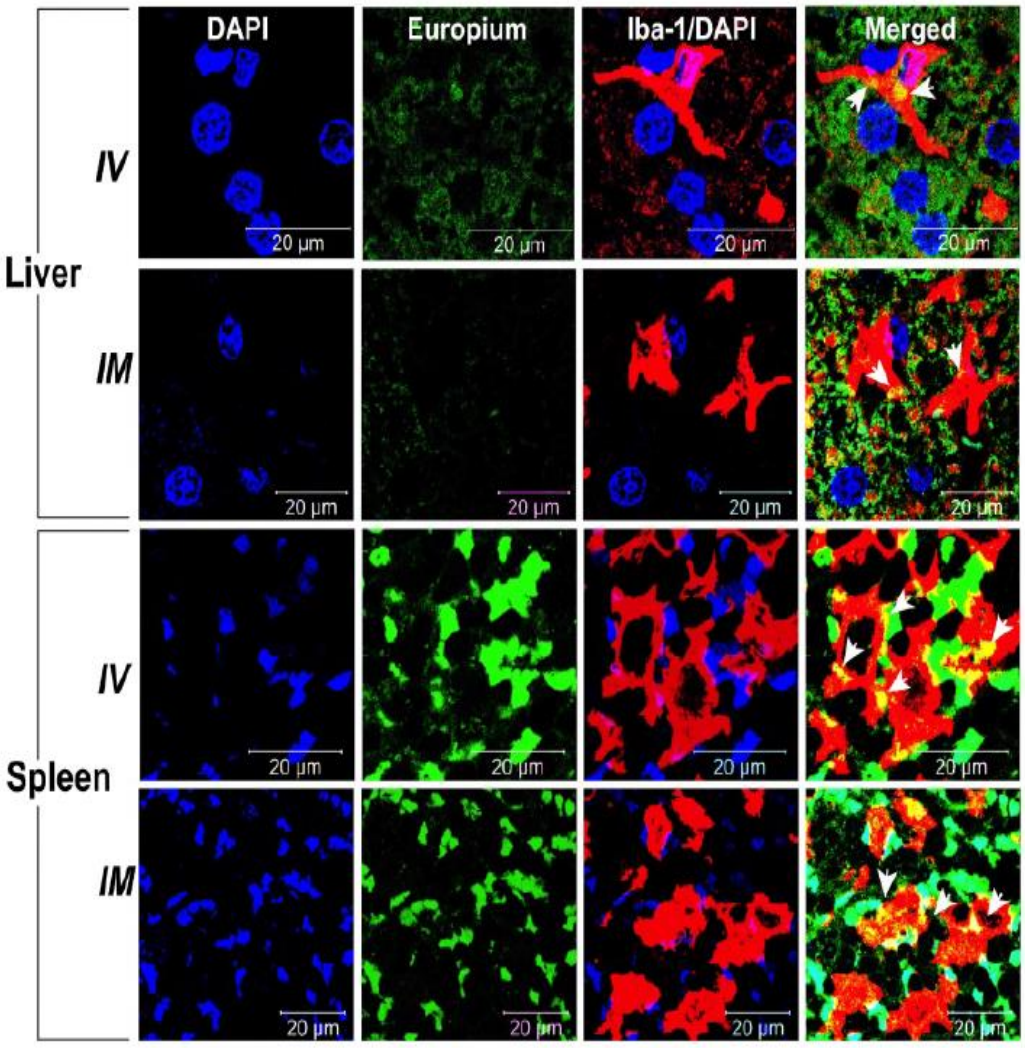

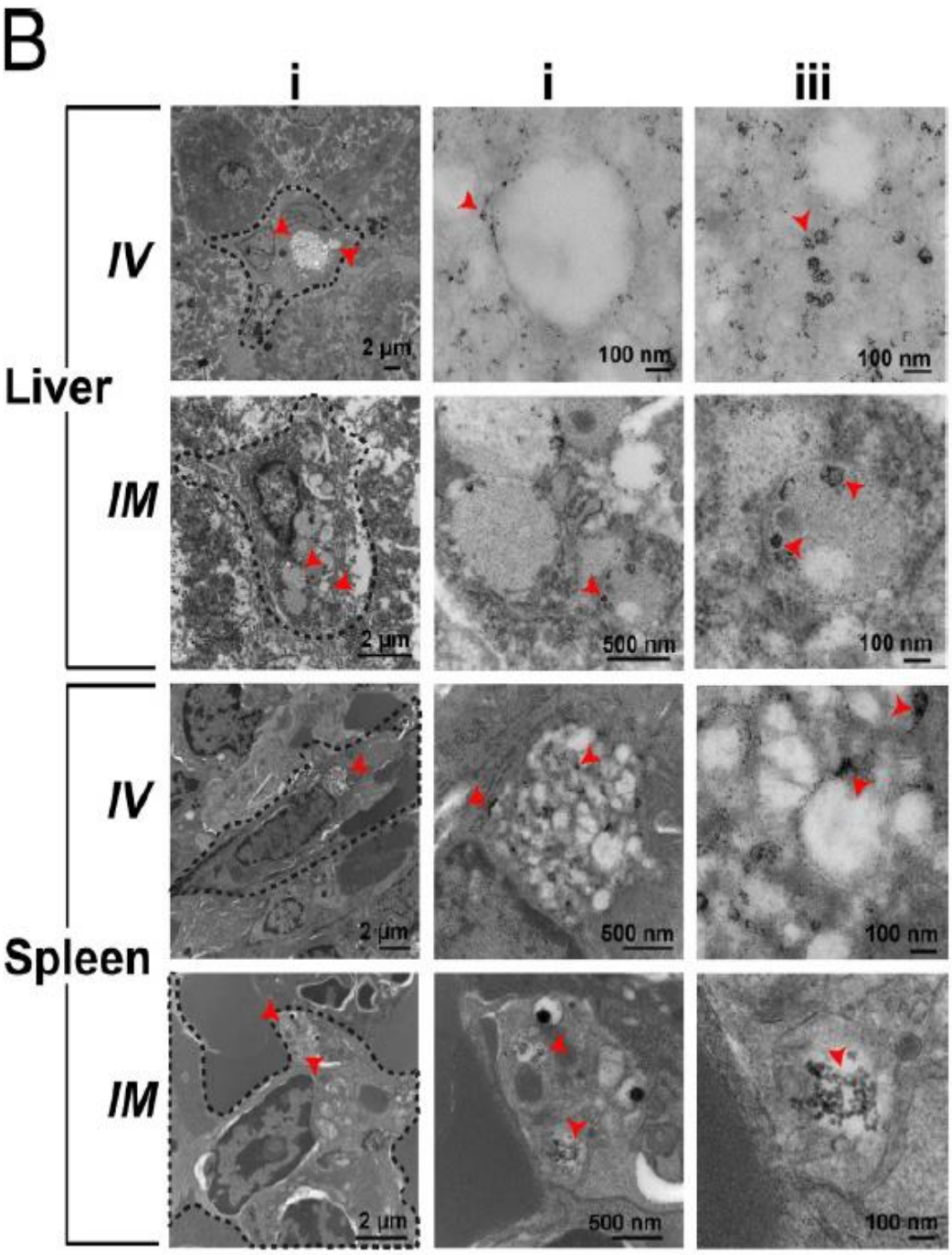
B
i
i
iii
IV
IM
Liver
IV
IM
Spleen
2 µm
100 nm
100 nm
2 µm
500 nm
100 nm
2 µm
500 nm
100 nm
2 µm
500 nm
100 nm

Figure 3.9 Immunohistochemical and morphological localization of EuCF-DTG nanoparticles. (A) Representative tissue sections of liver and spleen of rats administered EuCF-DTG nanoparticles (green) were stained for Iba-1 (red) on activated macrophages. Nanoparticles were detected in macrophages in both liver and spleen. Arrows in the merged figures indicate co-localization of nanoparticles in macrophages. Images were captured with 63X objective on a Zeiss LSM 710 confocal microscope. (B) TEM of liver and spleen 5 days after IV or IM injection of EuCF-DTG nanoparticles (2 mg iron/kg). Panels ii and iii are higher-powered images from regions indicated by red arrowheads in panel i. Presence of nanoparticles (black dots) is seen in macrophages in both liver and spleen (panel ii and iii, Figure S11. FA-EuCF-DTG nanoparticles were seen localization in reticuloendothelial tissues by TEM tests

CHAPTER 4

Nanoformulated antiretroviral therapy attenuates brain metabolic oxidative stress

4.1 Introduction

HIV-1 infection is associated with a spectrum of comorbid conditions that includes the CNS [250-252]. Nonetheless, many of these conditions have been either reduced or eliminated following the widespread use of ART. ART has enabled infected people to live nearly normal lives by reducing plasma and tissue HIV-1 RNA to levels below the limits of detection [7, 174]. Nonetheless, disease morbidities remain, albeit at lower levels, both as a consequence of viral infection and concomitant illnesses. This includes abuse of illicit drugs, nutritional deficiencies, neuropsychiatric disorders, and a variety of comorbid infectious diseases that include hepatitis and opportunistic viral and parasitic infections. Malignancies, depression, and immune dysfunctions are specifically linked to cognitive and behavioral abnormalities as areARVs themselves. The latter plays a role in direct neurotoxicity and consequent neuropsychiatric compromise [253, 254]. Among them, to date, efavirenz is known to affect neuronal function [255]. The potential effects that other ARVs may have on brain function and metabolism remain poorly understood. Such drug-associated toxicities could become more pronounced as commonly used ARVs are transformed into LASER ART. Such achievements have been made possible by chemical drug modifications enabling lipophilic hydrophobic nanocrystals to be created that markedly prolong the drug's apparent half-life [256, 257]. One of the ARVs, dolutegravir (DTG), has received notable attention for its potential for transformation into a long-acting drug as well as its potential albeit rare toxicities [256]. In 2013, DTG was approved by the U.S. Food and Drug Administration and soon afterwards broadly incorporated in combination ART regimens based on its potency and limited viral resistance patterns [258-260]. While the drug is generally well tolerated, reports have emerged that in some aged patients and females, adverse events could signal off-target drug effects involving the CNS [256]. Given DTG's key role in HIV-1 therapeutic regimens, studying the intricate metabolic mechanism of how and why neural effects occur could improve disease outcomes. Further, as DTG use increases among older patients, the knowledge of who could be at risk and

any means to prevent it appears timely. The realization of LASER ART could, in part, facilitate any untoward drug effects as the circulating drug half-life broadens further. Alternatively, nanoformulated drug improvements in ARV uptake, retention, and biodistribution into tissues and organs where free drug may not easily reach could attenuate adverse events by further reducing the impact of virus on disease events and in control of untoward macrophage inflammatory responses. Indeed, while LASER ART can significantly improve antiretroviral clinical potency, it requires high doses to maintain the required four times the effective dose 90 in plasma to elicit sustained viral restriction [257, 261-266]. With this in mind, we investigated the metabolic effects of free and nanoformulated DTG in five different anatomical brain regions using untargeted and unbiased metabolomic detections. DTG was administered intramuscularly at 45-mg/kg doses over a 7-day time course. This enables up to 100 times the oral therapeutic plasma concentration. Reported steady-state plasma concentration obtained from HIV-1-infected adults after ten doses of monotherapy with 50 mg (once daily) DTG tablets is 3.34 μg/mL (Cmax), whereas in the current study, plasma concentration of injectable DTG for a single free DTG injection was up to 11.29 μg/mL [267, 268]. The frontal cortex (FC), ventral cortex (VC), dorsal cortex (DC), hippocampus (H), and cerebellum (CR) were dissected and then analyzed using liquid chromatography-mass spectrometry (LC-MS)- based global metabolomics. The results showed that “high parenteral doses” of free DTG induced disordered brain metabolism as defined by increases in specific energy-related metabolites and their pathways all linked to oxidative cellular processes. These were seen predominantly in the cerebellum and cortex and were attenuated to basal levels by the use of DTG delivered as a nanoformulation. While higher dosages of DTG could affect neurotoxicities, any concern in such administration as a long-acting antiretroviral was abrogated by an established nanoformulated drug delivery system.

4.2 Materials and methods

4.2.1 Preparation and characterization of nanoformulated DTG

For preparation of P407-DTG, 0.5% (w/v) P407 was mixed with 1% drug. The suspensions were homogenized at 20,000 psi using an Avestin Emulsiflex C3 homogenizer (Avestin Inc., Ottawa, ON, Canada) until the desired particle size (300– 400 nm) was reached. Free polymers and nonencapsulated drug particles were removed by centrifugation; the nanoparticles were resuspended in 0.2% P407. Drug loading was determined using reversed-phase high-performance liquid chromatography (HPLC) and ultra-performance liquid chromatography tandem mass spectrometry (UPLC-MS/MS) as described. Particle size, polydispersity, and zeta potential for the nanoformulations were determined by dynamic light scattering using a Malvern Zetasizer Nano-ZS instrument (Malvern Instruments Inc., Westborough, MA, USA).

4.2.2 DTG injection and brain tissue collection

Both nanoformulated and free DTG with their corresponding controls (vehicle only) were introduced by intramuscular injections with a loading dose of 45 mg/kg. Animals treated with nanoformulations were treated once while the free DTG group was treated every other day over a 1-week span (i.e., 4 total injections over 7 days) to maintain drug levels in the animals. Free DTG was dissolved in a buffer of (v/v) 43% ethanol, 5% cremophor, 20% propylene glycol (propane-1,2-diol), and 32% PBS. In the global metabolomics analysis, the same buffer and nanoformulation without DTG were used as controls. Mice were anesthetized with 1–2% isoflurane in oxygen and then aligned in a water-jacketed holder for microwave irradiation with a Muromachi Microwave Fixation System (10-kW model, Muromachi Kikai Co., Ltd., Chuo-ku, Tokyo, Japan). Irradiation time was 800 ms at 4.9 kW [269]. Single voxel localized spectra were acquired post-mortem at the midbrain to ensure metabolite level stabilization using point-resolved spectroscopy. Spectra were acquired with a repetition time of 4 s and echo time of 50 ms, 128 averages, using birdcage coil transmit, and received on a 7-Tesla/16-cm Bruker Pharmascan (Karlsure, Germany) MRI/MRS system. Single-scan, localized, unsuppressed water signals were acquired as a reference for metabolite normalization. Brains with abnormal N-acetylaspartate (NAA) or lactate concentrations

were eliminated from further analysis. Five animals were selected for further brain dissection and analysis. All specimens were from the same genetic strain (Balb/cJ), males and similar ages (7 weeks). After spectroscopic validation of microwave irradiation euthanasia, brains were isolated and initially split into hemispheres, with both hemispheres dissected into subregions. Subregional dissection followed anatomical boundaries to separate the frontal cortex, ventral cortex, dorsal cortex, hippocampus, and cerebellum. Following dissection, all tissues were flash frozen in dry ice and stored at − 80 °C.

4.2.3 Metabolome extraction

Brain tissue subregions were extracted as previously described [270]. Briefly, 0.6 mL of cold methanol:H2O (4:1, v/v) were added per 10 mg tissue (solvent volume was adjusted accordingly to tissue weight). Homogenization was performed with glass beads in a homogenizer and sonicated in an ice bath for 10 min. The mixtures were then transferred to 1.5-mL Eppendorf vials and rinsed with additional 200 μL extraction solvent. To precipitate proteins, the samples were incubated for 1 h at − 20 °C, followed by a 15-min centrifugation at 13,000 rpm at 4 °C. The resulting supernatant was evaporated to dryness in a vacuum concentrator. The dry extracts were then reconstituted in acetonitrile:H2O (1:1, v/v), normalized by tissue weight, sonicated for 10 min, and centrifuged for 15 min at 13000 rpm and 4 °C to remove insoluble debris. The supernatants were transferred to HPLC vials and stored at − 80 °C prior to LC-MS analysis.

4.2.4 HILIC-MS and data analysis

The extracts were analyzed on a 6550 iFunnel QTOF mass spectrometer coupled with a 1290 UPLC system (Agilent Technologies, Santa Clara, CA). For global metabolomics, a Luna Aminopropyl, 3 μm, 150 mm × 2.0 mm I.D. HILIC column (Phenomenex, Torrance, CA) was used. The mobile phase was composed of A = 20 mM ammonium acetate and 40 mM ammonium hydroxide in 5% ACN and B = 95% acetonitrile. A linear gradient from 100% B (0–2 min) to 100%

A (17–33 min) was applied with a 15-min re-equilibration time. The flow rate and injection volume were 250 μL/min and 5μL, respectively .ESI source condition swere set as follows: dry gas temperature, 200 °C; flow, 11 L/min, fragmentor, 380 V; sheath gas temperature, 300 °C; flow, 9 L/min; nozzle voltage, 500 V; and capillary voltage,− 500 Vin ESI-negative mode. The instrument was set to acquire data over the m/z range 50–1000, with the MS acquisition rate of 1 spectra/s. The sample sequence was randomized to avoid systematic decreases in signals over sample sets. For the MS/MS of selected precursors, the default isolation width was set as narrow (~ 1.3 m/z), with a MS acquisition rate at 2 spectra/s and MS/MS acquisition at 2 spectra/s to acquire over the m/z range 50–1000 and 25–1000; respectively. MS/MS data were acquired at the collision energy of 20 V. LC-MS data were converted to mzXML files using Masshunter Acquisition Software (Agilent Masshunter 6.0B). The mzXML files were uploaded to XCMS Online web platform for data processing (https://xcmsonline.scripps. edu) including peak detection, retention time correction, profile alignment, and isotope annotation [271]. Data were processed using both pairwise and multigroup comparisons, and the parameter settings were as follows: centWave for feature detection (Δ m/z = 15 ppm, minimum peak width = 10 s, and maximum peak width = 60 s); obiwarp settings for retention time correction (profStep = 0.5); and parameters for chromatogram alignment, including mzwid = 0.015, minfrac = 0.5, and bw = 5. The relative quantification of metabolite features was based on extracted ion chromatogram areas. Paired parametric t test and one-way ANOVA (post hoc Tukey test) were used to test the variation pattern of metabolite features between and across cell samples. The result outputs, including EICs, pairwise/multigroup cloud plot, multidimensional scaling plots, and principle components, were exported directly from XCMS Online. Generally, the numbers of total pairwise comparison features and significantly altered features (statistically defined as p value < 0.01, including both upregulated and downregulated features) were reported in this study.

4.2.5 MDM and neuronal culture assays

Human monocyte-derived macrophages (MDM) were isolated and then differentiated as described [227]. MDM were cultured in Dulbeccos Modified Eagle medium (Invitrogen) supplemented with 2 mM L-glutamine, 100 μg mL−1 streptomycin, 100 U mL−1 penicillin, and 2% fetal calf serum. Murine neurons were isolated from E16-E17 (embryonic) mouse whole brain tissues. Briefly, embryonic day 16 mice were harvested by cesarean section from anesthetized pregnant dams (C57BL/6 strain). The animal protocol was approved by the Animal Care and Use Committee of University of Nebraska Medical Center. Whole brain tissues were isolated and dissociated by 10% (v/v) trypsin (Life Technologies, Bethesda, MD) digestion and trituration with a fire-polished Pasteur pipette. Cell culture dishes were coated with 33 μg/mL poly-D-lysine. The cells were plated in neurobasal medium supplemented with B27, 300 μM glutamine, 25 μM mercaptoethanol, and streptomycin/amphotericin B (Life Technologies, Waltham, MA). Three days after plating, 50% of the medium was changed and subsequently the medium was changed every 6 days. Cells were maintained in the culture for 8–10 days for complete differentiation before any treatment.

4.2.6 Cell-based DTG measurements

MDM and neuron cells with different treatments were rinsed with phosphate-buffered saline (PBS) and extracted with acetonitrile:H2O:methanol (2:1:2, v/v/v) using freeze-thaw method as described elsewhere [270]. The samples were centrifuged at 16,000g at 4 °C for 15 min and the supernatant was directly injected into the triple-quad 6495 (Agilent Technologies, Santa Clara, CA) operated in multiple reaction monitoring mode (MRM), where the collision energies and product ions (MS2 or quantifier and qualifier ion transitions) were pre-optimized (quantifier ion 420 to 295 and qualifier ion 420–277). Cycle time was 150 ms for each transition. ESI source conditions were set as following: gas temperature 250 °C, gas flow 14 L/min, nebulizer 20 psi, sheath gas 250 °C, sheath gas flow 11 L/min, capillary voltage 3000 V, nozzle voltage 1500 V, and EMV 1000 V in ESI-positive mode. The analyses were performed on a Waters UPLC BEH Amide column (50 × 1

mm, 1.7 μm) (Waters Corporation, Milford. MA). The mobile phase was composed of A = water with 20 mM ammonium formate and 0.1% formic acid and B = acetonitrile with 0.1% formic acid. A linear gradient from 5% B (0–0.5 min) to 30% B (0.5– 5 min, maintaining for 2 min) was applied. Then, the gradient was set to the initial 5% B within the next 1 min. A 2-min reequilibration time was applied to the column for re-equilibration. The flow rate was 200 μL/min, and the sample injection volume was 2 μL.

4.2. 7 Reactive oxygen species (ROS) measurements

ROS were measured in neuron and MDM cells with the probe DCFDA (dichlorofluorescin diacetate, abcam, Cambridge, MA). Cells were seeded on black, clear-bottomed 96-well plates. After cells were pre-cultured with different treatments, the media were removed and the cells were washed with 1 × buffer (supplied with the kit). Cells were incubated for 45 min in 1× buffer containing 25 μM DCFDA at 37 °C. DCF production was measured by fluorescence spectroscopy with excitation wavelength at 485 nm and emission wavelength at 535 nm. In this study, the cells were treated with increasing concentrations of free DTG, nano-DTG, and various vehicle, positive, and negative controls to compare ROS generation and lactate dehydrogenase (LDH)-based cytotoxicity generated by such treatments. The highest DTG levels measured in the mouse brain is in the micromolar range so the highest dosing concentration used for ROS experiment was set to 500 μM in the dosing medium, which did not show significant cytotoxicity. TBHP (tert-butyl hydroperoxide; 10 μM) and PBS were used as the positive and negative controls, respectively. The vehicle control for nanoformulated DTG was composed of poloxamer micelles without the drug. The vehicle control for free DTG was composed of 43% ethanol, 5% cremophor, 20% propylene glycol (propane-1,2-diol), and 32% PBS (v/v). To further validate the protective effect of the P407 nanoformulation in mediating the oxidative stress, we conducted additional experiments to measure ROS formation in neurons and MDM cells treated with free and nanoformulated DTG with a series of dilutions from 10 to 100 μM of drug and then challenged with the positive control 10 μM TBHP

to induce further oxidative stress. Specifically, cells (both MDM and neurons) were treated for 2 h with various vehicle or drug concentrations. Then, cells were washed and new media was added, and after 24-h culture, cells were challenged with TBHP for 2 h, followed by fluorescence-based ROS measurements.

4.3 Results

4.3.1 Brain region-specific metabolomics after free and nanoformulated DTG injections

Following free and nanoformulated DTG mouse injections, global metabolomics were performed on five dissected brain subregions including the FC, VC, DC, H, and CR (Figure 4.1). The effects of free DTG on the brain metabolome were more pronounced within the FC and CR (Figure 4.2a). In free DTG treated mice, the FC and CR showed the most pronounced metabolite dysregulations with 130 and 73 features in comparison to 50, 58, and 61 for the VC, DC, and H. Each of the numbers listed are posted in comparison to controls. The dysregulated metabolites observed in the CR overlapped, in part, with those observed in the other four brain subregions. In contrast to the metabolite effects seen by free DTG, nanoformulated DTG-treated animals showed few dysregulated features. Interestingly, the number of dysregulated features had a narrower range from 33 to 17, which on average represents a third of the number in the free DTG treatment group. Furthermore, equivalent DTG drug concentrations were measured in all five brain regions in mice treated with either free or nanoformulated DTG, demonstrating the advantages of increased macrophage uptake and retention and apparent plasma drug half-life of the nanoparticle delivered DTG compared to free drug as a delivery system. Statistical significant differences in DTG concentrations were only observed in the H, where lower drug concentrations were measured in the nanoformulated drug-treated mice. However, the fold change (0.63) was valued as small and unlikely to affect the observed metabolite response differences (Figure 4.2b). Indeed, DTG nanoparticles are rapidly endocytosed by macrophages and release drug in a controlled manner in tissue target locations, which more likely reflects the differences seen.

Among the many dysregulated metabolites seen in brain subregions in the free DTG-treated group, the most affected were identified as energy-related pathways, including glycolysis and the tricarboxylic acid (TCA) cycle (Figure 4.3). Also, the dysregulation of nicotinamide adenine dinucleotide (NAD) and nicotinamide adenine dinucleotide phosphate (NADP), known cofactors in redox reactions, proved highly relevant due to linkages to oxidative stress related to xenobiotics and environmental pollutants affecting biological systems. The dysregulation of these was not observed between controls and DTG nanoparticles, which suggests negligible drug brain metabolic disruption when DTG was encased in nanoformulations.

4.3.2 DTG and oxidative stress

In addition to energy-related pathways, the most significant change in DTG-induced brain metabolism was in ascorbic acid and glutathione degradation. These changes are depicted in Figure. 4.4 for both free (a, b) and nanoformulated (c, d) DTG in each brain subregion. These values represent the ratio of the amount found in the controls divided by the amount found in the treated mice for ascorbic acid and GSH, as they are depleted with oxidative stress. Conversely, the values for threonate and GSSG represent the ratio of the amount found in the treated mice divided by the amount found in their corresponding controls. In these assays, higher ratios reflect greater degrees of oxidative stress seen as visual darker shades with oxidation, red for depletion of protecting metabolites (ascorbic acid and GSH) and green for the increase in oxidation

products (threonate and GSSG).

The most substantial changes in ascorbic acid levels were observed in the FC and CR in animals treated with free DTG. Similarly, increases in threonate further support the presence of oxidative stress (Figure. 4.4a). Analogous to ascorbic acid and threonate metabolic dysregulation in free DTG treatment groups, GSH and GSSG showed similar effects with the exception of increases in oxidative stress seen across each of the five brain regions (Figure. 4.4b). All changes found in free DTG groups are statistically significant (p value < 0.05) with the exception of ascorbic

acid levels observed in the H (Figure 4.6). In contrast to free DTG, nanoformulated DTG treated animals showed less ROS brain-associated metabolic dysregulation. In Figure. 4.4c, d, more limited changes were seen without statistical significance compared to controls. It should be noted that similar brain drug levels between free and nanoformulated drugs were seen across both formulations and as such cannot explain the experimental differences (Figure 4.2b). To investigate the metabolic source of the oxidative stress and the association with nanoformulation, a number of mechanistic laboratory experiments were performed for cross validation and extension.

4.3.3 Nanoparticle DTG encasement abrogates brain oxidative stress

In attempts to elucidate any neuroprotective mechanism underlying the DTG nanoformulations, we employed mouse embryonic neuron cells and human MDM for testing. Each was treated with free and nanoformulated DTG with the addition of their respective vehicle controls. ROS formation was measured orthogonally in neurons and MDM using fluorescence based commercial kits (DCFDA, Figure 4.5a, b, respectively) and administered at 100 and 500 μM. Values are reported as fold changes compared to respective vehicle controls. Neurons treated with free but not nanoformulated DTG showed increases in ROS of up to 1.5 times of control. In contrast for MDM, free and nanoformulated DTG induced more limited ROS effects altering metabolite concentrations 0.8 and 1.2 times, respectively, when given at 100 μM. The abilities of nanoparticles to modestly increase ROS suggested that P407 by itself is not an antioxidant but that the protective mechanism could be more physically linked. ROS levels in free DTG cell cultures were higher than those in the vehicle controls as aligned with the notion that DTG can itself induce oxidative stress. More interestingly, comparisons between free and nanoformulated DTG supported the hypothesis that nanoformulation can reduce oxidative stress and protect neurons (Figure 4.7a–d). In attempts to sort out these differences and to better elucidate the effects of free and nanoformulated DTG and relevant drug delivery vehicles on ROS induction, we performed dose-response ROS induction following oxidative stress induced by TBHP. In these experiments, neuron and MDM cells were

treated with both free and nanoformulated DTG (concentration between 10 and 100 μM) followed by the addition of 10 μM TBHP as an oxidative stress inducer. As shown in Fig. 5c, a clear ROS response was seen in neurons treated with either free or nanoformulated DTG, while no effect was seen for vehicle controls. Most importantly, for MDM (Figure. 4.5d), free DTG challenged with TBHP induced ROS formation in a dose-response at higher concentrations (60 to 100 μM), reflective of what was observed previously in neurons. In contrast, addition of nanoformulated DTG to the cultures attenuated the TBHP response signaling control of ROS or the ability to buffer such effects by the nanoformulations. These latter data provide a mechanism for how the nanoformulation could control ROS production in specific brain regions. Finally, we measured cellular uptake of free and nanoformulated DTG at 1, 10, and 100 μM (Figure 4.5e, f) in attempts to better uncover mechanisms. As shown in Figure 4.5e, the concentrations of nanoformulated DTG in neurons were almost one order of magnitude higher than those in the free DTG drug. However, for MDM, the concentration was similar between two forms of DTG treatment (Figure 4. 5f), which could be explained by different drug uptake mechanisms, biotransformations, and cell metabolic capacity between both cell types. However, considering the fact that DTG concentrations of nano-DTG-treated cells are one order of magnitude higher than those of free DTG-treated cells at the same dosing concentration (Figure 4. 5a, b), the nanoformulations shows its protective effect in modulating ROS level (e.g., fold change of 4 at 100 μM for free DTG and fold change of 1.2 at 10 μM for nano-DTG). As for MDM cells (Fig. 4.5f), the free DTG drug challenged with TBHP induced ROS formation with a clear concentration-response at higher concentrations (60 to 100 μM), similar to neurons. This explains, in part, the unexpected increase in ROS production during initial TBHP challenge in neurons (Figure 4.5c).

4.4 Discussion

The possible link between ART and neurotoxicities has only been postulated. Here, we investigated for the first time the effect of DTG on global metabolome during administration of

free and nanoformulated drugs. The results showed that while free DTG delivered at high doses can affect the brain metabolism for oxidative stress, the effects can be curtailed by how the drug is formulated. Altogether, our results affirm that if and when DTG is used in part of a LASER ART regimen, it can be administered safely. It is acknowledged and despite restricted viral growth by cART, up to 60% of HIV-1- infected patients show HAND-related cognitive and behavioral abnormalities induced by comorbid infectious, cancerous, metabolic, and neuropsychiatric events [175]. ARVs themselves are potential contributors and most can elicit varying degrees of neurotoxic reactions. Each of these "purported" adverse effects is independent of drug class that includes nucleoside reverse transcriptase inhibitors (NRTIs, e.g., abacavir and lamivudine), non-NRTIs (e.g., efavirenz), entry inhibitors (e.g., maraviroc), inhibitors of the viral protease (e.g., atazanavir), and integrase inhibitors (INSTI, e.g., DTG). Notwithstanding, each of the drugs has revolutionized patient care and has improved longevity and disease morbidities considerably, and to the degree, HIV-1/AIDS is now a treatable chronic, managed disease. DTG, in particular, is used commonly in both first- and second-line therapies that have been projected by 2019 to account for 37% of the adult first-line NNRTI/INSTI market, representing 3.8 million patients [272]. Compared to NRTIs, DTG is durable and can cross the BBB allowing it to easily achieve therapeutic brain concentrations [273]. However, side effects of DTG are reported and include insomnia and headache as well as more significant allergic reactions and abnormal liver function in dual hepatitis virus-infected people [259]. Low concentrations of DTG can trigger suicidal death in erythrocytes characterized by cell shrinkage and membrane scrambling with phosphatidylserine translocation to the erythrocyte surface [274]. Putative neuropsychiatric effects were reported in adult patients who received DTG, raltegravir, and elvitegravir, suggesting specific toxicities linked to integrase strand transfer inhibitors [253, 256, 275-279]. Nonetheless, others have debunked such results with a sole substantiated DTG metabolic effect being a rise in serum creatinine due to tubular secretion inhibitions [280, 281].

Oxidative stress plays a principal role in the pathogenesis of neurodegenerative disorders including Alzheimer's disease, Parkinson's disease, amyotrophic lateral sclerosis, and HIV-1 associated dementia [282]. A spectrum of xenobiotics, mitochondrial dysfunction, accumulation of aberrant misfolded proteins, inflammation, and defects in protein clearance are all known to accumulate ROS. Xenobiotics can be oxidized to free radicals by cytochrome P450 and generate ROS following the quenching of the radicals. DTG has been shown to be oxidized by CYP3A4, even though the major metabolic reaction was glucuronidation of DTG principally by metabolic reaction was glucuronidation of DTG principally (in humans) [283]. Dysregulation of glycolysis, TCA cycle, and redox cofactors could indicate a need of cells engaging in neutralizing ROS processes. Another ART drug, efavirenz, was also reported to alter mitochondrial respiration and enhance ROS generation, resulting in CNS damage [255, 284-286]. Therefore, the need for novel therapeutic strategies that attenuate neuroinflammation and protect neurons against oxidative stress is immediate for DTG. Despite the higher DTG dose used in this study over those administered to HIV-1 infected patients the drug concentrations in brain were equivalent (Figure 4.2b). Of interest no significant oxidative stress increase was observed during nanoformulated DTG treatment compared to free DTG-injected mice. Thus, it is speculated that P407 nanoformulation could play a vital role in mediating ROS formation. Several other non-ionic surfactants including polyethylene glycol (PEG) and poloxamer 188 have shown protective effects from oxidative damage in both laboratory and animal models of human disease [287-290]. For example, using a guinea pig spinal cord injury model, it has been shown that PEG could significantly decrease injury-induced ROS elevation and lipid peroxidation levels [286]. A further investigation showed that PEG is not an effective free radical scavenger nor does it have the ability to suppress xanthine oxidase, a key enzyme in generating superoxide, but can significantly accelerate and enhance the healing process to restore membrane integrity [289].

Our in vitro study suggested that surfactant poloxamer-407 could decrease the oxidative stress and cell damage. Thus, it is very likely that P407 has a beneficial effect on the drug efficacy of DTG treatment besides its role as a drug delivery system. This protective effect of non-ionic surfactant nanoformulations could have significant implications on future drug discovery, given the fact that oxidative stress is one of the most common side effects of many therapeutic drugs. Induction of oxidative stress can lead to drug failure in clinical trials or phase-out in the market in later use. Though oral ingestion of antioxidants could deem effective in counteracting such toxicity, it is not an ideal therapeutic solution due to their side effects or interactions with other medications or supplements [291-293]. Interestingly, the nanoformulated non-ionic surfactant tested in this study did not show any obvious toxicity in affecting brain metabolism. Previous studies have also found that nanoparticles can penetrate the BBB possibly via receptor-mediated endocytosis in brain capillary endothelial cells [294]. This suggests that another advantage of nanoformulations in antagonizing oxidative stress is the colocalization of nanoparticles and drug during distribution, resulting in possible in situ restoration of normal physiological conditions. Further investigation on the optimization of the material type, size, and formulation as well as its potential application for generic drug modification is needed. It is worth noting that oxidative stress and malformations in embryonic developmental including those linked to neural tube defects could occur [295-299]. Future works are certainly required to see if such relationships could occur between DTG and maternal fetal abnormalities.

In conclusion, we examined DTG brain metabolic activities using mass spectrometry-based metabolite profiling and observed significant dysregulation in energy and oxidative stress pathways; most notably, glutathione and ascorbic acid were depleted. This effect was significantly attenuated when DTG was administered as a nanoformulation. This data provides a possible pathway for the advantages of nanoformulations or other relevant therapeutic drug delivery systems to preclude systemic toxic reactions and most notably those that involve the nervous system.

4.5 Figures

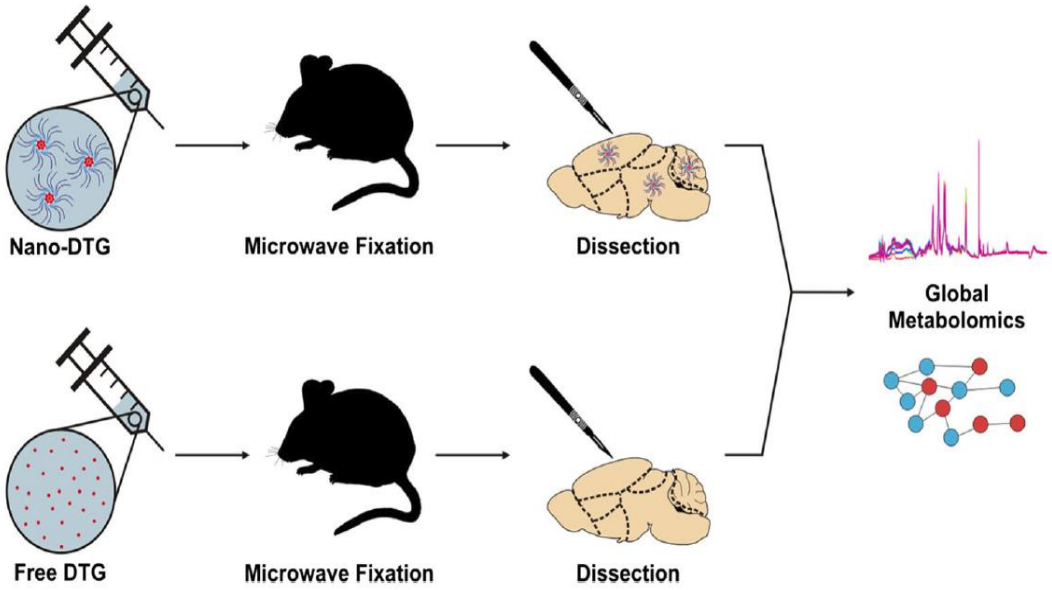

Figure 4.1 Workflow of mouse brain global metabolomics study. Free and nanoformulated DTG with drug administered every other day for three total injections or by a single bolus of 45 mg/kg, respectively. All mice were sacrificed after 1 week following treatment. After heat fixation by microwave irradiation euthanasia, brain hemispheres were dissected into subregions including the FC, the VC, the DC, the H, and the CR. Brain subregions were extracted for untargeted LC-MS metabolic profiling (mice specimens = 5, total 50 sub-samples)

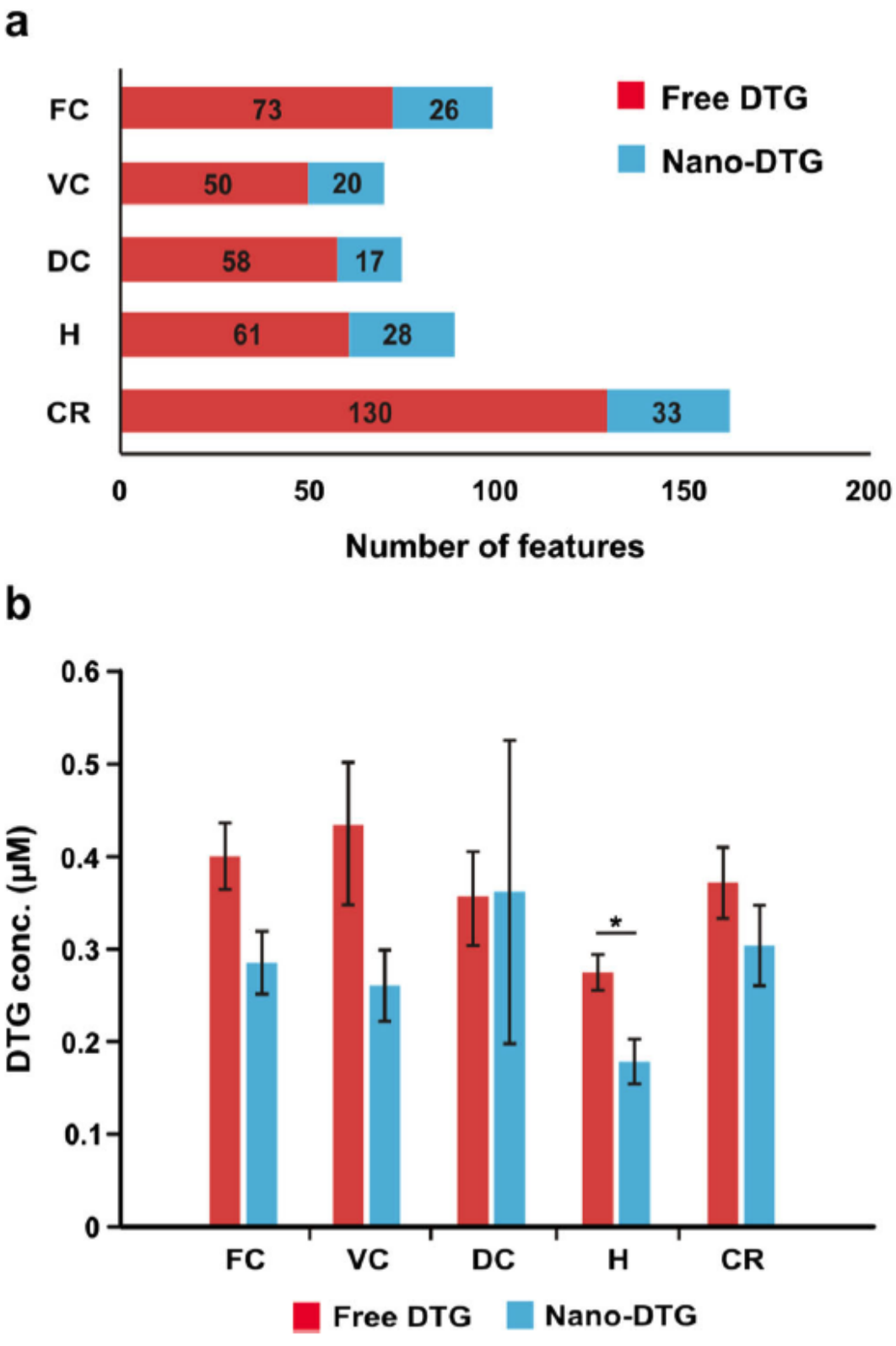
a
FC
VC
DC
H
CR
73
26
50
20
58
17
61
28
130
33
Free DTG
Nano-DTG
0
50
100
150
200
Number of features
b
DTG conc. (μM)
0.6
0.5
0.4
0.3
0.2
0.1
0
*
FC
VC
DC
H
CR
Free DTG
Nano-DTG

Figure 4.2 Total number of dysregulated features among the FC, VC, DC, H, and CR. All the features were manually filtered. b DTG concentration in brain regions for free and nanoformulated DTG (nano-DTG) (error represents SEM and "*" represents p value < 0.05). For each experiment, a minimum of four experimental replicates were used

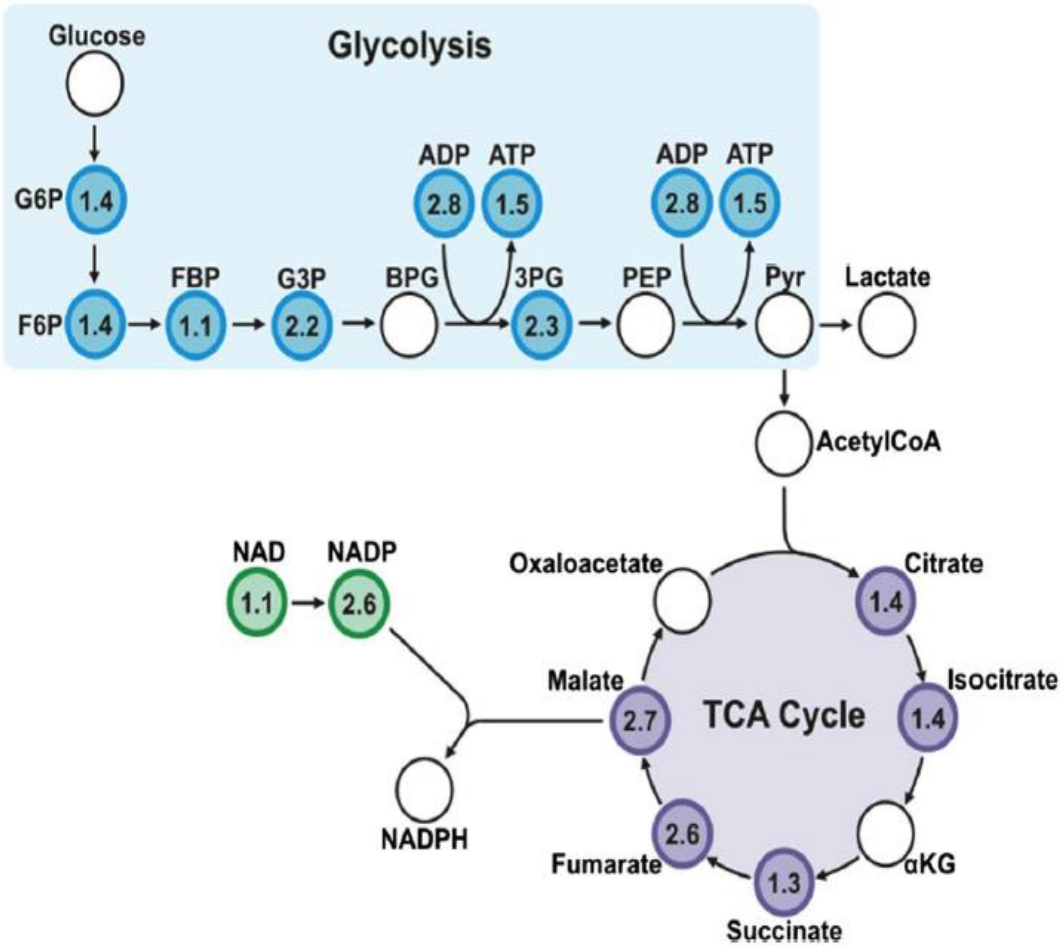

Figure 4.3 Glycolysis/TCA pathways and redox partners with identified metabolites. Fold change between free DTG and the corresponding control. Those values in circles had a p value < 0.05. All the metabolites were identified using METLIN MS/MS fragment match and confirmed with their pure standards

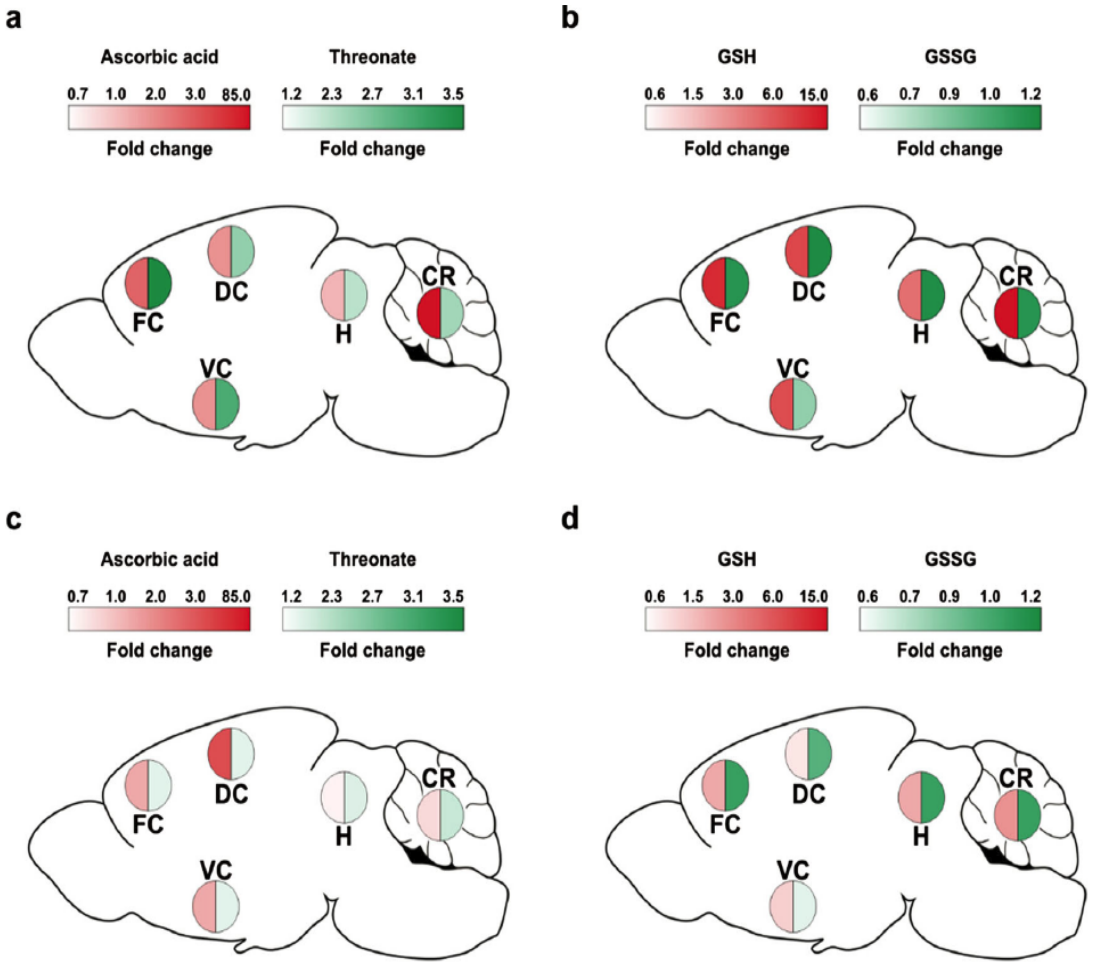

Figure 4.4-Fold change of metabolites indicative of oxidative stress in five different brain regions. Both free DTG and nanoformulated DTG treatments with their corresponding controls. Ascorbic acid is oxidized to threonate and GSH is oxidized to GSSG. The color scheme was selected to show oxidation with darker shades of red for ascorbic acid and GSH and green for threonate and GSSG. a Ascorbic acid and threonate fold changes for free DTG treatment. b GSH and GSSG fold changes for free DTG treatment. c Ascorbic acid and threonate fold changes for nanoformulated DTG treatment. d GSH and GSSG fold changes for nanoformulated DTG treatment (n = 10 samples from 5 mice). All fold changes in a and b except for H in a have p values < 0.05. None were found to be statistically significant in c and d. The experiments listed represent a minimum of four replicates for each group

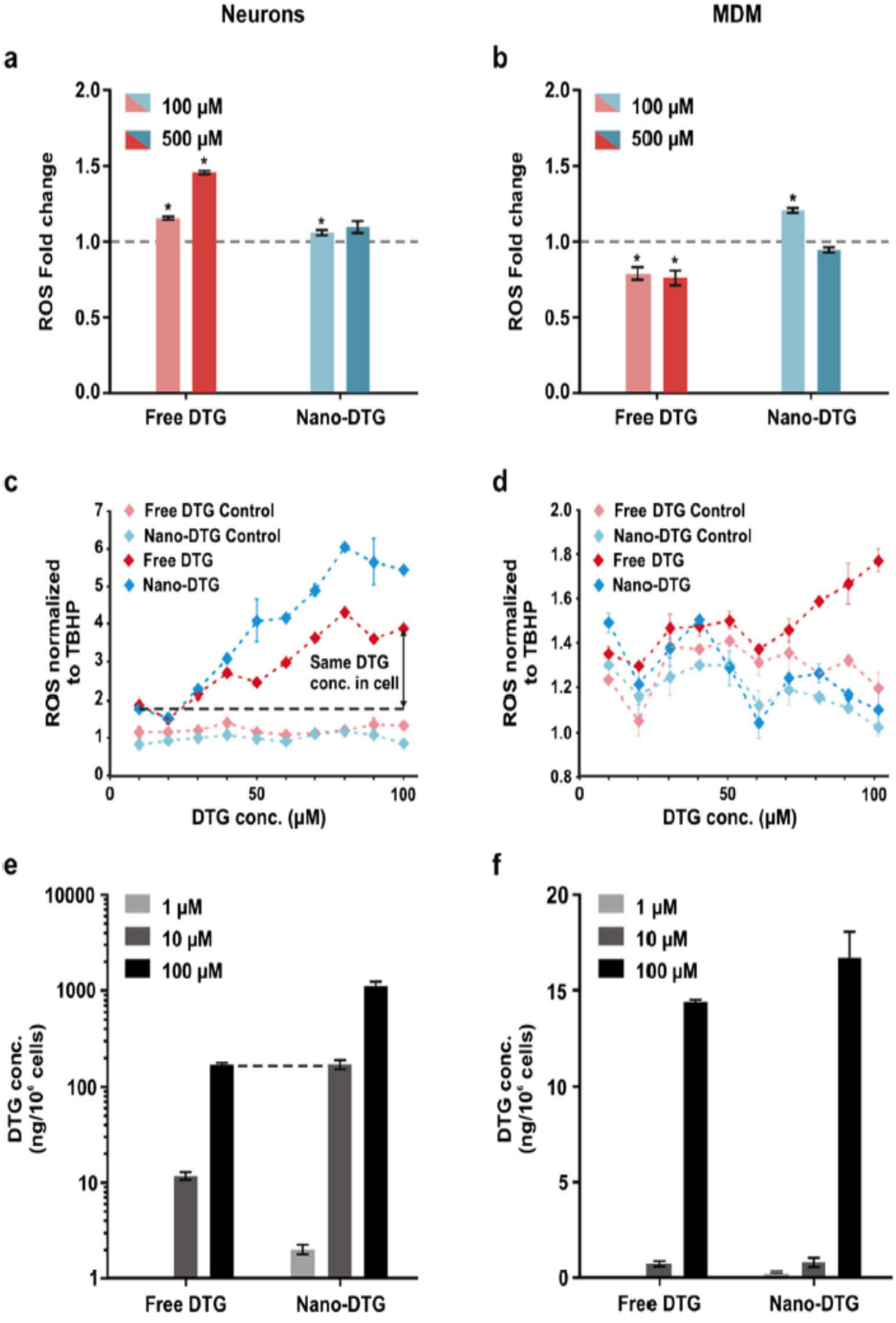
Neurons
MDM
a
b
ROS Fold change
100 µM
500 µM
Free DTG
Nano-DTG
c
d
ROS normalized to TBHP
Free DTG Control
Nano-DTG Control
Free DTG
Nano-DTG
Same DTG conc. in cell
DTG conc. (µM)
e
f
DTG conc. (ng/10⁶ cells)
1 µM
10 µM
100 µM

Figure 4.5 ROS formation and drug uptake of free and nanoformulated DTG in neurons and MDM cultures. a, b ROS fold change of neurons and MDM relative to their respective controls, respectively (error represent SEMand "*" represents p value < 0.01). c, d ROS levels after TBHP challenge in the neurons and MDM treated with free DTG, nanoformulated DTG, and their respective vehicle controls with a series of dilution from 10 to 100 μM. The data was normalized with TBHP-positive control (10 μM). e, f DTG concentration in neurons and MDM respectively treated with free DTG and nanoformulated DTG. The DTG concentration in neurons treated with 100 μM free DTG equals the DTG concentration treated with 10 μM nanoformulated DTG (dotted line, 168 ng/106 cells). This comparison by cellular uptake is indicated by the dotted line in c

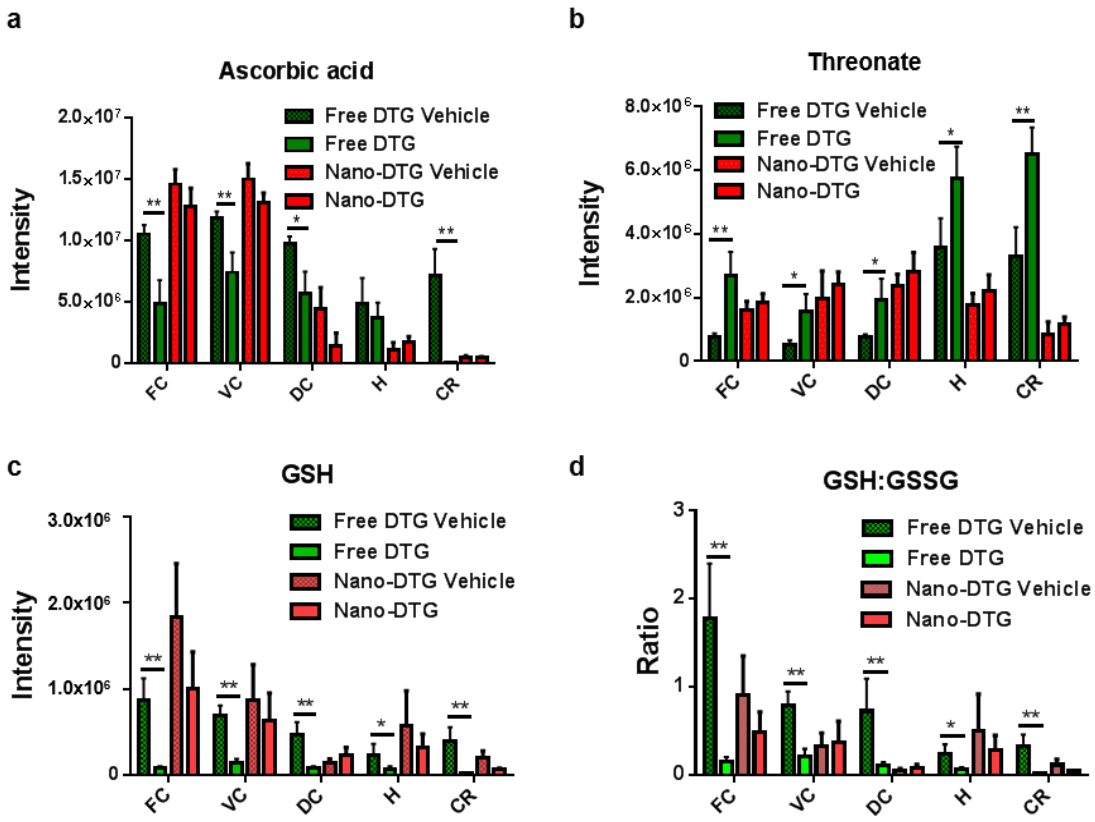

Figure 4.6. **Relative abundance of oxidative stress biomarkers**. **(a)** ascorbic acid; **(b)** threonate; **(c)** glutathione (GSH); **(d)** GSH/GSSG ratio in five dissected regions, frontal cortex, ventral cortex, dorsal cortex, hippocampus and cerebellum (n=10 samples from 5 mice) from mice treated with free DTG and Nano-DTG compared with their respective controls. All data corresponds to global metabolomics analysis. Error bars represents standard error of the mean. "*" and "**" represents *p values* <0.05, and <0.01; respectively.

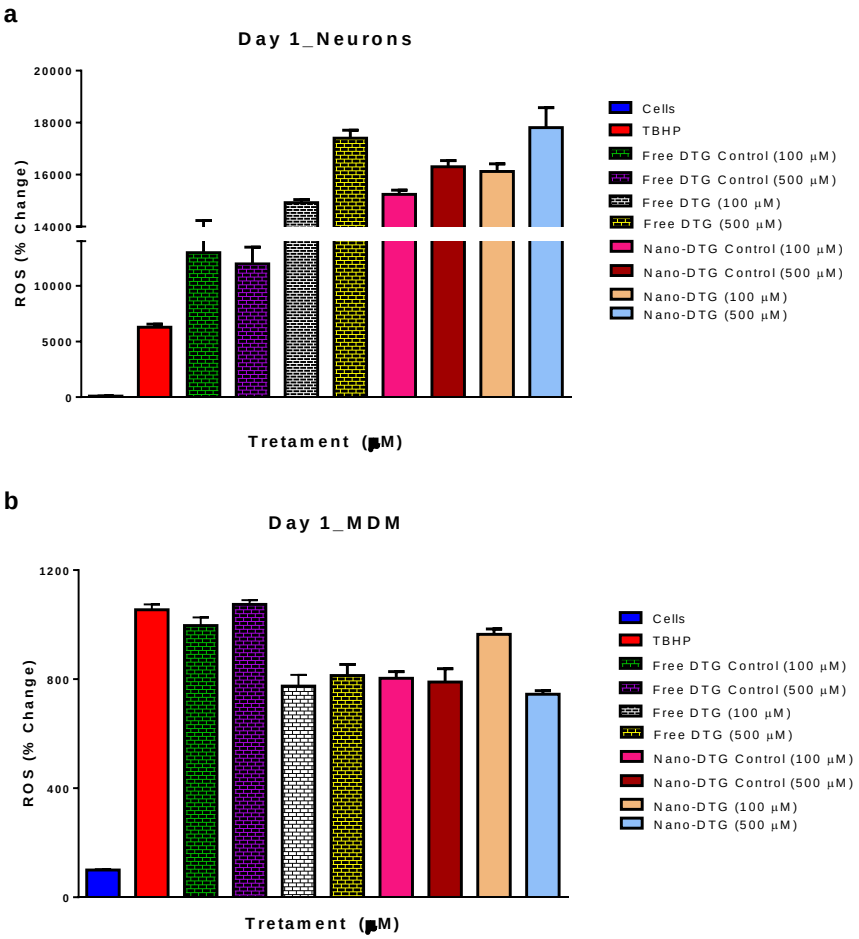

Figure 4.7. Free DTG and nanoformualted DTG (Nano-DTG) reactive oxygen species (ROS) formation in murine neurons and human monocyte derived macrophage (MDM) cells 24 hours post treatment. (a) Neurons and **(b)** MDM treated with 10 µM TBHP (positive control), free DTG (100 and 500 µM), Nano-DTG (100 and 500 µM), and their respective vehicle controls. Error bars represent standard error of the mean (n=6).

CHAPTER 5

Summary and Conclusion, Limitations, and Future Directions

5.1 Summary and conclusions

The successful development of combination antiretroviral therapy for the treatment of HIV-1 undoubtably changed the course of human history, as millions of infected people can now anticipate a prolonged lifespan instead of a certain and painful death. However, the persistence of virus and the continued strain of the pandemic on global healthcare has resulted in HIV-1 research to develop novel strategies to improve upon current antiretroviral therapy. Improvements in pharmacodynamic and pharmacokinetic profiles have shown remarkable promise in increasing drug adherence, reducing secondary toxicities, and preventing new infections. Our lab has shown that the enhancement of the hydrophobicity of current ARVs via nanocrystals incased in biodegradable polymers allows for the establishment of drug depots within monocyte-macrophages, significantly prolonging drug half-life. But experimentation of such nanoformulations within animal models has proved cumbersome, with biodistribution measurements extending weeks or even months proving particularly tedious.

The first study (chapters 2 and 3) assessed the use of our theranostic nanoparticle platform and its ability to accumulate within monocyte-macrophages as well as reticuloendothelial tissues. Theranostic nanotechnology has allowed the rapid screening of drug tissue biodistribution and pharmacokinetics which allows for pharmacodynamic improvements. Our theranostic nanoparticle platform was developed with careful consideration of components that allowed assessment of particle presence as well as component concentration within cells and tissues *in vitro*, *in vivo*, and *ex vivo*. Encasement of hydrophobic ARVs and imaging contrast agents within a single nanoformulation produced theranostic nanoparticles with a multitude of modalities, allowing for validations of the multiple measurements performed. Incorporation of Eu^{3+} into the nanoparticles allowed for confirmation of particle presence within cells and tissues via fluorescence confocal imaging. Cobalt ferrite provided a paramagnetic material necessary for T_2 contrast in MR imaging. Altogether, our theranostic nanoparticle platform allowed for real time assessment of ARV

biodistribution and activity that would otherwise not be possible with traditional plasma post-mortem tissue concentration analysis. Upon synthesis, EuCF-DTG nanoparticles showed remarkably consistent size, size, magnetism, fluorescence, and proper ARV drug loading as well as drug release in PBS. Administration of EuCF-DTG to *in vitro* macrophage cell culture resulted in consistent cellular uptake of nanoparticles, with FA targeted EuCF-DTG showing significantly higher uptake. Uptake of EuCF-DTG nanoparticles did not affect cellular viability in these studies. Furthermore, confocal microscopy of *in vitro* macrophages displayed EuCF-DTG nanoparticles localizing within subcellular components, with a high proportion of nanoparticles residing within recycling endosomes. Perhaps most importantly, EuCF-DTG nanoparticles exhibited antiretroviral activity upon administration to HIV-1 infected *in vitro* cellular cultures, confirming the therapeutic effects of our theranostic nanoparticle platform. Real time *in vivo* MR imaging of rats administered EuCF-DTG nanoparticles both via IV and IM injection confirmed nanoparticle presence within reticuloendothelial tissues at 2, 5, and 10 days post-injection. Quantification of iron concentrations within liver and spleen was performed by MRI T_2 mapping with IV injected animals exhibiting a two-fold increase in iron compared to IM injected animals. Post-mortem tissue concentrations of cobalt and DTG were measured by ICP-MS and UPLC- MS/MS, respectively. DTG and cobalt levels following IM or IV injection of nanoparticles showed coordinate tissue and plasm drug and cobalt levels. Furthermore, MRI iron concentrations performed *in vivo* were validated by *ex vivo* concentrations of cobalt and DTG. Overall, such data suggests that the amount of drug that accumulates in tissues can be estimated in real time by *in vivo* MRI by using the known signal-to-drug ratio of EuCF-DTG nanoparticles. Post-mortem tissue confocal microscopy confirmed the presence of EuCF-DTG nanoparticle within recycling endosomal compartments in macrophages, mirroring results found in *in vitro* confocal microscopy studies. Additional biodistribution studies were performed by EuCF-DTG administration to rhesus macaques. Highest concentrations of DTG and cobalt were found in the liver and kidneys, with detectable levels observed in the spleen and

lymph nodes. These results suggest that EuCF-DTG nanoparticles are taken up by macrophages in reticuloendothelial tissues in rhesus macaques, similar to biodistribution studies performed in rats.

Our second study (chapter 4) assessed the possibility that native ARV drug administration could cause neurotoxicity and whether administration of ARV drug as a nanoformulation could attenuate any observable neurotoxic effect. While ART restricts HIV-1 replication and subsequently improves the quality and longevity of life for infected people, such treatment can lead to adverse clinical outcomes such as drug resistance and systemic adverse events. Both could be affected by long-acting slow effect release ART. Indeed, maintenance of sustained plasma drug levels, for weeks or months, after a single-high level dosing, could improve regimen adherence but additionally affect systemic toxicities, including those of the CNS. To address this a potent and durable HIV-1 integrase inhibitor used effectively in combination ART was tested. Rodents were administered parenteral 45-mg/kg doses. DTG-associated changes in CNS homeostasis were assessed by measuring brain metabolic activities. After antiretroviral treatment, brain subregions were dissected and screened by mass spectrometry-based metabolomics. Metabolic drug-related dysregulation of energy and oxidative stress were readily observed within the cerebellum and frontal cortex following native drug administrations. Each was associated with alterations in neural homeostasis and depleted canonical oxidation protection pools that included glutathione and ascorbic acid. Surprisingly, the oxidative stress-related metabolites were completely attenuated when DTG was administered as nanoformulations. These data demonstrate the importance of formulation design in control of DTG or perhaps other antiretroviral drug-associated CNS events.

Overall, the data presented in this thesis will have significant impact on research striving for both the care for HIV-1 patients and the eradication of the virus. A theranostic nanoparticle platform was designed specifically for HIV-1 therapeutic innovation, allowing for improvements in pharmacokinetic and biodistribution profiles of LASER ART technology within a relatively short time frame. Such theranostic technology, to the authors knowledge, is the first such platform

that has been applied for HIV-1 research. Furthermore, investigation of possible off target neurological effects of relatively new ARV medications allows for improvements in patient care. The attenuation of the observed changes in the neuro-metabolome by nanoformulated ARV is representative of such improvements. Such nanoformulated ARV not only has a longer half-life and improved biodistribution, but it's slower systemic release can possibly prevent neurological side-effects of the drug. Both projects have potential for dramatic influence on future directions of HIV research.

5.2 Limitations

While the HIV-1 theranostic technology that was developed and experimentally tested ultimately met our goals that are outlined within this thesis, several limitations of such nanotechnology exist. Future development and utilization of HIV-1 theranostic nanotechnology must take note of such limitations and make efforts to overcome them.

A major limitation of our EuCF-DTG theranostic nanoparticle platform was that of drug loading. Indeed, the ability to load adequate amounts of drug into a nanoscale system while still containing the necessary contrast agents and fluorescent components is particularly challenging. EuCF-DTG nanoparticles exhibited a drug loading percentage of ~6.2% weight/weight; while such concentrations were adequate to exhibit antiretroviral activity *in vitro*, it is unlikely that such drug levels would have much of a therapeutic effect on HIV-1 replication *in vivo*. Specifically, biodistribution studies of EuCF-DTG nanoparticles performed on SIV-1 infected rhesus macaques confirmed this issue. While the presence of the nanoparticle component cobalt and the ARV DTG were confirmed within the plasma and multiple tissue sites, SIV-1 viremia within these same tissues did not show any differences between pre and post injection of EuCF-DTG nanoparticles. Such data exhibits that EuCF-DTG being delivered to tissue sites of viral replication and that DTG is being released, but that DTG levels are not adequate to reduce SIV-1 viremia. Diagnostic limitations of our EuCF-DTG theranostic nanoparticle platform was the use of MRI as the major

imaging modality. While MRI is a powerful diagnostic tool with superior spatial resolution, it has difficulty imaging particular tissues that are relevant to HIV-1 pathology. Specifically, T_2 weighted MR images of tissues or organs containing air, such as the lungs or gastrointestinal tract, cannot be performed to very low signal-to-noise ratios in such areas. This is a major limitation due to the gut associated lymphoid tract being a significant HIV-1 reservoir, in which theranostic nanoparticle deliverance and subsequent MR imaging would be beneficial. Furthermore, MRI has difficulty differentiating small lymphoid tissues, such as lymph nodes, from the surrounding tissues. The inability to image and quantify theranostic nanoparticle concentrations within such tissues is a major limitation.

Metabolomic analysis of the brains of native DTG and nanoformulated DTG administered mice are limited as it is difficult to ascertain whether metabolic changes in redox metabolites is truly indicative of HIV-1 associated neurocognitive disorders. Indeed, while the changes that were exhibited can be classified as neurotoxic, alterations in neuronal homeostasis and depletions of canonical oxidation protection pools might not result in the manifestation of neuropsychiatric events. This is characteristic of the majority of psychiatric or neurological studies that utilize animal models; presentation of adverse behaviors or psychiatric abnormalities is often nuanced and requires complex questioning between the patient and clinician. Such psychiatric evaluation is not possible in animals. Deviation from normal baseline behavior, or abnormalities in post-mortem tissue analysis in comparison to control animals are the only way to establish possible adverse neuropsychiatric events. The animals utilized in our second study (chapter 4) did not display any abnormal behaviors during their administration of native or nanoformulated DTG.

5.3 Future Directions

Potential future applications of HIV-1 theranostic technology are both diverse and exciting. Successful establishment of a theranostic nanoparticle platform allows for rapid assessment of biodistribution and pharmacokinetics, allowing for newer and more advanced drug delivery and

targeting schemes for HIV-1 eradication to be evaluated more efficiently. Experimentation that would take months or years with traditional pharmacokinetic evaluations can be performed within weeks using a theranostic platform, allowing more time and resources to be put towards more innovative nanotechnological developments. Additionally, further refinement of theranostic nanoparticles is a future possibility. Addition of a radionucleotide into the nanoparticle system allows for another imaging modality; such a theranostic platform would allow for MRI, fluorescence, and PET/SPECT imaging. Radio-imaging of nanoparticles allows for biodistribution analysis within tissues that are not possible with MRI. Alterations in nanoparticle components and size could lead to specific targeting of other HIV-1 reservoirs, such as the brain or lymphoid systems. Furthermore, magnetic movement of magnetically sensitive nanoparticles into areas of interest via external magnetic gradients could have significant potential in drug delivery technology, both in HIV-1 and other diseases. All future directions give optimism to the eventual eradication of HIV-1 from society.

REFERENCES

1. Maartens, G., C. Celum, and S.R. Lewin, *HIV infection: epidemiology, pathogenesis, treatment, and prevention.* Lancet, 2014. **384**(9939): p. 258-71.
2. Bezabhe, W.M., et al., *Barriers and facilitators of adherence to antiretroviral drug therapy and retention in care among adult HIV-positive patients: a qualitative study from Ethiopia.* PLoS One, 2014. **9**(5): p. e97353.
3. Fujita, M., *[Study of molecular function of proteins in human immunodeficiency virus].* Yakugaku Zasshi, 2013. **133**(10): p. 1103-11.
4. Sprague, C. and S.M. Brown, *Local and Global HIV Aging Demographics and Research.* Interdiscip Top Gerontol Geriatr, 2017. **42**: p. 1-10.
5. Furman, P.A., et al., *Phosphorylation of 3'-azido-3'-deoxythymidine and selective interaction of the 5'-triphosphate with human immunodeficiency virus reverse transcriptase.* Proc Natl Acad Sci U S A, 1986. **83**(21): p. 8333-7.
6. St Clair, M.H., et al., *3'-Azido-3'-deoxythymidine triphosphate as an inhibitor and substrate of purified human immunodeficiency virus reverse transcriptase.* Antimicrob Agents Chemother, 1987. **31**(12): p. 1972-7.
7. Meeker, R.B., E. Asahchop, and C. Power, *The brain and HAART: collaborative and combative connections.* Curr Opin HIV AIDS, 2014. **9**(6): p. 579-84.
8. Pau, A.K. and J.M. George, *Antiretroviral therapy: current drugs.* Infect Dis Clin North Am, 2014. **28**(3): p. 371-402.
9. Weiss, R.A., et al., *Variable and conserved neutralization antigens of human immunodeficiency virus.* Nature, 1986. **324**(6097): p. 572-5.
10. Gelderblom, H.R., M. Ozel, and G. Pauli, *Morphogenesis and morphology of HIV. Structure-function relations.* Arch Virol, 1989. **106**(1-2): p. 1-13.
11. Dahabieh, M.S., E. Battivelli, and E. Verdin, *Understanding HIV latency: the road to an HIV cure.* Annu Rev Med, 2015. **66**: p. 407-21.
12. Lima, R.G., et al., *Interaction of macrophages with apoptotic cells enhances HIV Type 1 replication through PGE2, PAF, and vitronectin receptor.* AIDS Res Hum Retroviruses, 2006. **22**(8): p. 763-769.
13. Porcheray, F., et al., *Macrophage activation and human immunodeficiency virus infection: HIV replication directs macrophages towards a pro-inflammatory phenotype while previous activation modulates macrophage susceptibility to infection and viral production.* Virology, 2006. **349**(1): p. 112-120.
14. Burton, D.R. and R.A. Weiss, *AIDS/HIV. A boost for HIV vaccine design.* Science, 2010. **329**(5993): p. 770-3.
15. Dalgleish, A.G., et al., *The CD4 (T4) antigen is an essential component of the receptor for the AIDS retrovirus.* Nature, 1984. **312**(5996): p. 763-767.
16. Klatzmann, D., et al., *T-lymphocyte T4 molecule behaves as the receptor for human retrovirus LAV.* Nature, 1984. **312**(5996): p. 767-8.
17. Cohn, L.B., et al., *HIV-1 integration landscape during latent and active infection.* Cell, 2015. **160**(3): p. 420-32.
18. Maldarelli, F., et al., *HIV latency. Specific HIV integration sites are linked to clonal expansion and persistence of infected cells.* Science, 2014. **345**(6193): p. 179-83.

19. Farnet, C.M. and F.D. Bushman, *HIV cDNA integration: molecular biology and inhibitor development.* Aids, 1996. **10 Suppl A**: p. S3-11.
20. Devadas, K., et al., *Mechanisms for macrophage-mediated HIV-1 induction.* J Immunol, 2004. **173**(11): p. 6735-6744.
21. Cuevas, J.M., et al., *Extremely High Mutation Rate of HIV-1 In Vivo.* PLoS Biol, 2015. **13**(9): p. e1002251.
22. Sierra, S., B. Kupfer, and R. Kaiser, *Basics of the virology of HIV-1 and its replication.* J Clin Virol, 2005. **34**(4): p. 233-44.
23. Freed, E.O., *HIV-1 assembly, release and maturation.* Nat Rev Microbiol, 2015. **13**(8): p. 484-96.
24. Shaw, G.M. and E. Hunter, *HIV transmission.* Cold Spring Harb Perspect Med, 2012. **2**(11).
25. Dickson, D.W., *Multinucleated giant cells in acquired immunodeficiency syndrome encephalopathy. Origin from endogenous microglia?* Arch Pathol Lab Med, 1986. **110**(10): p. 967-968.
26. Sharer, L.R., E.S. Cho, and L.G. Epstein, *Multinucleated giant cells and HTLV-III in AIDS encephalopathy.* Hum Pathol, 1985. **16**(8): p. 760-760.
27. Jiang, H., et al., *Determinants of progression to AIDS and death following HIV diagnosis: a retrospective cohort study in Wuhan, China.* PLoS One, 2013. **8**(12): p. e83078.
28. Fauci, A.S., *Multifactorial nature of human immunodeficiency virus disease: implications for therapy.* Science, 1993. **262**(5136): p. 1011-8.
29. Haase, A.T., *Population biology of HIV-1 infection: viral and CD4+ T cell demographics and dynamics in lymphatic tissues.* Annu Rev Immunol, 1999. **17**: p. 625-56.
30. Pantaleo, G. and A.S. Fauci, *Tracking HIV during disease progression.* Curr Opin Immunol, 1994. **6**(4): p. 600-4.
31. Schmitz, J.E., et al., *Control of viremia in simian immunodeficiency virus infection by CD8+ lymphocytes.* Science, 1999. **283**(5403): p. 857-60.
32. Haase, A.T., *Perils at mucosal front lines for HIV and SIV and their hosts.* Nat Rev Immunol, 2005. **5**(10): p. 783-92.
33. Pandrea, I., et al., *Into the wild: simian immunodeficiency virus (SIV) infection in natural hosts.* Trends Immunol, 2008. **29**(9): p. 419-28.
34. Galati, D. and M. Bocchino, *New insights on the perturbations of T cell cycle during HIV infection.* Curr Med Chem, 2007. **14**(18): p. 1920-4.
35. Connor, R.I., et al., *Increased viral burden and cytopathicity correlate temporally with CD4+ T-lymphocyte decline and clinical progression in human immunodeficiency virus type 1-infected individuals.* J Virol, 1993. **67**(4): p. 1772-7.
36. Fischl, M.A., et al., *Zalcitabine compared with zidovudine in patients with advanced HIV-1 infection who received previous zidovudine therapy.* Ann Intern Med, 1993. **118**(10): p. 762-9.
37. Lundgren, J.D., et al., *Comparison of long-term prognosis of patients with AIDS treated and not treated with zidovudine. AIDS in Europe Study Group.* Jama, 1994. **271**(14): p. 1088-92.
38. Hammer, S.M., et al., *A trial comparing nucleoside monotherapy with combination therapy in HIV-infected adults with CD4 cell counts from 200 to 500 per cubic millimeter. AIDS Clinical Trials Group Study 175 Study Team.* N Engl J Med, 1996. **335**(15): p. 1081-90.
39. Vella, S., et al., *The history of antiretroviral therapy and of its implementation in resource-limited areas of the world.* Aids, 2012. **26**(10): p. 1231-41.

40. Skowron, G., et al., *Alternating and intermittent regimens of zidovudine and dideoxycytidine in patients with AIDS or AIDS-related complex.* Ann Intern Med, 1993. **118**(5): p. 321-30.
41. Kuritzkes, D.R., et al., *Lamivudine in combination with zidovudine, stavudine, or didanosine in patients with HIV-1 infection. A randomized, double-blind, placebo-controlled trial. National Institute of Allergy and Infectious Disease AIDS Clinical Trials Group Protocol 306 Investigators.* Aids, 1999. **13**(6): p. 685-94.
42. Cameron, D.W., et al., *Ritonavir and saquinavir combination therapy for the treatment of HIV infection.* Aids, 1999. **13**(2): p. 213-24.
43. Montaner, J.S., et al., *A randomized, double-blind trial comparing combinations of nevirapine, didanosine, and zidovudine for HIV-infected patients: the INCAS Trial. Italy, The Netherlands, Canada and Australia Study.* Jama, 1998. **279**(12): p. 930-7.
44. Michaels, S.H., R. Clark, and P. Kissinger, *Declining morbidity and mortality among patients with advanced human immunodeficiency virus infection.* N Engl J Med, 1998. **339**(6): p. 405-6.
45. Polis, M.A., et al., *Correlation between reduction in plasma HIV-1 RNA concentration 1 week after start of antiretroviral treatment and longer-term efficacy.* Lancet, 2001. **358**(9295): p. 1760-5.
46. Wong, J.K. and S.A. Yukl, *Tissue reservoirs of HIV.* Curr Opin HIV AIDS, 2016. **11**(4): p. 362-70.
47. Chun, T.W., et al., *In vivo fate of HIV-1-infected T cells: quantitative analysis of the transition to stable latency.* Nat Med, 1995. **1**(12): p. 1284-90.
48. Hamlyn, E., et al., *Plasma HIV viral rebound following protocol-indicated cessation of ART commenced in primary and chronic HIV infection.* PLoS One, 2012. **7**(8): p. e43754.
49. Saksena, N.K., et al., *HIV reservoirs in vivo and new strategies for possible eradication of HIV from the reservoir sites.* HIV AIDS (Auckl), 2010. **2**: p. 103-22.
50. Chomont, N., et al., *HIV reservoir size and persistence are driven by T cell survival and homeostatic proliferation.* Nat Med, 2009. **15**(8): p. 893-900.
51. Chun, T.W., et al., *HIV-infected individuals receiving effective antiviral therapy for extended periods of time continually replenish their viral reservoir.* J Clin Invest, 2005. **115**(11): p. 3250-5.
52. Fletcher, C.V., et al., *Persistent HIV-1 replication is associated with lower antiretroviral drug concentrations in lymphatic tissues.* Proc Natl Acad Sci U S A, 2014. **111**(6): p. 2307-12.
53. Siliciano, J.D., et al., *Long-term follow-up studies confirm the stability of the latent reservoir for HIV-1 in resting CD4+ T cells.* Nat Med, 2003. **9**(6): p. 727-8.
54. Cavert, W., et al., *Kinetics of response in lymphoid tissues to antiretroviral therapy of HIV-1 infection.* Science, 1997. **276**(5314): p. 960-4.
55. Lafeuillade, A., et al., *Human immunodeficiency virus type 1 kinetics in lymph nodes compared with plasma.* J Infect Dis, 1996. **174**(2): p. 404-7.
56. Gunthard, H.F., et al., *Residual human immunodeficiency virus (HIV) Type 1 RNA and DNA in lymph nodes and HIV RNA in genital secretions and in cerebrospinal fluid after suppression of viremia for 2 years.* J Infect Dis, 2001. **183**(9): p. 1318-27.
57. Horiike, M., et al., *Lymph nodes harbor viral reservoirs that cause rebound of plasma viremia in SIV-infected macaques upon cessation of combined antiretroviral therapy.* Virology, 2012. **423**(2): p. 107-18.
58. Kline, C., et al., *Persistence of viral reservoirs in multiple tissues after antiretroviral therapy suppression in a macaque RT-SHIV model.* PLoS One, 2013. **8**(12): p. e84275.

59. North, T.W., et al., *Viral sanctuaries during highly active antiretroviral therapy in a nonhuman primate model for AIDS.* J Virol, 2010. **84**(6): p. 2913-22.
60. Cerf-Bensussan, N. and D. Guy-Grand, *Intestinal intraepithelial lymphocytes.* Gastroenterol Clin North Am, 1991. **20**(3): p. 549-76.
61. Mowat, A.M. and J.L. Viney, *The anatomical basis of intestinal immunity.* Immunol Rev, 1997. **156**: p. 145-66.
62. Lapenta, C., et al., *Human intestinal lamina propria lymphocytes are naturally permissive to HIV-1 infection.* Eur J Immunol, 1999. **29**(4): p. 1202-8.
63. Poles, M.A., et al., *A preponderance of CCR5(+) CXCR4(+) mononuclear cells enhances gastrointestinal mucosal susceptibility to human immunodeficiency virus type 1 infection.* J Virol, 2001. **75**(18): p. 8390-9.
64. Anton, P.A., et al., *Enhanced levels of functional HIV-1 co-receptors on human mucosal T cells demonstrated using intestinal biopsy tissue.* Aids, 2000. **14**(12): p. 1761-5.
65. Poles, M.A., et al., *Lack of decay of HIV-1 in gut-associated lymphoid tissue reservoirs in maximally suppressed individuals.* J Acquir Immune Defic Syndr, 2006. **43**(1): p. 65-8.
66. Chun, T.W., et al., *Persistence of HIV in gut-associated lymphoid tissue despite long-term antiretroviral therapy.* J Infect Dis, 2008. **197**(5): p. 714-20.
67. Yukl, S.A., et al., *Differences in HIV burden and immune activation within the gut of HIV-positive patients receiving suppressive antiretroviral therapy.* J Infect Dis, 2010. **202**(10): p. 1553-61.
68. Murray, P.J. and T.A. Wynn, *Protective and pathogenic functions of macrophage subsets.* Nat Rev Immunol, 2011. **11**(11): p. 723-37.
69. Igarashi, T., et al., *Macrophage are the principal reservoir and sustain high virus loads in rhesus macaques after the depletion of CD4+ T cells by a highly pathogenic simian immunodeficiency virus/HIV type 1 chimera (SHIV): Implications for HIV-1 infections of humans.* Proc Natl Acad Sci U S A, 2001. **98**(2): p. 658-63.
70. Ball, J.K., et al., *Genomic variation of human immunodeficiency virus type 1 (HIV-1): molecular analyses of HIV-1 in sequential blood samples and various organs obtained at autopsy.* J Gen Virol, 1994. **75 (Pt 4)**: p. 67-79.
71. van't Wout, A.B., et al., *Analysis of the temporal relationship between human immunodeficiency virus type 1 quasispecies in sequential blood samples and various organs obtained at autopsy.* J Virol, 1998. **72**(1): p. 488-96.
72. Navia, B.A., et al., *The AIDS dementia complex: II. Neuropathology.* Ann Neurol, 1986. **19**(6): p. 525-35.
73. Navia, B.A., B.D. Jordan, and R.W. Price, *The AIDS dementia complex: I. Clinical features.* Ann Neurol, 1986. **19**(6): p. 517-24.
74. Gelman, B.B., et al., *Neurovirological correlation with HIV-associated neurocognitive disorders and encephalitis in a HAART-era cohort.* Journal of acquired immune deficiency syndromes (1999), 2013. **62**(5): p. 487-495.
75. Griffin, W.C., et al., *The severe combined immunodeficient (SCID) mouse model of human immunodeficiency virus encephalitis: deficits in cognitive function.* J Neurovirol, 2004. **10**(2): p. 109-115.
76. Kranick, S.M. and A. Nath, *Neurologic complications of HIV-1 infection and its treatment in the era of antiretroviral therapy.* Continuum (Minneapolis, Minn.), 2012. **18**(6 Infectious Disease): p. 1319-1337.
77. Weed, M.R. and D.J. Steward, *Neuropsychopathology in the SIV/macaque model of AIDS.* Front Biosci, 2005. **10**: p. 710-727.

78. Wilkie, F.L., et al., *Cognitive functioning in younger and older HIV-1-infected adults.* J Acquir Immune Defic Syndr, 2003. **33 Suppl 2**: p. 93-93.
79. Worlein, J.M., et al., *Cognitive and motor deficits associated with HIV-2(287) infection in infant pigtailed macaques: a nonhuman primate model of pediatric neuro-AIDS.* J Neurovirol, 2005. **11**(1): p. 34-45.
80. Butovsky, O., et al., *Activation of microglia by aggregated beta-amyloid or lipopolysaccharide impairs MHC-II expression and renders them cytotoxic whereas IFN-gamma and IL-4 render them protective.* Mol Cell Neurosci, 2005. **29**(3): p. 381-393.
81. Craft, J.M., D.M. Watterson, and L.J. Van Eldik, *Human amyloid beta-induced neuroinflammation is an early event in neurodegeneration.* Glia, 2006. **53**(5): p. 484-490.
82. Ghafouri, M., et al., *HIV-1 associated dementia: symptoms and causes.* Retrovirology, 2006. **3**: p. 28-28.
83. Hirsch, E.C., et al., *The role of glial reaction and inflammation in Parkinson's disease.* Ann N Y Acad Sci, 2003. **991**: p. 214-28.
84. Minghetti, L., *Role of inflammation in neurodegenerative diseases.* Curr Opin Neurol, 2005. **18**(3): p. 315-321.
85. Wu, D.-C., et al., *The inflammatory NADPH oxidase enzyme modulates motor neuron degeneration in amyotrophic lateral sclerosis mice.* Proc Natl Acad Sci U S A, 2006. **103**(32): p. 12132-12137.
86. Zhang, W., et al., *Aggregated alpha-synuclein activates microglia: a process leading to disease progression in Parkinson's disease.* Faseb j, 2005. **19**(6): p. 533-42.
87. Everall, I.P., et al., *Cortical synaptic density is reduced in mild to moderate human immunodeficiency virus neurocognitive disorder. HNRC Group. HIV Neurobehavioral Research Center.* Brain Pathol, 1999. **9**(2): p. 209-217.
88. Masliah, E., et al., *Dendritic injury is a pathological substrate for human immunodeficiency virus-related cognitive disorders. HNRC Group. The HIV Neurobehavioral Research Center.* Ann Neurol, 1997. **42**(6): p. 963-72.
89. McArthur, J.C., et al., *Dementia in AIDS patients: incidence and risk factors. Multicenter AIDS Cohort Study.* Neurology, 1993. **43**(11): p. 2245-2252.
90. Aiamkitsumrit, B., et al., *Bioinformatic analysis of HIV-1 entry and pathogenesis.* Curr HIV Res, 2014. **12**(2): p. 132-61.
91. Klasse, P.J., *The molecular basis of HIV entry.* Cell Microbiol, 2012. **14**(8): p. 1183-92.
92. Williams, D.W., et al., *Mechanisms of HIV entry into the CNS: increased sensitivity of HIV infected CD14+CD16+ monocytes to CCL2 and key roles of CCR2, JAM-A, and ALCAM in diapedesis.* PLoS One, 2013. **8**(7): p. e69270.
93. Toborek, M., et al., *Mechanisms of the blood-brain barrier disruption in HIV-1 infection.* Cell Mol Neurobiol, 2005. **25**(1): p. 181-199.
94. Persidsky, Y. and H.E. Gendelman, *Mononuclear phagocyte immunity and the neuropathogenesis of HIV-1 infection.* J Leukoc Biol, 2003. **74**(5): p. 691-701.
95. Zink, W.E., et al., *The neuropathogenesis of HIV-1 infection.* FEMS Immunol Med Microbiol, 1999. **26**(3-4): p. 233-241.
96. Kanmogne, G.D., P. Grammas, and R.C. Kennedy, *Analysis of human endothelial cells and cortical neurons for susceptibility to HIV-1 infection and co-receptor expression.* J Neurovirol, 2000. **6**(6): p. 519-528.
97. Eugenin, E.A., et al., *HIV-1 tat protein induces a migratory phenotype in human fetal microglia by a CCL2 (MCP-1)-dependent mechanism: possible role in NeuroAIDS.* Glia, 2005. **49**(4): p. 501-510.

98. Kure, K., et al., *Cellular localization of an HIV-1 antigen in subacute AIDS encephalitis using an improved double-labeling immunohistochemical method.* Am J Pathol, 1990. **136**(5): p. 1085-1092.
99. McArthur, J.C., et al., *Human immunodeficiency virus-associated neurocognitive disorders: Mind the gap.* Annals of Neurology, 2010. **67**(6): p. 699-714.
100. Alliot, F., I. Godin, and B. Pessac, *Microglia derive from progenitors, originating from the yolk sac, and which proliferate in the brain.* Brain Res Dev Brain Res, 1999. **117**(2): p. 145-152.
101. Lavi, E., et al., *Chemokine receptors in the human brain and their relationship to HIV infection.* J Neurovirol, 1998. **4**(3): p. 301-11.
102. Miller, F., et al., *Blood-brain barrier and retroviral infections.* Virulence, 2012. **3**(2): p. 222-9.
103. Lipton, S.A., M. Yeh, and E.B. Dreyer, *Update on current models of HIV-related neuronal injury: platelet-activating factor, arachidonic acid and nitric oxide.* Adv Neuroimmunol, 1994. **4**(3): p. 181-188.
104. Tyor, W.R., et al., *Cytokine expression in the brain during the acquired immunodeficiency syndrome.* Ann Neurol, 1992. **31**(4): p. 349-360.
105. Aquaro, S., et al., *Human immunodeficiency virus infection and acquired immunodeficiency syndrome dementia complex: role of cells of monocyte-macrophage lineage.* J Neurovirol, 2005. **11 Suppl 3**: p. 58-66.
106. Nottet, H.S. and H.E. Gendelman, *Unraveling the neuroimmune mechanisms for the HIV-1-associated cognitive/motor complex.* Immunol Today, 1995. **16**(9): p. 441-8.
107. Nottet, H.S., et al., *A regulatory role for astrocytes in HIV-1 encephalitis. An overexpression of eicosanoids, platelet-activating factor, and tumor necrosis factor-alpha by activated HIV-1-infected monocytes is attenuated by primary human astrocytes.* J Immunol, 1995. **154**(7): p. 3567-3581.
108. Peluso, M.J. and S. Spudich, *Treatment of HIV in the CNS: effects of antiretroviral therapy and the promise of non-antiretroviral therapeutics.* Curr HIV/AIDS Rep, 2014. **11**(3): p. 353-62.
109. Persidsky, Y., et al., *Mononuclear phagocytes mediate blood-brain barrier compromise and neuronal injury during HIV-1-associated dementia.* J Leukoc Biol, 2000. **68**(3): p. 413-422.
110. Brabers, N.A.C.H. and H.S.L.M. Nottet, *Role of the pro-inflammatory cytokines TNF-alpha and IL-1beta in HIV-associated dementia.* Eur J Clin Invest, 2006. **36**(7): p. 447-458.
111. Berger, J.R. and M. Avison, *The blood brain barrier in HIV infection.* Front Biosci, 2004. **9**: p. 2680-2685.
112. Andras, I.E., et al., *HIV-1 Tat protein alters tight junction protein expression and distribution in cultured brain endothelial cells.* J Neurosci Res, 2003. **74**(2): p. 255-265.
113. Banks, W.A., V. Akerstrom, and A.J. Kastin, *Adsorptive endocytosis mediates the passage of HIV-1 across the blood-brain barrier: evidence for a post-internalization coreceptor.* J Cell Sci, 1998. **111 (Pt 4)**: p. 533-40.
114. Banks, W.A., et al., *Transport of human immunodeficiency virus type 1 pseudoviruses across the blood-brain barrier: role of envelope proteins and adsorptive endocytosis.* J Virol, 2001. **75**(10): p. 4681-4691.
115. Kanmogne, G.D., C. Primeaux, and P. Grammas, *HIV-1 gp120 proteins alter tight junction protein expression and brain endothelial cell permeability: implications for the pathogenesis of HIV-associated dementia.* J Neuropathol Exp Neurol, 2005. **64**(6): p. 498-505.

116. Kanmogne, G.D., et al., *HIV-1 gp120 compromises blood-brain barrier integrity and enhances monocyte migration across blood-brain barrier: implication for viral neuropathogenesis.* J Cereb Blood Flow Metab, 2007. **27**(1): p. 123-134.
117. Nottet, H.S., et al., *Mechanisms for the transendothelial migration of HIV-1-infected monocytes into brain.* J Immunol, 1996. **156**(3): p. 1284-1295.
118. Wu, D.T., et al., *Mechanisms of leukocyte trafficking into the CNS.* J Neurovirol, 2000. **6 Suppl 1**: p. 82-85.
119. Conant, K., et al., *In vivo and in vitro infection of the astrocyte by HIV-1.* Adv Neuroimmunol, 1994. **4**(3): p. 287-289.
120. Diesing, T.S., et al., *HIV-1-associated dementia: a basic science and clinical perspective.* AIDS Read, 2002. **12**(8): p. 358-368.
121. Lawrence, D.M. and E.O. Major, *HIV-1 and the brain: connections between HIV-1-associated dementia, neuropathology and neuroimmunology.* Microbes Infect, 2002. **4**(3): p. 301-308.
122. Navenot, J.M., et al., *Molecular anatomy of CCR5 engagement by physiologic and viral chemokines and HIV-1 envelope glycoproteins: differences in primary structural requirements for RANTES, MIP-1 alpha, and vMIP-II Binding.* J Mol Biol, 2001. **313**(5): p. 1181-1193.
123. McManus, C.M., et al., *Chemokine and chemokine-receptor expression in human glial elements: induction by the HIV protein, Tat, and chemokine autoregulation.* Am J Pathol, 2000. **156**(4): p. 1441-53.
124. Kutsch, O., et al., *Induction of the chemokines interleukin-8 and IP-10 by human immunodeficiency virus type 1 tat in astrocytes.* J Virol, 2000. **74**(19): p. 9214-9221.
125. Schmidtmayerova, H., et al., *Human immunodeficiency virus type 1 infection alters chemokine beta peptide expression in human monocytes: implications for recruitment of leukocytes into brain and lymph nodes.* Proc Natl Acad Sci U S A, 1996. **93**(2): p. 700-704.
126. Herbein, G. and A. Varin, *The macrophage in HIV-1 infection: from activation to deactivation?* Retrovirology, 2010. **7**: p. 33.
127. Koppensteiner, H., R. Brack-Werner, and M. Schindler, *Macrophages and their relevance in Human Immunodeficiency Virus Type I infection.* Retrovirology, 2012. **9**: p. 82.
128. Burdo, T.H., A. Lackner, and K.C. Williams, *Monocyte/macrophages and their role in HIV neuropathogenesis.* Immunological reviews, 2013. **254**(1): p. 102-113.
129. Eugenin, E.A. and J.W. Berman, *Gap junctions mediate human immunodeficiency virus-bystander killing in astrocytes.* J Neurosci, 2007. **27**(47): p. 12844-50.
130. Maslin, C.L.V., et al., *Transendothelial migration of monocytes: the underlying molecular mechanisms and consequences of HIV-1 infection.* Curr HIV Res, 2005. **3**(4): p. 303-317.
131. Gonzalez, E., et al., *HIV-1 infection and AIDS dementia are influenced by a mutant MCP-1 allele linked to increased monocyte infiltration of tissues and MCP-1 levels.* Proc Natl Acad Sci U S A, 2002. **99**(21): p. 13795-13800.
132. Conant, K., et al., *Induction of monocyte chemoattractant protein-1 in HIV-1 Tat-stimulated astrocytes and elevation in AIDS dementia.* Proc Natl Acad Sci U S A, 1998. **95**(6): p. 3117-3121.
133. Kelder, W., et al., *Beta-chemokines MCP-1 and RANTES are selectively increased in cerebrospinal fluid of patients with human immunodeficiency virus-associated dementia.* Ann Neurol, 1998. **44**(5): p. 831-835.
134. Churchill, M.J., et al., *Extensive astrocyte infection is prominent in human immunodeficiency virus-associated dementia.* Ann Neurol, 2009. **66**(2): p. 253-8.

135. Strelow, L.I., D. Janigro, and J.A. Nelson, *The blood-brain barrier and AIDS.* Adv Virus Res, 2001. **56**: p. 355-88.
136. Buttner, A., P. Mehraein, and S. Weis, *Vascular changes in the cerebral cortex in HIV-1 infection. II. An immunohistochemical and lectinhistochemical investigation.* Acta Neuropathol, 1996. **92**(1): p. 35-41.
137. Shi, B., et al., *Apoptosis induced by HIV-1 infection of the central nervous system.* J Clin Invest, 1996. **98**(9): p. 1979-90.
138. Marechal, V., et al., *Cytosolic Gag p24 as an index of productive entry of human immunodeficiency virus type 1.* J Virol, 1998. **72**(3): p. 2208-12.
139. Marechal, V., et al., *Human immunodeficiency virus type 1 entry into macrophages mediated by macropinocytosis.* J Virol, 2001. **75**(22): p. 11166-77.
140. McClure, M.O., M. Marsh, and R.A. Weiss, *Human immunodeficiency virus infection of CD4-bearing cells occurs by a pH-independent mechanism.* Embo j, 1988. **7**(2): p. 513-8.
141. Liu, B. and J.-S. Hong, *Role of microglia in inflammation-mediated neurodegenerative diseases: mechanisms and strategies for therapeutic intervention.* J Pharmacol Exp Ther, 2003. **304**(1): p. 1-7.
142. Gartner, S. and Y. Liu, *Insights into the role of immune activation in HIV neuropathogenesis.* J Neurovirol, 2002. **8**(2): p. 69-75.
143. Yu, H.J., M.A. Reuter, and D. McDonald, *HIV Traffics through a Specialized, Surface-Accessible Intracellular Compartment during trans-Infection of T Cells by Mature Dendritic Cells.* PLoS Pathog, 2008. **4**(8).
144. Joseph, S.B., et al., *HIV-1 target cells in the CNS.* J Neurovirol, 2014.
145. Gonzalez-Scarano, F. and J. Martin-Garcia, *The neuropathogenesis of AIDS.* Nat Rev Immunol, 2005. **5**(1): p. 69-81.
146. Kettenmann, H., et al., *Physiology of microglia.* Physiological Reviews, 2011. **91**(2): p. 461-553.
147. Ling, E.A., *Influence of cortisone on amoeboid microglia and microglial cells in the corpus callosum in postnatal rats.* J Anat, 1982. **134**(Pt 4): p. 705-17.
148. Pontow, S.E., et al., *Actin cytoskeletal reorganizations and coreceptor-mediated activation of rac during human immunodeficiency virus-induced cell fusion.* J Virol, 2004. **78**(13): p. 7138-7147.
149. Lifson, J., et al., *Role of envelope glycoprotein carbohydrate in human immunodeficiency virus (HIV) infectivity and virus-induced cell fusion.* J Exp Med, 1986. **164**(6): p. 2101-6.
150. Lifson, J.D., et al., *Induction of CD4-dependent cell fusion by the HTLV-III/LAV envelope glycoprotein.* Nature, 1986. **323**(6090): p. 725-8.
151. Matthews, T.J., et al., *Interaction between the human T-cell lymphotropic virus type IIIB envelope glycoprotein gp120 and the surface antigen CD4: role of carbohydrate in binding and cell fusion.* Proc Natl Acad Sci U S A, 1987. **84**(15): p. 5424-5428.
152. Sharer, L.R., et al., *Comparison of simian immunodeficiency virus and human immunodeficiency virus encephalitides in the immature host.* Ann Neurol, 1988. **23 Suppl**: p. 108-112.
153. Deshpande, M., et al., *Role of activated astrocytes in neuronal damage: potential links to HIV-1-associated dementia.* Neurotox Res, 2005. **7**(3): p. 183-192.
154. Wesselingh, S.L. and K.A. Thompson, *Immunopathogenesis of HIV-associated dementia.* Curr Opin Neurol, 2001. **14**(3): p. 375-379.
155. Mehla, R., et al., *Programming of neurotoxic cofactor CXCL-10 in HIV-1-associated dementia: abrogation of CXCL-10-induced neuro-glial toxicity in vitro by PKC activator.* J Neuroinflammation, 2012. **9**: p. 239.

156. Woods, S.P., et al., *HIV-associated Deficits in Action (Verb) Generation May Reflect Astrocytosis.* J Clin Exp Neuropsychol, 2010. **32**(5): p. 522-7.
157. Bezzi, P., et al., *CXCR4-activated astrocyte glutamate release via TNFalpha: amplification by microglia triggers neurotoxicity.* Nat Neurosci, 2001. **4**(7): p. 702-710.
158. Chauhan, A., et al., *HIV-1 endocytosis in astrocytes: A kiss of death or survival of the fittest?* Neurosci Res, 2014. **88c**: p. 16-22.
159. Churchill, M. and A. Nath, *Where does HIV hide? A focus on the central nervous system.* Current opinion in HIV and AIDS, 2013. **8**(3): p. 165-169.
160. Budka, H., *East-West Danube symposium on human and zoonotic spongiform encephalopathies, in Bratislava, Czechoslovakia, May 22-23, 1991.* Brain Pathol, 1991. **1**(4): p. 325-326.
161. Lima, R.G., et al., *The replication of human immunodeficiency virus type 1 in macrophages is enhanced after phagocytosis of apoptotic cells.* J Infect Dis, 2002. **185**(11): p. 1561-1566.
162. Petito, C.K., et al., *Neuropathology of acquired immunodeficiency syndrome (AIDS): an autopsy review.* J Neuropathol Exp Neurol, 1986. **45**(6): p. 635-646.
163. Canque, B., et al., *Macrophage inflammatory protein-1alpha is induced by human immunodeficiency virus infection of monocyte-derived macrophages.* Blood, 1996. **87**(5): p. 2011-2019.
164. Farzan, M., et al., *HIV-1 entry and macrophage inflammatory protein-1beta-mediated signaling are independent functions of the chemokine receptor CCR5.* J Biol Chem, 1997. **272**(11): p. 6854-6857.
165. Jennes, W., et al., *Disturbed secretory capacity for macrophage inflammatory protein (MIP)-1 alpha and MIP-1 beta in progressive HIV infection.* AIDS Res Hum Retroviruses, 2004. **20**(10): p. 1087-1091.
166. Miyakawa, T., et al., *Identification of amino acid residues critical for LD78beta, a variant of human macrophage inflammatory protein-1alpha, binding to CCR5 and inhibition of R5 human immunodeficiency virus type 1 replication.* J Biol Chem, 2002. **277**(7): p. 4649-4655.
167. Chen, K., et al., *CD40/CD40L dyad in the inflammatory and immune responses in the central nervous system.* Cell Mol Immunol, 2006. **3**(3): p. 163-169.
168. Holm, G.H. and D. Gabuzda, *Distinct mechanisms of CD4+ and CD8+ T-cell activation and bystander apoptosis induced by human immunodeficiency virus type 1 virions.* J Virol, 2005. **79**(10): p. 6299-311.
169. Marcondes, M.C., et al., *Highly activated CD8(+) T cells in the brain correlate with early central nervous system dysfunction in simian immunodeficiency virus infection.* J Immunol, 2001. **167**(9): p. 5429-5438.
170. Weidenheim, K.M., I. Epshteyn, and W.D. Lyman, *Immunocytochemical identification of T-cells in HIV-1 encephalitis: implications for pathogenesis of CNS disease.* Mod Pathol, 1993. **6**(2): p. 167-174.
171. Kornbluth, R.S., K. Kee, and D.D. Richman, *CD40 ligand (CD154) stimulation of macrophages to produce HIV-1-suppressive beta-chemokines.* Proc Natl Acad Sci U S A, 1998. **95**(9): p. 5205-10.
172. Zhang, R., et al., *CD40 ligand dysregulation in HIV infection: HIV glycoprotein 120 inhibits signaling cascades upstream of CD40 ligand transcription.* J Immunol, 2004. **172**(4): p. 2678-2686.
173. Zhang, L., et al., *Quantifying residual HIV-1 replication in patients receiving combination antiretroviral therapy.* N Engl J Med, 1999. **340**(21): p. 1605-1613.

174. Heaton, R.K., et al., *HIV-associated neurocognitive disorders persist in the era of potent antiretroviral therapy: CHARTER Study.* Neurology, 2010. **75**(23): p. 2087-96.
175. Saylor, D., et al., *HIV-associated neurocognitive disorder--pathogenesis and prospects for treatment.* Nat Rev Neurol, 2016. **12**(4): p. 234-48.
176. Renju, J., et al., *'Side effects' are 'central effects' that challenge retention in HIV treatment programmes in six sub-Saharan African countries: a multicountry qualitative study.* Sex Transm Infect, 2017. **93**(Suppl 3).
177. Zhang, L., et al., *Side effects, adherence self-efficacy, and adherence to antiretroviral treatment: a mediation analysis in a Chinese sample.* AIDS Care, 2016. **28**(7): p. 919-26.
178. Robertson, K., J. Liner, and R.B. Meeker, *Antiretroviral neurotoxicity.* J Neurovirol, 2012. **18**(5): p. 388-99.
179. Robertson, K.R., et al., *Neurocognitive effects of treatment interruption in stable HIV-positive patients in an observational cohort.* Neurology, 2010. **74**(16): p. 1260-6.
180. Apostolova, N., et al., *Efavirenz and the CNS: what we already know and questions that need to be answered.* J Antimicrob Chemother, 2015. **70**(10): p. 2693-708.
181. Gutierrez, F., et al., *Prediction of neuropsychiatric adverse events associated with long-term efavirenz therapy, using plasma drug level monitoring.* Clin Infect Dis, 2005. **41**(11): p. 1648-53.
182. Blanch, J., et al., *Preliminary data of a prospective study on neuropsychiatric side effects after initiation of efavirenz.* J Acquir Immune Defic Syndr, 2001. **27**(4): p. 336-43.
183. Clifford, D.B., et al., *Impact of efavirenz on neuropsychological performance and symptoms in HIV-infected individuals.* Ann Intern Med, 2005. **143**(10): p. 714-21.
184. van Luin, M., et al., *Absence of a relation between efavirenz plasma concentrations and toxicity-driven efavirenz discontinuations in the EuroSIDA study.* Antivir Ther, 2009. **14**(1): p. 75-83.
185. *Statement on potential safety signal in infants born to women taking dolutegravir from the HHS antiretroviral guideline panels* 2018.
186. Kevadiya, B.D., et al., *Neurotheranostics as personalized medicines.* Adv Drug Deliv Rev, 2018.
187. Lammers, T., et al., *Theranostic nanomedicine.* Acc Chem Res, 2011. **44**(10): p. 1029-38.
188. Kevadiya, B.D., et al., *Multimodal Theranostic Nanoformulations Permit Magnetic Resonance Bioimaging of Antiretroviral Drug Particle Tissue-Cell Biodistribution.* Theranostics, 2018. **8**(1): p. 256-276.
189. Scatliff, J.H. and P.J. Morris, *From Roentgen to magnetic resonance imaging: the history of medical imaging.* N C Med J, 2014. **75**(2): p. 111-3.
190. Pierre, V.C., M.J. Allen, and P. Caravan, *Contrast agents for MRI: 30+ years and where are we going?* J Biol Inorg Chem, 2014. **19**(2): p. 127-31.
191. Xiao, Y.D., et al., *MRI contrast agents: Classification and application (Review).* Int J Mol Med, 2016. **38**(5): p. 1319-1326.
192. Neuwelt, A., et al., *Iron-based superparamagnetic nanoparticle contrast agents for MRI of infection and inflammation.* AJR Am J Roentgenol, 2015. **204**(3): p. W302-13.
193. Schneider, A.F.L. and C.P.R. Hackenberger, *Fluorescent labelling in living cells.* Curr Opin Biotechnol, 2017. **48**: p. 61-68.
194. Liu, G., *Advances in the theoretical understanding of photon upconversion in rare-earth activated nanophosphors.* Chem Soc Rev, 2015. **44**(6): p. 1635-52.
195. Edagwa, B., et al., *Long-acting slow effective release antiretroviral therapy.* Expert Opinion on Drug Delivery, 2017: p. 1-11.

196. Singh, D., et al., *Development and characterization of a long-acting nanoformulated abacavir prodrug.* Nanomedicine (Lond), 2016. **11**(15): p. 1913-27.
197. Andrews, C.D. and W. Heneine, *Cabotegravir long-acting for HIV-1 prevention.* Curr Opin HIV AIDS, 2015. **10**(4): p. 258-63.
198. Araínga, M., et al., *A mature macrophage is a principal HIV-1 cellular reservoir in humanized mice after treatment with long acting antiretroviral therapy.* Retrovirology, 2017. **14**(1): p. 17.
199. Landovitz, R.J., R. Kofron, and M. McCauley, *The promise and pitfalls of long-acting injectable agents for HIV prevention.* Curr Opin HIV AIDS, 2016. **11**(1): p. 122-8.
200. Margolis, D.A., et al., *Cabotegravir plus rilpivirine, once a day, after induction with cabotegravir plus nucleoside reverse transcriptase inhibitors in antiretroviral-naive adults with HIV-1 infection (LATTE): a randomised, phase 2b, dose-ranging trial.* Lancet Infect Dis, 2015. **15**(10): p. 1145-1155.
201. Spreen, W.R., D.A. Margolis, and J.C. Pottage, *Long-acting injectable antiretrovirals for HIV treatment and prevention.* Curr Opin HIV AIDS, 2013. **8**.
202. Gnanadhas, D.P., et al., *Autophagy facilitates macrophage depots of sustained-release nanoformulated antiretroviral drugs.* J Clin Invest, 2017. **127**(3): p. 857-873.
203. Ma, L., et al., *Efficient Targeting of Adipose Tissue Macrophages in Obesity with Polysaccharide Nanocarriers.* ACS Nano, 2016. **10**(7): p. 6952-62.
204. Martin, P., et al., *Augmented Inhibition of CYP3A4 in Human Primary Hepatocytes by Ritonavir Solid Drug Nanoparticles.* Mol Pharm, 2015. **12**(10): p. 3556-68.
205. Miller, M.A., et al., *Radiation therapy primes tumors for nanotherapeutic delivery via macrophage-mediated vascular bursts.* Sci Transl Med, 2017. **9**(392).
206. Puligujja, P., et al., *Pharmacodynamics of long-acting folic acid-receptor targeted ritonavir-boosted atazanavir nanoformulations.* Biomaterials, 2015. **41**: p. 141-150.
207. Weissleder, R., M. Nahrendorf, and M.J. Pittet, *Imaging macrophages with nanoparticles.* Nat Mater, 2014. **13**(2): p. 125-138.
208. Chen, W., et al., *Long-Acting Release Formulation of Exendin-4 Based on Biomimetic Mineralization for Type 2 Diabetes Therapy.* ACS Nano, 2017. **11**(5): p. 5062-5069.
209. Chou, S.F., D. Carson, and K.A. Woodrow, *Current strategies for sustaining drug release from electrospun nanofibers.* J Control Release, 2015. **220**(Pt B): p. 584-91.
210. Radzio, J., et al., *The long-acting integrase inhibitor GSK744 protects macaques from repeated intravaginal SHIV challenge.* Sci Transl Med, 2015. **7**(270): p. 270ra5.
211. Schneider, E.L., et al., *Subcutaneously Administered Self-Cleaving Hydrogel-Octreotide Conjugates Provide Very Long-Acting Octreotide.* Bioconjug Chem, 2016. **27**(7): p. 1638-44.
212. Tibbitt, M.W., J.E. Dahlman, and R. Langer, *Emerging Frontiers in Drug Delivery.* J Am Chem Soc, 2016. **138**(3): p. 704-17.
213. Mandal, B., et al., *Development and in vitro evaluation of core–shell type lipid–polymer hybrid nanoparticles for the delivery of erlotinib in non-small cell lung cancer.* European Journal of Pharmaceutical Sciences, 2016. **81**: p. 162-171.
214. Krishnamurthy, S., et al., *Lipid-coated polymeric nanoparticles for cancer drug delivery.* Biomaterials Science, 2015. **3**(7): p. 923-936.
215. Krais, A., et al., *Targeted uptake of folic acid-functionalized iron oxide nanoparticles by ovarian cancer cells in the presence but not in the absence of serum.* Nanomedicine, 2014. **10**(7): p. 1421-31.

216. Low, P.S., W.A. Henne, and D.D. Doorneweerd, *Discovery and development of folic-acid-based receptor targeting for imaging and therapy of cancer and inflammatory diseases.* Acc Chem Res, 2008. **41**(1): p. 120-9.
217. Paulos, C.M., et al., *Folate receptor-mediated targeting of therapeutic and imaging agents to activated macrophages in rheumatoid arthritis.* Adv Drug Deliv Rev, 2004. **56**(8): p. 1205-17.
218. Rollett, A., et al., *Folic acid-functionalized human serum albumin nanocapsules for targeted drug delivery to chronically activated macrophages.* Int J Pharm, 2012. **427**(2): p. 460-6.
219. Thomas, T.P., et al., *Folate-targeted nanoparticles show efficacy in the treatment of inflammatory arthritis.* Arthritis Rheum, 2011. **63**(9): p. 2671-80.
220. Zhao, X., H. Li, and R.J. Lee, *Targeted drug delivery via folate receptors.* Expert Opin Drug Deliv, 2008. **5**(3): p. 309-19.
221. Patel, N.R., et al., *Design, Synthesis, and Characterization of Folate-Targeted Platinum-Loaded Theranostic Nanoemulsions for Therapy and Imaging of Ovarian Cancer.* Mol Pharm, 2016. **13**(6): p. 1996-2009.
222. Zhang, Z. and J. Yao, *Preparation of Irinotecan-Loaded Folate-Targeted Liposome for Tumor Targeting Delivery and Its Antitumor Activity.* AAPS PharmSciTech, 2012. **13**(3): p. 802-810.
223. Kevadiya, B.D., et al., *Development of europium doped core-shell silica cobalt ferrite functionalized nanoparticles for magnetic resonance imaging.* Acta Biomaterialia, 2017. **49**: p. 507-520.
224. Sengupta, S., et al., *Temporal targeting of tumour cells and neovasculature with a nanoscale delivery system.* Nature, 2005. **436**(7050): p. 568-572.
225. Kevadiya, B.D., G.V. Joshi, and H.C. Bajaj, *Layered bionanocomposites as carrier for procainamide.* Int J Pharm, 2010. **388**(1-2): p. 280-6.
226. Kevadiya, B.D., et al., *Evaluation of clay/poly (L-lactide) microcomposites as anticancer drug, 6-mercaptopurine reservoir through in vitro cytotoxicity, oxidative stress markers and in vivo pharmacokinetics.* Colloids Surf B Biointerfaces, 2013. **112**: p. 400-7.
227. Gendelman, H.E., et al., *Efficient isolation and propagation of human immunodeficiency virus on recombinant colony-stimulating factor 1-treated monocytes.* J Exp Med, 1988. **167**(4): p. 1428-41.
228. MacParland, S.A., et al., *Phenotype Determines Nanoparticle Uptake by Human Macrophages from Liver and Blood.* ACS Nano, 2017. **11**(3): p. 2428-2443.
229. Guo, D., et al., *Creation of a Long-Acting Nanoformulated 2',3'-Dideoxy-3'-Thiacytidine.* Journal of Acquired Immune Deficiency Syndromes (1999), 2017. **74**(3): p. e75-e83.
230. Kalter, D.C., H.E. Gendelman, and M.S. Meltzer, *Inhibition of human immunodeficiency virus infection in monocytes by monoclonal antibodies against leukocyte adhesion molecules.* Immunol Lett, 1991. **30**(2): p. 219-27.
231. Nadeem, M., et al., *Magnetic Properties of Polyvinyl Alcohol and Doxorubicine Loaded Iron Oxide Nanoparticles for Anticancer Drug Delivery Applications.* PLOS ONE, 2016. **11**(6): p. e0158084.
232. Nyaku, A.N., S.G. Kelly, and B.O. Taiwo, *Long-Acting Antiretrovirals: Where Are We now?* Curr HIV/AIDS Rep, 2017. **14**(2): p. 63-71.
233. Rusconi, S., S. Marcotullio, and A. Cingolani, *Long-acting agents for HIV infection: biological aspects, role in treatment and prevention, and patient's perspective.* New Microbiol, 2017. **40**(2).

234. Kirtane, A.R., R. Langer, and G. Traverso, *Past, Present, and Future Drug Delivery Systems for Antiretrovirals.* J Pharm Sci, 2016. **105**(12): p. 3471-3482.
235. Ma, A., et al., *Improving adherence and clinical outcomes through an HIV pharmacist's interventions.* AIDS Care, 2010. **22**(10): p. 1189-94.
236. Koppensteiner, H., R. Brack-Werner, and M. Schindler, *Macrophages and their relevance in Human Immunodeficiency Virus Type I infection.* Retrovirology, 2012. **9**: p. 82-82.
237. Williams, D.W., et al., *Monocytes mediate HIV neuropathogenesis: mechanisms that contribute to HIV associated neurocognitive disorders.* Curr HIV Res, 2014. **12**(2): p. 85-96.
238. Bastin, G. and S.P. Heximer, *Rab family proteins regulate the endosomal trafficking and function of RGS4.* J Biol Chem, 2013. **288**.
239. Caillet, M., et al., *Rab7A is required for efficient production of infectious HIV-1.* PLoS Pathog, 2011. **7**.
240. Bain, A.D., C. Kumar Anand, and Z. Nie, *Exact solution of the CPMG pulse sequence with phase variation down the echo train: application to R(2) measurements.* J Magn Reson, 2011. **209**(2): p. 183-94.
241. Malinouski, M., et al., *Genome-wide RNAi ionomics screen reveals new genes and regulation of human trace element metabolism.* Nat Commun, 2014. **5**: p. 3301.
242. Amiri, S. and H. Shokrollahi, *Magnetic and structural properties of RE doped Co-ferrite (REåNd, Eu, and Gd) nano-particles synthesized by co-precipitation.* Journal of Magnetism and Magnetic Materials, 2013. **345**: p. 18-23.
243. Huang, H.-C., et al., *Formulation of novel lipid-coated magnetic nanoparticles as the probe for in vivo imaging.* Journal of Biomedical Science, 2009. **16**(1): p. 86.
244. Garapaty, A. and J.A. Champion, *Tunable particles alter macrophage uptake based on combinatorial effects of physical properties.* Bioengineering & Translational Medicine, 2017. **2**(1): p. 92-101.
245. Paul, D., et al., *Phagocytosis Dynamics Depends on Target Shape.* Biophysical Journal, 2013. **105**(5): p. 1143-1150.
246. Toy, R., et al., *Shaping cancer nanomedicine: The effect of particle shape on the in vivo journey of nanoparticles.* Nanomedicine (London, England), 2014. **9**(1): p. 121-134.
247. Puligujja, P., et al., *Macrophage folate receptor-targeted antiretroviral therapy facilitates drug entry, retention, antiretroviral activities and biodistribution for reduction of human immunodeficiency virus infections.* Nanomedicine, 2013. **9**.
248. Lameijer, M.A., et al., *Monocytes and macrophages as nanomedicinal targets for improved diagnosis and treatment of disease.* Expert Rev Mol Diagn, 2013. **13**(6): p. 567-80.
249. Zanganeh, S., et al., *Iron oxide nanoparticles inhibit tumour growth by inducing pro-inflammatory macrophage polarization in tumour tissues.* Nat Nanotechnol, 2016. **11**(11): p. 986-994.
250. Chen, M.F., A.J. Gill, and D.L. Kolson, *Neuropathogenesis of HIV-associated neurocognitive disorders: roles for immune activation, HIV blipping and viral tropism.* Curr Opin HIV AIDS, 2014. **9**(6): p. 559-64.
251. Ho, E.L. and C.M. Marra, *Central nervous system diseases due to opportunistic and coinfections.* Semin Neurol, 2014. **34**(1): p. 61-9.
252. Ipp, H., et al., *Role of inflammation in HIV-1 disease progression and prognosis.* Crit Rev Clin Lab Sci, 2014. **51**(2): p. 98-111.
253. Penafiel, J., et al., *Tolerability of integrase inhibitors in a real-life setting.* J Antimicrob Chemother, 2017.

254. Sanchez, A.B. and M. Kaul, *Neuronal Stress and Injury Caused by HIV-1, cART and Drug Abuse: Converging Contributions to HAND.* Brain Sci, 2017. **7**(3).
255. Tovar-y-Romo, L.B., et al., *Dendritic spine injury induced by the 8-hydroxy metabolite of efavirenz.* J Pharmacol Exp Ther, 2012. **343**(3): p. 696-703.
256. Hoffmann, C., et al., *Higher rates of neuropsychiatric adverse events leading to dolutegravir discontinuation in women and older patients.* HIV Med, 2017. **18**(1): p. 56-63.
257. Sillman, B., et al., *Creation of a long-acting nanoformulated dolutegravir.* Nat Commun, 2018. **9**(1): p. 443.
258. Brenner, B.G. and M.A. Wainberg, *Clinical benefit of dolutegravir in HIV-1 management related to the high genetic barrier to drug resistance.* Virus Res, 2016.
259. Karmon, S.L. and M. Markowitz, *Next-generation integrase inhibitors : where to after raltegravir?* Drugs, 2013. **73**(3): p. 213-28.
260. Katlama, C., et al., *Dolutegravir as monotherapy in HIV-1-infected individuals with suppressed HIV viraemia.* J Antimicrob Chemother, 2016. **71**(9): p. 2646-50.
261. Edagwa, B., et al., *Long-acting slow effective release antiretroviral therapy.* Expert Opin Drug Deliv, 2017. **14**(11): p. 1281-1291.
262. Edagwa, B.J., et al., *Development of HIV reservoir targeted long acting nanoformulated antiretroviral therapies.* Curr Med Chem, 2014. **21**(36): p. 4186-98.
263. Li, T., et al., *Magnetic resonance imaging of folic acid-coated magnetite nanoparticles reflects tissue biodistribution of long-acting antiretroviral therapy.* Int J Nanomedicine, 2015. **10**: p. 3779-90.
264. Puligujja, P., et al., *Pharmacodynamics of folic acid receptor targeted antiretroviral nanotherapy in HIV-1-infected humanized mice.* Antiviral Res, 2015. **120**: p. 85-8.
265. Puligujja, P., et al., *Macrophage folate receptor-targeted antiretroviral therapy facilitates drug entry, retention, antiretroviral activities and biodistribution for reduction of human immunodeficiency virus infections.* Nanomedicine, 2013. **9**(8): p. 1263-73.
266. Zhang, G., et al., *The mixed lineage kinase-3 inhibitor URMC-099 improves therapeutic outcomes for long-acting antiretroviral therapy.* Nanomedicine, 2016. **12**(1): p. 109-22.
267. Cottrell, M.L., T. Hadzic, and A.D. Kashuba, *Clinical pharmacokinetic, pharmacodynamic and drug-interaction profile of the integrase inhibitor dolutegravir.* Clin Pharmacokinet, 2013. **52**(11): p. 981-94.
268. Min, S., et al., *Antiviral activity, safety, and pharmacokinetics/pharmacodynamics of dolutegravir as 10-day monotherapy in HIV-1-infected adults.* Aids, 2011. **25**(14): p. 1737-45.
269. Epstein, A.A., et al., *Combinatorial assessments of brain tissue metabolomics and histopathology in rodent models of human immunodeficiency virus infection.* J Neuroimmune Pharmacol, 2013. **8**(5): p. 1224-38.
270. Ivanisevic, J., et al., *Toward 'omic scale metabolite profiling: a dual separation-mass spectrometry approach for coverage of lipid and central carbon metabolism.* Anal Chem, 2013. **85**(14): p. 6876-84.
271. Tautenhahn, R., et al., *XCMS Online: a web-based platform to process untargeted metabolomic data.* Anal Chem, 2012. **84**(11): p. 5035-9.
272. Rossetti, B., F. Montagnani, and A. De Luca, *Current and emerging two-drug approaches for HIV-1 therapy in ART-naive and ART-experienced, virologically suppressed patients.* Expert Opin Pharmacother, 2018. **19**(7): p. 713-738.

273. Letendre, S.L., et al., *ING116070: a study of the pharmacokinetics and antiviral activity of dolutegravir in cerebrospinal fluid in HIV-1-infected, antiretroviral therapy-naive subjects.* Clin Infect Dis, 2014. **59**(7): p. 1032-7.
274. Al Mamun Bhuyan, A., et al., *Enhanced Eryptosis Following Exposure to Dolutegravir.* Cell Physiol Biochem, 2016. **39**(2): p. 639-50.
275. Eiden, C., et al., *Severe insomnia related to high concentrations of raltegravir.* Aids, 2011. **25**(5): p. 725-7.
276. Harris, M., G. Larsen, and J.S. Montaner, *Exacerbation of depression associated with starting raltegravir: a report of four cases.* Aids, 2008. **22**(14): p. 1890-2.
277. Kheloufi, F., et al., *Psychiatric disorders after starting dolutegravir: report of four cases.* Aids, 2015. **29**(13): p. 1723-5.
278. Kheloufi, F., et al., *Neuropsychiatric events and dolutegravir in HIV patients: a worldwide issue involving a class effect.* Aids, 2017. **31**(12): p. 1775-1777.
279. Menard, A., et al., *Neuropsychiatric adverse effects on dolutegravir: an emerging concern in Europe.* Aids, 2017. **31**(8): p. 1201-1203.
280. Koteff, J., et al., *A phase 1 study to evaluate the effect of dolutegravir on renal function via measurement of iohexol and para-aminohippurate clearance in healthy subjects.* Br J Clin Pharmacol, 2013. **75**(4): p. 990-6.
281. Raffi, F., et al., *Once-daily dolutegravir versus raltegravir in antiretroviral-naive adults with HIV-1 infection: 48 week results from the randomised, double-blind, non-inferiority SPRING-2 study.* Lancet, 2013. **381**(9868): p. 735-43.
282. Reynolds, A., et al., *Oxidative stress and the pathogenesis of neurodegenerative disorders.* Int Rev Neurobiol, 2007. **82**: p. 297-325.
283. Castellino, S., et al., *Metabolism, excretion, and mass balance of the HIV-1 integrase inhibitor dolutegravir in humans.* Antimicrob Agents Chemother, 2013. **57**(8): p. 3536-46.
284. Funes, H.A., et al., *Neuronal bioenergetics and acute mitochondrial dysfunction: a clue to understanding the central nervous system side effects of efavirenz.* J Infect Dis, 2014. **210**(9): p. 1385-95.
285. Funes, H.A., et al., *Efavirenz alters mitochondrial respiratory function in cultured neuron and glial cell lines.* J Antimicrob Chemother, 2015. **70**(8): p. 2249-54.
286. Luo, J., R. Borgens, and R. Shi, *Polyethylene glycol improves function and reduces oxidative stress in synaptosomal preparations following spinal cord injury.* J Neurotrauma, 2004. **21**(8): p. 994-1007.
287. Hannig, J., et al., *Surfactant sealing of membranes permeabilized by ionizing radiation.* Radiat Res, 2000. **154**(2): p. 171-7.
288. Lee, R.C., et al., *Surfactant-induced sealing of electropermeabilized skeletal muscle membranes in vivo.* Proc Natl Acad Sci U S A, 1992. **89**(10): p. 4524-8.
289. Luo, J., R. Borgens, and R. Shi, *Polyethylene glycol immediately repairs neuronal membranes and inhibits free radical production after acute spinal cord injury.* J Neurochem, 2002. **83**(2): p. 471-80.
290. Moloughney, J.G. and N. Weisleder, *Poloxamer 188 (p188) as a membrane resealing reagent in biomedical applications.* Recent Pat Biotechnol, 2012. **6**(3): p. 200-11.
291. Bardia, A., et al., *Efficacy of antioxidant supplementation in reducing primary cancer incidence and mortality: systematic review and meta-analysis.* Mayo Clin Proc, 2008. **83**(1): p. 23-34.
292. Fusco, D., et al., *Effects of antioxidant supplementation on the aging process.* Clin Interv Aging, 2007. **2**(3): p. 377-87.

293. Nitta, H., et al., *Effects of nutritional supplementation with antioxidant vitamins and minerals and fish oil on antioxidant status and psychosocial stress in smokers: an open trial.* Clin Exp Med, 2007. **7**(4): p. 179-83.
294. Wohlfart, S., S. Gelperina, and J. Kreuter, *Transport of drugs across the blood-brain barrier by nanoparticles.* J Control Release, 2012. **161**(2): p. 264-73.
295. Ahmed, A.E., et al., *Fetal origin of adverse pregnancy outcome: the water disinfectant by-product chloroacetonitrile induces oxidative stress and apoptosis in mouse fetal brain.* Brain Res Dev Brain Res, 2005. **159**(1): p. 1-11.
296. Han, Z.J., et al., *Oxidative stress is implicated in arsenic-induced neural tube defects in chick embryos.* Int J Dev Neurosci, 2011. **29**(7): p. 673-80.
297. Kotch, L.E., S.Y. Chen, and K.K. Sulik, *Ethanol-induced teratogenesis: free radical damage as a possible mechanism.* Teratology, 1995. **52**(3): p. 128-36.
298. Tung, E.W. and L.M. Winn, *Valproic acid increases formation of reactive oxygen species and induces apoptosis in postimplantation embryos: a role for oxidative stress in valproic acid-induced neural tube defects.* Mol Pharmacol, 2011. **80**(6): p. 979-87.
299. Zhao, Z. and E.A. Reece, *Nicotine-induced embryonic malformations mediated by apoptosis from increasing intracellular calcium and oxidative stress.* Birth Defects Res B Dev Reprod Toxicol, 2005. **74**(5): p. 383-91.